Radar detection of cosmic-ray and neutrino induced cascades

By

Steven Prohira

Submitted to the Department of Physics and Astronomy and the
Graduate Faculty of the University of Kansas
in partial fulfillment of the requirements for the degree of
Doctor of Philosophy

Committee members

David Besson, Chairperson

KC Kong

John P. Ralston

Alice Bean

Doug McKay

Chris Allen

Date defended: 5 September 2018

The Dissertation Committee for Steven Prohira certifies
that this is the approved version of the following dissertation :

Radar detection of cosmic-ray and neutrino induced cascades

David Besson, Chairperson

Date approved: 28 November 2018

Abstract

An ultra high energy particle, incident upon the earth, will produce a cascade of particles upon interaction. Detection of this cascade holds the key to understanding the properties of the primary-what it was, how much energy it carried, and maybe even where it came from. Of the many strategies developed over the course of the last century to detect such cascades, the radar technique is one of the latest to be explored with interest. For high enough incident energies, the relativistic progression of the cascade through a medium will produce a cloud of ionization that may become dense enough to reflect incident radio-frequency (RF) fields. If so, a broadcasting transmitter and distant receiver could feasibly detect cascades at very long baselines, thereby converting a massive volume of air or ice or sand or salt into a sensitive detector. Such an increase in volume opens up possibility of detecting events which occur on the order of $1 km^{-2} yr^{-1}$ or less. In this dissertation, we present a detailed discussion of the radar detection method, focusing specifically on the detection of ultra high energy cosmic rays in the atmosphere, and ultra high energy neutrinos in dense material, such as ice. We will present the history and experimental efforts to date, and include the latest results from recent models and experiments seeking to address the radar problem. Ultimately, we suggest that the radar method is a promising one for the detection of $>10^{15} eV$ neutrinos which have interacted in a dense medium, such as the Antarctic ice.

For my mother and father.

Acknowledgements

I would firstly like to thank my advisor, Dave Besson, for providing me with innumerable opportunities and being a wonderful mentor and teacher. I hope that this work is the start of a long collaboration, and that I might have the chance to continue to learn from him for years to come.

There are numerous individuals to whom I would like to extend my gratitude:

To KC Kong and JP Ralston for being supportive, insightful, and inspiring inside the classroom and out, and to the rest of my committee for guiding this dissertation. To Gopi Mohlabeng for his friendship and brilliant insights. To my many peers at KU, specifically Sam Kunwar, Jessica Stockham, Mark Stockham, Uzair Latif, Sasha Novikov, Josh Macy, and my graduate student cohort, for making it such a wonderful place to pursue a degree.

To the many colleagues who have most generously given me their time and effort, provided opportunities, lent equipment, guided missions, or offered a place to crash: Krijn de Vries, David Saltzberg, Stephanie Wissel, Amy Connolly, Thomas Meures, Carsten Hast, Peter Gorham, Christian Miki, Cosmin Deaconu, and Linda Cremonesi.

To Rob Young and Ken Ratzlaff, whose expertise in hardware and electronics–not to mention their patient guidance– was a fundamental part of just about every project I worked on at KU.

To the staff, technicians, and scientists at SLAC who provided such excellent beam conditions for T576.

To my parents, David and Jodie, who always put my needs above their own, and to my sister Kellie, and my friends Jeff, Lange, Antonis, and Brian for being supportive, inquisitive, and always up for a chat and some advice during my graduate career.

Most importantly to my wife Erika, for being the only real fundamental constant.

Finally and most generally, I must thank all of those at KU who took a gamble on me. It is left as an exercise for the reader to decide if it was a good idea.

This work was supported in part by a DOE Office of Science Graduate Student Research Award, and a KU Field Station student award. The SCGSR program is administered by the Oak Ridge Institute for Science and Education for the DOE under contract number DE-SC0014664.

Contents

List of Figures

Chapter 1

Introduction

1.1 Overview

Radio Frequency (RF) detection techniques may well be the key to detecting-and therefore understanding-the highest energy particles in the universe. These high energy particles (protons, atomic nuclei, neutrinos), many orders of magnitude more energetic than those that can be produced by any human-made accelerator, arrive at earth from their as-yet-unknown origins[I] and interact with an atom in the atmosphere, land, or sea, causing a cascade of secondary particles. The physics of cascade development is roughly the same for all species of primary particle and all mediums: a primary particle interacts with a constituent atom of the target medium, creating secondary particles which carry a significant fraction of the primary energy. These secondary particles interact with other medium atoms, and/or decay into further secondary particles, which propagate, and so on. Specifics of the primary particle and medium of interaction are important to developing physics models and detector technology, but in general, all cascades develop in this same manner. These cascades are predominantly made up of photons and charged particles, and so in most respects, cosmic-ray and neutrino induced cascade detection is a study of electrodynamics. This is good news for the experimentalist-electrodynamics is well understood. Therefore the only limit to de-

[I] At the time of this writing, IceCube recently announced their first multi-messenger signal [1] to point to a known source, blazar TXS 0506+056, with a 3.5σ significance, suggesting a possible source of extragalactic neutrinos.

veloping robust detection schemes for these cascades-and by extension the primary particles which made them-is the accurate modeling of cascades, and the rich variety of phenomena therein that can be exploited for purposes of detection. This dissertation will focus primarily on one technique: radar-based detection of cosmic-ray and neutrino induced cascades. This introduction will present and classify existing detection techniques, and make the case for radar detection as a useful and unique strategy for cascade detection.

1.2 Cosmic Rays

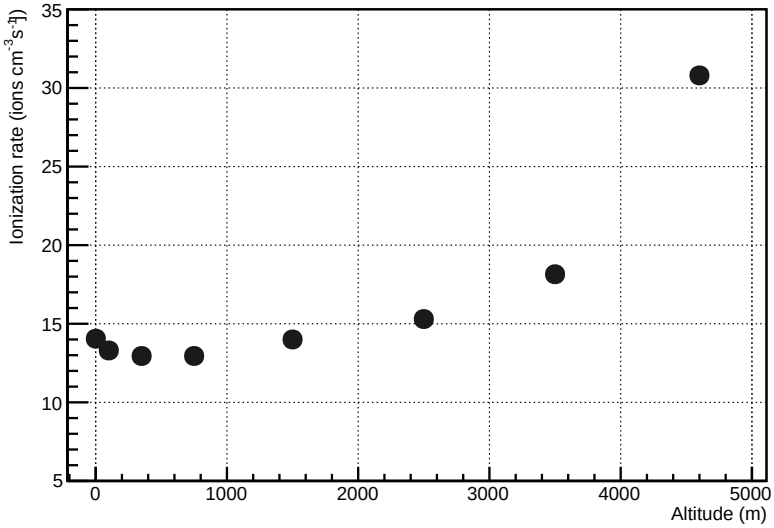

Figure 1.1: The original data from Hess's paper on cosmic rays. These data are the overall averages of measurements from two ionization detectors over several flights made in 1912. Data from [2].

Though observed first nearly 110 years prior by William Morgan [3], x-rays were first named and rigorously explored by Röntgen in 1895 [4]. Röntgen wrote that some invisible ray from an arc discharge in a vacuum tube "is capable of penetrating black cardboard which is quite opaque to ultra-violet light, sunlight, or arc-light" and can expose film or illuminate phosphor screens behind barriers. Upon learning of this, Becquerel studied Röntgen's apparatus and in 1896 made the notable observation that certain materials emit these very same x-rays without any applied power

or excitation from sunlight. Though such phenomena had been observed earlier, Becquerel's were the first deep explorations of radiation. Marie Skłodowska-Curie and later Pierre Curie extended the study to different materials, establishing that radiation came from certain elements. Radiation was then detected just about everywhere, even up in the atmosphere, so experiments were carried out to measure the flux of radiation as a function of height off the ground, to isolate the source. Results were inconclusive until 1912, when Victor Hess made a series of balloon flights up to 5 km with several ionization detectors. The averaged result from several of his flights is shown in Figure 1.1. While initially decreasing as a function of height, Hess's data showed unambiguously that the flux of charged particles increases with height, indicating an extra-terrestrial source of radiation. These particles from above were called cosmic-rays.

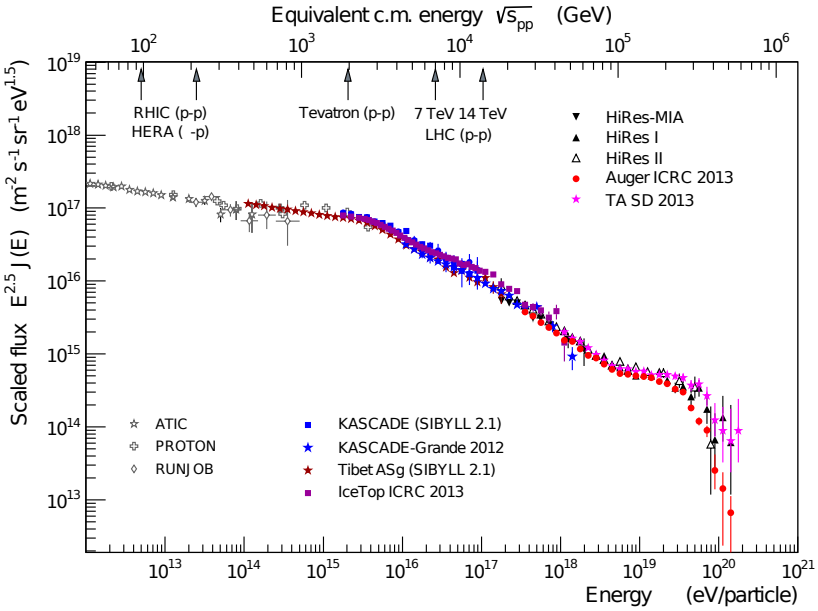

Figure 1.2: The cosmic ray flux as a function of primary particle energy, compiled from various cosmic ray experiments. Taken and adapted from [5].

The cosmic ray flux is shown in Figure 1.2, with contributions provided by many different experiments using many different techniques. The flux of ultra-high energy cosmic rays (UHECR) is extremely low, so the shape of the end of the spectrum (if it is the end of the spectrum) is not well-constrained. The so-called 'ankle' [6] of the spectrum at $\sim 10^{18.5}$ eV has been measured

to high precision by several experiments, but the exact shape of the spectrum above this point is not fully understood. There is a theoretical limit to the energy of an extragalactic proton seen at earth, the so-called Greisen–Zatsepin–Kuz'min (GZK) [7, 8] limit, which is roughly $10^{19.5}$ eV. This limit results from the fact that extremely energetic extragalactic protons above this energy will interact with cosmic microwave background (CMB) photons before arriving at earth, resulting in a suppression of our measured flux. A suppression in the flux of cosmic rays above 10^{19} eV, consistent with the GZK cutoff, was first reported by HiRes [9] and subsequently observed by several experiments, but even the highest statistics measurements [10] have a very limited number of events around the GZK cutoff. This is shown in Figure 1.3. So, higher statistics are needed to sort out exactly what happens at this part of the cosmic ray spectrum. This will be discussed further.

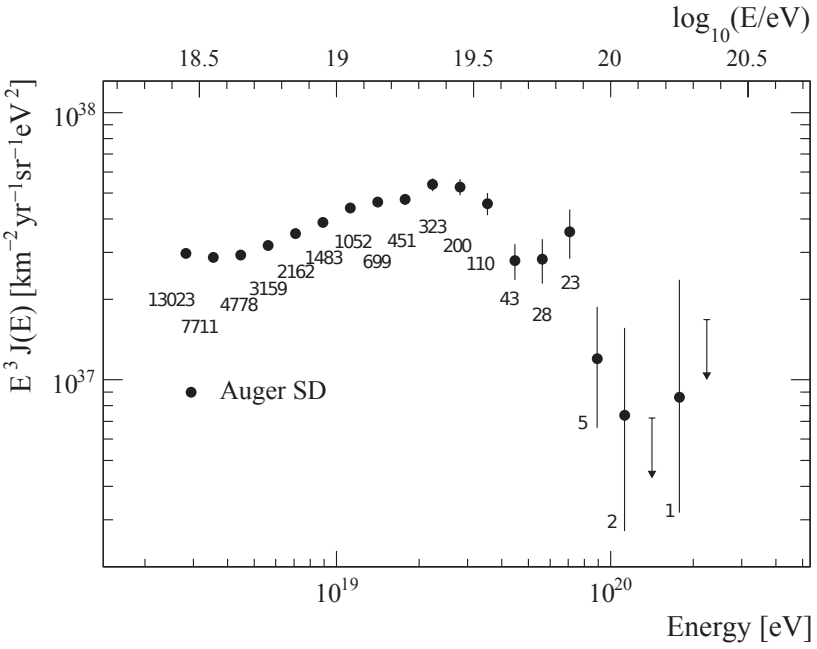

Figure 1.3: The highest-precision measurement to date of the ankle and GZK suppressed region of the cosmic-ray spectrum, from the surface detector of the Auger experiment. Number of events at each energy bin is indicated. Taken from [10].

1.3 Neutrinos

Duchamp once said that "the only works of art America has given are her plumbing and her bridges." To that we might add the discovery of the $\bar{\nu}_e$.

First suggested by Pauli in 1930 to explain the continuous energy spectra of electrons from β decay, neutrinos were elucidated by Fermi in the article *Tentativo di una teoria dei raggi* β[II] in 1933, and experimentally detected by Cowan and Reines [13] in 1956. Neutrinos are weakly interacting particles which were known from the very beginning to have a very small mass. In the language of 1930, β decay was the spontaneous emission of a β particle (now known as either an electron or a positron) from an atomic nucleus. The energy spectrum of the observed β particle varied from its cousins α and γ (α was discovered by Rutherford, γ discovered by Villard, and named in order of the observed depth of penetration through material, from least to most) in that it was continuous, whereas the energy spectra of α and γ particles are strongly peaked. In the case of α decay, a parent nucleus loses an α particle ($2p+2n$, a helium nucleus), with a measured energy equal to the difference $M_{parent} - (M_{child} + M_{\alpha})$. It was thought that β decay was the same basic process, as only one decay product (the β particle) is detected. But instead of obtaining a well defined peak at a certain energy, the spectrum for the outgoing β is observed to be continuous. Bohr suggested, incorrectly, that β decay was evidence of energy conservation violation. Pauli suggested, correctly, that there must be a neutral particle of very small mass which is also produced during the decay, taking some of the energy with it. Fermi dubbed it the neutrino.

The 26-year interval between postulation and discovery of the neutrino is a testament to the challenges of detection. The discovery was made using the process of inverse β decay, building on the suggestion of Pontecorvo [11]. In inverse β decay, a reactor-produced $\bar{\nu}_e$ scatters from a proton in a tank of detector material, producing a positron and a neutron.[III] The positron annihilates with an electron in the material, producing a γ ray burst, which is detected. A second γ ray burst is

[II] Astonishingly, this article was rejected by *Nature* and subsequently did not appear in English at that time [11]. Wilson presented a translation in 1968 [12].

[III] The use of anti-neutrino and flavor notation is anachronistic in this case, as such details had not been yet worked out. But they are used here for those concerned with balancing quantum numbers

produced from capture of the free neutron. Timing and energy measurements of the so-called 'delayed pulse pair' unambiguously demonstrated the neutrino's (more specifically, the electron anti-neutrino's) existence. Of the tens-of-millions-of-trillions of $\bar{\nu}_e$ passing through Cowan and Reines's detector at the Savannah River reactor in 1956, only $\sim$4000 events were detected over the 1371-hour run, implying a very small cross section, which they calculated at $6.3 \times 10^{-44} cm^2$.

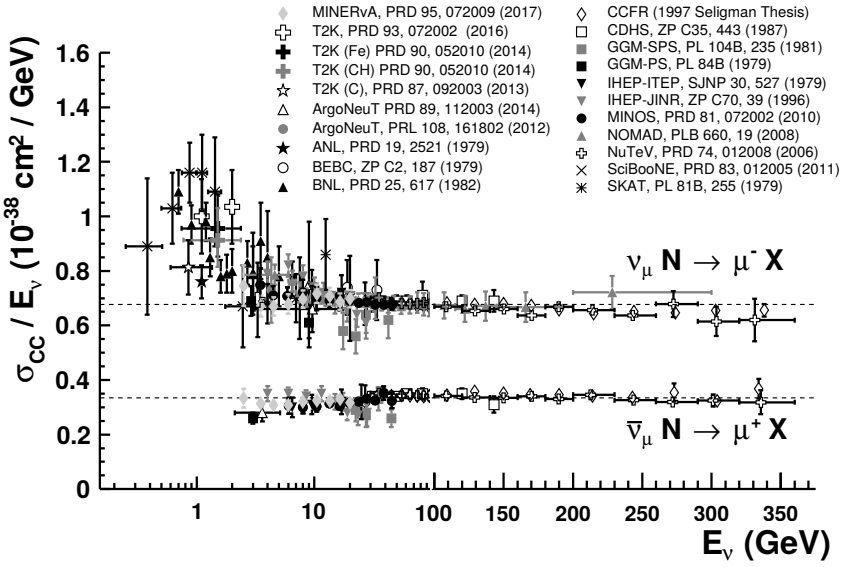

Figure 1.4: A review of the inclusive neutrino-nucleon charged-current (CC) cross sections $\sigma_{\nu N}^{CC}$ from various experiments. The CC cross section is greater than the neutral-current (NC) cross section by a factor of $\sim$3, which is not shown. Taken from [14].

Robust calculations of the neutrino cross section up to ultra-high energies have been made during the intervening years [15], with experimental data available (at the time of this writing) up to $\sim$10 TeV [14, 16, 17]. Figure 1.4 reviews the inclusive CC neutrino-nucleon cross section ($\sigma_{\nu N}^{CC}$) up to 350 GeV, up to which it scales with E_ν.

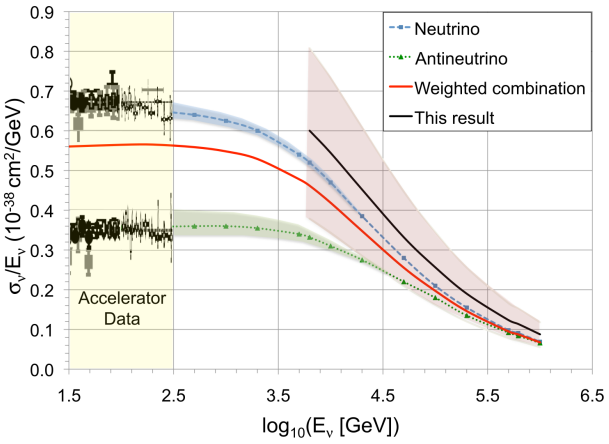

Figure 1.5: $\sigma_{\nu N}^{CC}$ as in Figure 1.4, but with the addition of recent experimental results up to the TeV scale (solid black line, with 1σ error, sys. + stat., shown). Taken from [16].

Above ~350 GeV, $\sigma_{\nu N}^{CC}$ scales as $\sim E_\nu^{0.3}$, being limited by the W and Z boson masses. Current measurements (Figures 1.5, 1.6) show agreement with the most recent cross-section calculations by Connolly et. al. [18]. The data in Figure 1.6 come from the highest-energy publicly available data from the IceCube [19] collaboration.

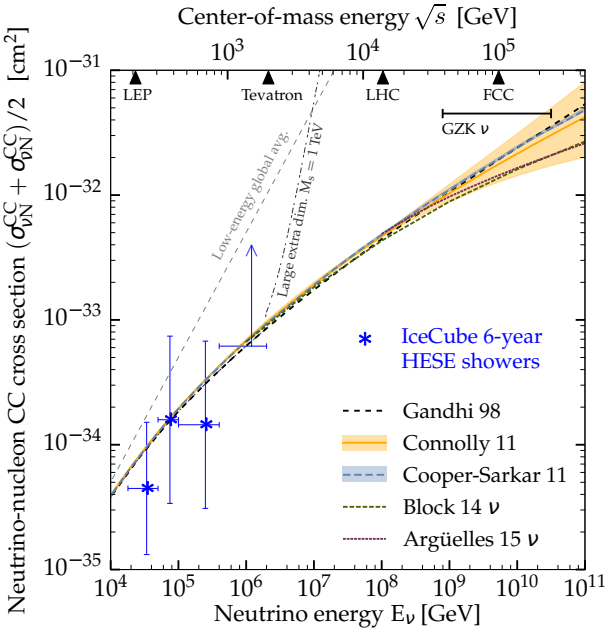

Figure 1.6: Calculated $(\sigma_{\nu N}^{CC} + \sigma_{\bar{\nu}N}^{CC})/2$ at the highest energies, with the latest experimental results overlaid, showing good agreement. Taken from [17].

As can be seen by the low statistics of the data points in Figure 1.6, fluxes at these high energies are exceedingly low, which we will address in later sections when discussing current detection strategies. In short, current detection technologies are limited by the amount of active detector volume comprised by a given experiment. Up above the GeV scale, direct detection of scattering products (e.g. $e^+e^- \rightarrow \gamma\gamma$ from inverse beta decay) becomes statistically disfavored. Larger arrays solve this problem by detecting not the individual charged tracks (or lepton/γ products) from ν scattering events, but Cherenkov [20] light from a relativistic secondary particle produced by a very high energy neutrino as it interacts in the detector volume. This technique of detecting a neutrino is used by the Sudbury Neutrino Observatory (SNO) [21], Super-Kamiokande [22], and the future, larger Hyper-Kamiokande [23], employing large tanks of water surrounded by optical detectors. All of these are dwarfed by the massive IceCube, which employs a cubic kilometer of ice at the South Pole as its detector volume. More on IceCube's detection strategy will be discussed in section 1.4.2, as well as the next generation of RF detection technology. The key to detecting neutrinos of the highest energies is likely RF detection of showers produced by neutrino primaries.

1.4 Cosmic-Ray and Neutrino Induced Cascade Detection Techniques

In this section we present the various detection techniques for high-energy cosmic-ray and neutrino induced cascades, starting with charged particle detectors and ending with RF detection strategies, including radar. For brevity, we neglect the lower-energy neutrino and cosmic-ray experiments which detect primaries below the 10-100 GeV scale.

1.4.1 Charged-Particle Detectors

From a detection standpoint, the simplest way to detect a cosmic-ray or neutrino induced cascade is to directly detect the charged particles produced by the shower. For example, an array of charged particle detectors on the ground can be used to detect the charged particles from a cosmic-ray

air extensive-air shower (EAS) [24]. This is an effective and well-understood method, employed by (among others) AGASA [25], HAWC [26], the Telescope Array (TA) [27], and the Pierre Auger Observatory [28], which gets its namesake from the the scientist who developed the EAS model, and spent most of his later years supporting humanitarian causes for the United Nations. The only restriction of such technology is that at a certain energy, up above 10^{19} eV, the flux of cosmic rays is so low that it becomes unlikely for a localized detector to be in the footprint of a large number of cascades, as discussed above. At these high energies, where the flux is on the order of $1/(km^2 * 100yr)$, two ancillary strategies may be invoked: either expand the surface array footprint (expensive, logistically challenging) or use a detection technology that does not rely on direct detection of the charged shower particles. The footprint of the original TA surface detector [29] is shown in Figure 1.7. A planned extension [30] will increase that coverage by a factor of 4, to roughly 3000 km^2 (roughly the size of the existing Auger surface detector), which is the geographic limit on the extension capability of TA, given the local topography. Therefore, some other technologies are needed to increase the statistics on the highest energy cosmic rays. There are basically only two alternative detection strategies for cosmic-ray and neutrino-induced cascades (which are themselves just sub-sets of the more general photon detection category): optical, and RF.

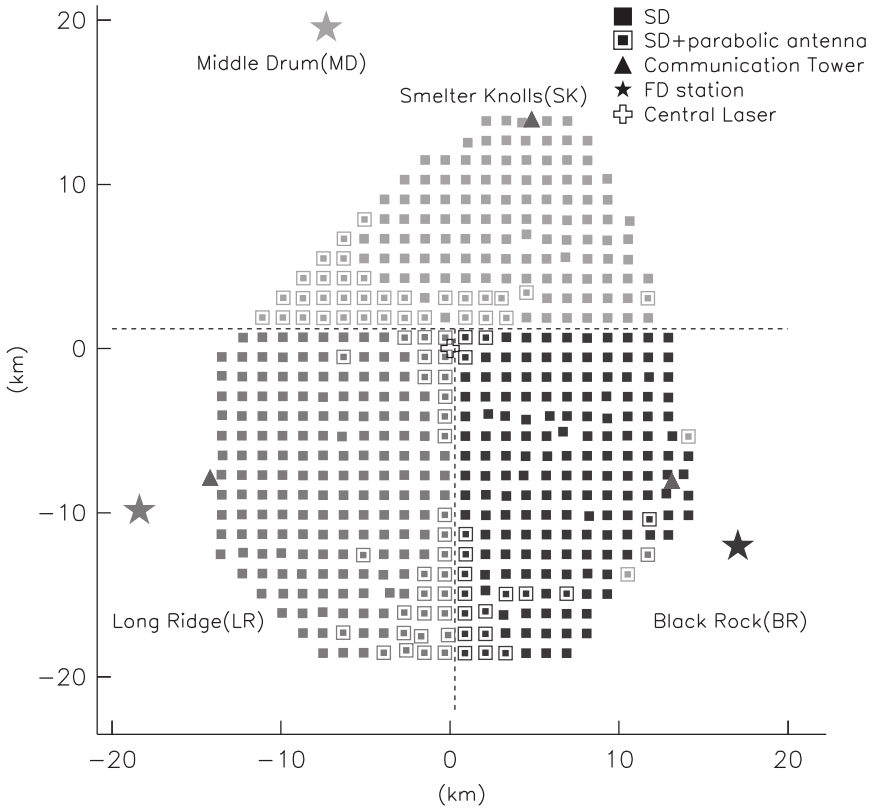

Figure 1.7: Original configuration of the Telescope Array surface detector. An extension is underway [30] to increase the area by a factor of 4 beyond this size. Also indicated are the fluorescence detectors and calibration light source. Taken from [29].

1.4.2 Optical Detectors

Optical detectors are yet a robust and effective detection scheme for cosmic-ray and neutrino-induced cascades. For air showers, florescence from nitrogen, excited by high-energy photons of an EAS, is detected by distant florescence telescopes such as Fly's Eye [31], the High Resolution Fly's Eye (Hi-Res) [32], and subsequent florescence detectors at the Telescope Array. They are able to track an EAS as it develops in the atmosphere and therefore provide excellent measurements on shower evolution. These detectors do not need to be in the footprint of a shower, which increases their exposure, but they do need absolute darkness to operate, which limits the duty cycle to $\sim$10%.

Cherenkov radiation is coherent emission, over a large frequency band, produced when charged particle velocities exceed the phase velocity of light in the medium they traverse. The radiation is

highly beamed on a cone, with a well-defined angle based on the refractive index of the medium n,

$$cos\theta_C = \frac{1}{n\beta}, \tag{1.1}$$

where $\beta = v/c$ is the ratio of the particle velocity to the vacuum velocity of light. Several observatories (built primarily for gamma-ray astronomy) are sensitive to the Chereknov light produced by cosmic ray showers in the upper atmosphere, such as MAGIC [33], VERITAS [34] and the future Cherenkov Telescope Array [35]. For neutrinos, similar Cherenkov radiation is produced as a neutrino-induced cascade traverses a dense medium, such as ice or water. Detection of such light [36] is the goal of experiments such as AMANDA [37], IceCube [19], ANTARES [38], and future KM3NeT [39]. IceCube currently has the highest energy neutrino detections at a few PeV [40]. Cherenkov emission is highly beamed, and so gamma-ray observatories do not improve on the footprint problem for UHECR, but for neutrino-induced cascades in ice or water, the array comprises a volume rather than an area, with increase arrival direction acceptance.

1.4.3 RF Detectors

The last category is RF detection of cosmic-ray and neutrino-induced cascades, a thorough review of which is given in [5]. The techniques for RF detection can be categorized into two groups: primary RF and secondary RF. Primary RF includes any technique for detecting radio produced by the particle shower itself. There are several distinct mechanisms which produce primary RF, which depend primarily upon the type of incident particle and the location of the shower (e.g. air versus ice, earth versus moon, etc). For cosmic-ray induced showers in air, the primary emission mechanism is from transverse currents in the shower produced by positive and negative charge separation in the geomagnetic field. Detectors such as LOFAR [41], LOPES [42], and AERA [43] detect such geomagnetic emission.

For neutrino interactions in dense media, the primary mechanism is the so-called Askaryan effect [44], which is coherent Cherenkov-like emission of radio from the negative charge excess

which builds up inside a cascade. This is primarily due to there being only electrons (not positrons) in matter; in addition to Compton scattering of atomic electrons into the advancing shower, shower positrons from pair production within the cascade will annihilate with electrons in the bulk, resulting in a lateral current which produces coherent radiation at RF wavelengths. In the 1990s it was suggested [45] and detailed [46] that a radio detector in ice could be sensitive to Askaryan radiation from ultra-high energy neutrinos. The Askaryan effect was first detected experimentally in silica at the Final Focus Test Beam at SLAC by Saltzberg and Gorham et. al. [47] and subsequently in different materials. The pioneering experiment for Askaryan detection of neutrinos (informed primarily by [46]) was the Radio Ice Cherenkov Experiment (RICE) [48], and current efforts ARA [49], ARIANNA [50], and ANITA [51] have not yet detected unambiguous signal from a neutrino cascade at the time of this writing. A visualization of the main primary RF emission mechanisms is shown in Figure 1.8.

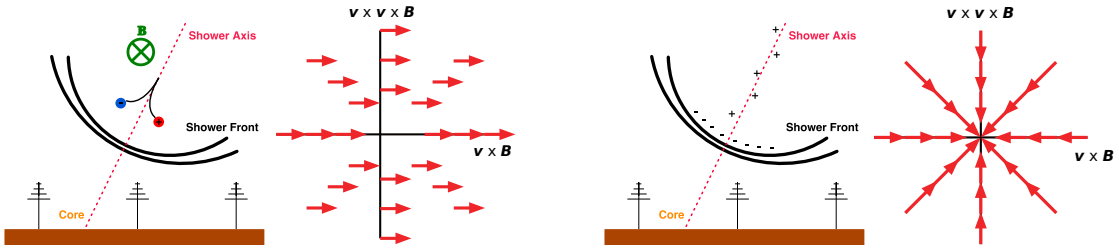

Figure 1.8: Graphical representation of the mechanisms and polarization of the main primary RF phenomena. Left: positive and negative particles in the shower separate in the Earth's magnetic field, leading to transverse currents relative to the shower axis. The electric field polarization lies along this separation vector, which aligns with the Lorentz force $\vec{v} \times \vec{B}$. Right: the Askaryan effect, in which a negative charge excess builds up as the shower progresses, resulting in a lateral current. Taken from [5].

For the geomagnetic emission, the electric field vector is aligned with the force felt by the particles as they move to the ground [52]. In fair weather, this is dominated by the earth's magnetic field such that the usual Lorentz force becomes simply $\vec{F} = q\vec{v} \times \vec{B}$ [53]. When a strong electric field is present in the atmosphere, the atmospheric electric field vector must be considered [54]. This is shown in Figure 1.9, where the measured electric field polarization is indicated by small arrows, and the Lorentz force vector $\vec{F}$ is shown for the case where it differs from 'normal' ($\vec{F} =$

$q\vec{v} \times \vec{B} \rightarrow \vec{F} = q(\vec{E} + \vec{v} \times \vec{B})$, e.g. in a thunderstorm $\vec{E} \neq 0$). For Askaryan emission, the E field is polarized radially out from the shower axis and perpendicular to the direction of propagation. This has been experimentally verified by [47] and [55] in sand and ice targets, respectively.

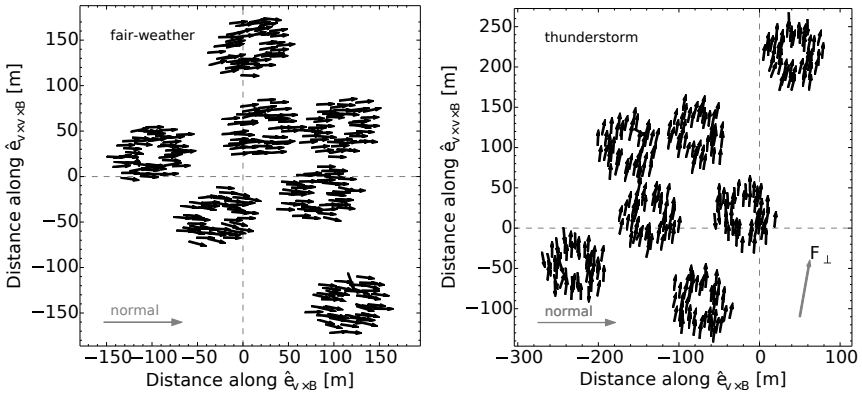

Figure 1.9: Measured polarization of the electric field from an EAS in the circular arrays of radio antennas at the LOFAR experiment. Left: the electric field polarization of an EAS during fair weather aligns with the geomagnetic polarization (indicated by 'normal'). Right: the electric field polarization of an EAS during a thunderstorm does not align with geomagnetic, having been rotated by strong atmospheric electric fields. Taken from [54] and adapted for formatting.

There is some interest in detection of the transition radiation signal from EAS, as the charged particles from a very high energy shower traverse the boundary between air and ice [56, 57]. Such transition radiation signals should be coherent at lower frequencies, and should radiate fairly isotropically. There is no dedicated experimental effort to detect such transition radiation at the time of this writing.

1.4.4 The Radar Method

Secondary RF refers to any passive RF method to detect a shower, such as radar [58]. Radar is currently the only secondary technique for detecting a high-energy particle shower. The description of the physics is straightforward: a particle shower in a medium will produce high energy particles that traverse that medium, kicking out ionization electrons from atoms in the bulk as they go. For high enough incident energies, this ionization may become dense enough to reflect radio. It is, effectively, a short-lived, small conductor. The Telescope Array Radar (TARA) [59] project was the

first dedicated experiment to try to detect the EAS from a cosmic ray interaction in the atmosphere using the radar method. TARA reported no signal [60], but placed a strong experimental limit on the model by Gorham [61]. Further details about TARA will be given in later sections. Several experiments [62, 63, 64] have sought to detect radar reflections from ionization deposits in a laboratory setting. Chiba et. al. have had very positive results for reflections from ionization deposits, albeit not from particle shower-induced ionization (see Chapter 2). The T576 experiment at SLAC sought to make the first direct measurement of radar reflection from the ionization produced by a particle shower, as previous experimental efforts at accelerators had too low primary energies to produce a detectable reflection. T576 will be discussed in detail in Chapter 5.

This dissertation focuses on the radar technique, where it has failed, and where it has the potential to succeed as a detection technology for high-energy particles. Chapter 2 will discuss the radar technique in general, with discussion of other radar-ionization interactions, including RF scattering from meteor trails and RF diagnostics in laboratory plasmas, as well as theory. Later chapters will go into detail about specific techniques to detect EAS in air (Chapter 3) and how to model neutrino-induced cascades in ice (Chapter 4). Finally, we discuss the T576 experiment, and a brief discussion of future prospects for radar systems.

Chapter 2

History, Theory, Experiment, and the Case for Radar

2.1 Radar Basics

Before going any further, we must describe what is meant by 'radar'. In general, radar (archaically stylized RADAR, initially standing for RAdio Direction And Ranging, or RAdio Detection And Ranging [Wikipedia]) is the technique of broadcasting a radio signal and detecting the reflection of that signal using a receiver. The most common types of radar (air traffic control, military, police, weather) fall into the category of mono-static radar, where the transmitter and receiver are co-located. In many cases, they are even the same antenna, switching rapidly between broadcast and receive mode. The properties of the received signal allow the radar operator to infer a great deal about the object(s) from which reflection has occurred. Frequency shifts indicate relative velocity. The amount of power received for an object at a known distance gives the so-called radar cross section, that is, the effective cross-sectional area of reflecting surface on an object (not to be confused with the physical cross-sectional area of the object itself). The so-called mono-static radar equation is,

$$P_r = \frac{\eta P_t \lambda^2 \sigma}{R^4}, \tag{2.1}$$

where P_r, P_t, λ, σ, and R are the power received, power transmitted, the interrogating wavelength, radar-cross section, the separation vector between antenna and object, respectively. The constant η contains the receiving and transmitting antenna characteristics and system losses, and takes many different forms in different applications. We will present some of these in later sections. Equation 2.1 can be solved for cross section for an object at a known distance, or if that is known, the distance to the object.

The second category of radar, that which cosmic-ray and neutrino induced cascade detection falls into, is known as bi-static radar. The basic principles are the same, except that the transmitter and receiver are not co-located, as in mono-static radar. This modifies Equation 2.1 such that $R^4 \to R_r^2 R_t^2$, where the subscripts r and t indicate distances from object to receiver and transmitter, respectively. This setup is particularly appropriate for tracking rapidly moving projectiles, since the Doppler shift f' is proportional to the change in overall path length of a radar signal, that is,

$$f'_{mono} = \frac{1}{\lambda}\frac{dR}{dt} \quad \to \quad f'_{bi} = \frac{1}{\lambda}\frac{d}{dt}(R_r + R_t), \tag{2.2}$$

for a transmitter wavelength λ. For a long baseline between receiver and transmitter, this derivative in the bistatic case is slowly varying, minimizing the frequency shift. The shower front of an EAS moves relativistically, so a long baseline ensures that Doppler shifts (from the shower front or the trailing ionization column) stay within the sensitive bandwidth of a detector system. This Doppler shift can be parameterized in terms of the typical angles of the bi-static setup,

$$f' = 2 f_0 \cos\delta \cos\frac{\beta}{2}, \tag{2.3}$$

which are defined in Figure 2.1. The angle δ is the angle between the momentum direction of the object and the bisector of the bi-static angle β, which is defined as the angle between TX and RX on the TX-object-RX plane.

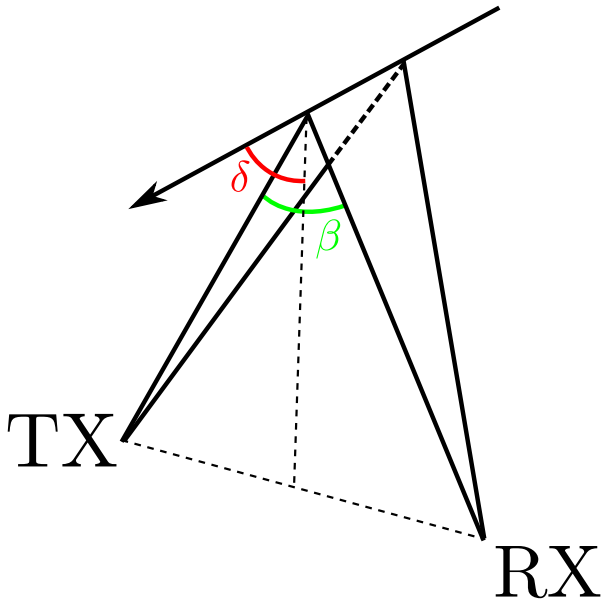

Figure 2.1: The typical angles of a bi-static radar configuration.

The transmitted RF of radar systems can be modulated in myriad ways, but for the case of cascade detection presented here, we only consider continuous-wave (CW) radio. This is because for EAS in air or cascades in ice, the expected radar signal has a characteristic shape [65, 66], which is easily distinguishable from anthropogenic electro-magnetic interference (EMI), making modulation in these cases redundant.

Of course, one of the most important considerations in calculating the return signal from a radar interrogation is, what exactly constitutes an object? In order for radio to be reflected, there must be some collection of free or freely-moving charges. For the radar detection of an airplane, for example, the physical limits of the object are clear-the freely moving charges responsible for reflection are those within the conducting metallic material of the vehicle. For the case of a meteor column or a particle cascade, the picture is far more complicated. There is a conspiracy of source properties and ionization properties which comes together to define the reflecting system.

Consider a meteor trail, which is the ionization of the atmosphere by a flying meteorite. The meteorite itself is perhaps the size of a grain of sand, yet it produces a column of ionization kilometers long, with a density such that, at night, the energy lost in the visible spectrum (which

comprises a small fraction of the total) is enough for it to be visible from the ground. Such an ionization column is obviously not monolithic, but instead comprised of lateral and longitudinal density gradients. So how do we define what the 'size' of the ionization column is? Is it the limit of the physical extent of the ionization distribution? Is it the physical extent of the density above some limit, such that, for example, the trail can produce enough visible light to be seen?

In radar literature (specifically meteor scatter, which will be discussed below) the cross section is generally defined by the extent of the so-called overdense region. This defines the region in an ionization cloud which is dense enough to totally reflect incident RF (that is, incident RF cannot penetrate it). Regions of lower density, which still may scatter incident RF, just not fully *coherently*, are called underdense. We will now derive the expression that delineates between the two, the so-called plasma frequency.

There are many ways to derive the plasma frequency, but let's first assume some collection of 'free' charges q, as may be found in a cloud of ionization as described in section 1.4.4. Let's assume there are N charges within some volume such that we can describe the collection in terms of a number density $n_e q$. Let's further assume that, within this volume, the charges are close enough together such that they move collectively under some external force, such as a harmonic driving force from incident RF, $q\mathbf{E} = qE_0 \exp[i(\mathbf{k}\cdot\mathbf{r} + \omega t)]\hat{\varepsilon}$, for a polarization vector $\hat{\varepsilon}$. We intentionally do not define 'close enough' at this point.

We can write down a current density of this collection of charges,

$$\mathbf{J} = n_e q \dot{\mathbf{x}}, \tag{2.4}$$

which is simply put in terms of the velocity $\dot{\mathbf{x}}$ of the collection of charges. We can then rearrange Maxwell's equations to obtain

$$\nabla^2 \mathbf{E} = \frac{1}{c^2}\frac{\partial}{\partial t}\left[\frac{\partial \mathbf{E}}{\partial t} + 4\pi\mathbf{J}\right], \tag{2.5}$$

which, after plugging things in, gives

$$\nabla^2 \mathbf{E} = \frac{1}{c^2}\left[\frac{\partial^2 \mathbf{E}}{\partial t^2} + 4\pi n_e q \ddot{\mathbf{x}}\right]. \tag{2.6}$$

Using our harmonic electric field as above, we can write

$$m\ddot{\mathbf{x}} = qE_0 \exp[i(\mathbf{k}\cdot\mathbf{r} + \omega t)]\hat{\varepsilon} \tag{2.7}$$

for the equation of motion of the collection of charges, and then, using eq. 2.6, we get,

$$k^2 = \frac{1}{c^2}[\omega^2 - \frac{4\pi n_e q^2}{m}]. \tag{2.8}$$

The quantity

$$\omega_p = \sqrt{\frac{4\pi n_e q^2}{m}} \tag{2.9}$$

is called the plasma frequency, and it can be understood in several ways. Firstly, it is clear to see in eq. 2.8 that if the angular frequency ω of the electric field is lower than ω_p, the wave number k becomes purely imaginary. If k is expressed as a complex number, this imaginary part represents an exponential damping of the field, that is, waves with frequencies lower than the plasma frequency cannot propagate within the volume of charges we just described. They will instead be reflected.

More intuitively, we can make a simple physical argument. When starting the derivation, we arbitrarily decided that there existed some volume where charges were close enough to oscillate collectively in some external harmonic force. It is clear that in order for this to occur, the harmonic force must be low frequency (long wavelength) relative to the extent of the volume, otherwise different parts of the volume would oscillate out of phase from one another, and the coherent motion would be destroyed. The plasma frequency is that cutoff-above the plasma frequency, the collective motion is no longer observed, and scattering becomes less coherent.

At the point $\omega = \omega_p$, the critical number density $n_c = \omega^2 m/4\pi q$ defines the number density at

the overdense/underdense boundary. This is the boundary of coherent reflection: for an airplane, it's just the outline of the fuselage of the airplane. For a particle shower, it is more involved, and the picture is more like the cartoon of Figure 2.2, adapted from Raizer [67], where for some interrogating frequency, the wave penetrates until it reaches n_c, where it is reflected.[I] Here the spacing of horizontal lines indicates the number density.

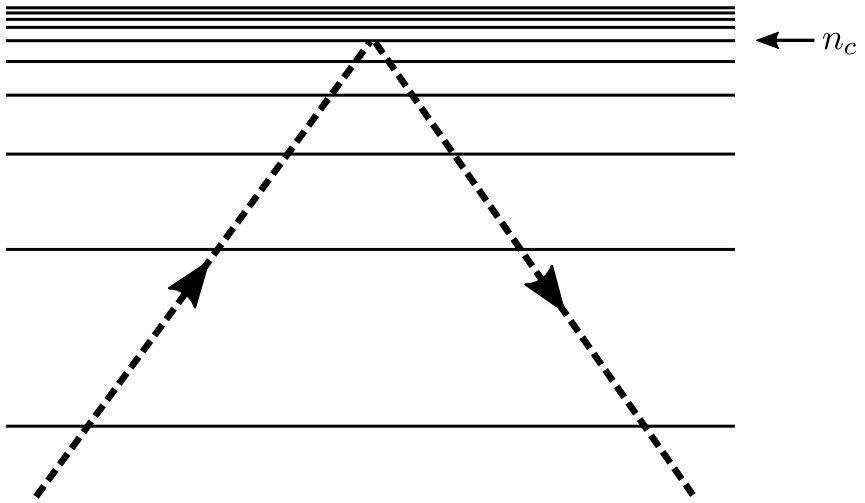

Figure 2.2: Illustration of the effect of the plasma frequency. Density of ionization is shown by the spacing of horizontal solid lines. The dashed line is an interrogating wave of some frequency. The wave is reflected when the density reaches n_c. Adapted from [67].

With these basics in mind, we can now look at some specific cases of radar/ionization interactions, and the history leading up to radar based detection of cosmic ray and neutrino induced cascades.

2.2 History and Model Development

In 1941, Blackett and Lovell suggested that the EAS from cosmic rays may explain "transient ionic clouds" which cause "sporadic radio reflexions" [58] in lower levels of the atmosphere, which had been observed in the course of early atmospheric radio research [68, 69, 70, 71]. The source of sporadic reflections from the upper atmosphere was soon thereafter attributed to meteors, a

[I] It is important to note that there is of course a gradient region between overdense and underdense, and nothing is exactly as clearly delineated as presented here. But the classification is useful, in general.

review of which is given in [72], and discussed further in section 2.3. The determination of the source of the low-altitude reflections remains inconclusive, but it sparked an interest in considering whether or not radar could be used to detect the dense column of ionization within an EAS. Blackett and Lovell first approximated that air showers from $E = 10^{16}$ eV were detectable with the extant experimental apparatus. However, no conclusive evidence of EAS reflections were made in the next 20 years. In 1960, a more detailed calculation indicated that the energy threshold was some 4 orders of magnitude higher, owing to collisions within the EAS ionization column. Experimental efforts at that time were again inconclusive.

In 2001, Gorham [61] produced the most detailed model of the scattering problem up to that point, in which he considered the evolving shower ionization density profile. He used a radar model from [73], following [74], called the 'thin-wire' approximation to model the ionization column of an EAS. In this thin-wire model, the radar cross section σ_{rcs}^{TW} is calculated for a cylinder of radius$\ll$length. It was calculated that σ_{rcs}^{TW} for showers of high energy ($\geq 10^{18}$ eV) would produce measurable bi-static radar returns. After this, the TARA experiment [59] sought the first radar reflections to be confirmed by a coincident measurement, by co-locating a bi-static radar system with the Telescope Array surface detector.[II] After a dedicated analysis, TARA put a limit on the Gorham model of $\mathcal{O}(10^{-4}\sigma_{rcs}^{TW})$ [60].

Somewhat concurrently to the TARA results, in 2014 Stasielak et. al. [76] presented a more detailed calculation of the air shower problem, incorporating detailed treatments of the atmosphere, noting that the free electron lifetime was $\mathcal{O}$(10-100 ns) [77], as in Figure 2.3. This lifetime τ is a measurement of the time it takes for the density of free electrons to fall by a factor of $1/e$. Schematically, the shower front of an EAS moves relativistically, trailing an ionization column behind. For $\tau =$100 ns, the density of the column 30 m behind the shower front will be a factor of $1/e$ lower than the front. The Moliere radius, in which 90% of the shower particles are found, is $\mathcal{O}$(10 m) for air at EAS altitudes. Therefore, an EAS column of radius r and length l in air

[II]Previous experiments had measured short bursts of radio originating in the atmosphere [75] with the correct properties for EAS reflections during dedicated EAS searches, but these results were never confirmed by a known secondary cosmic-ray detection technique.

has a profile such that $r \approx l$. In [74] it is noted that the thin-wire approximation is only valid for $2l/r > 100$, which is not met in general for the EAS case due to short lifetimes in air. This does not necessarily invalidate the radar technique for EAS, but it does limit the efficacy of the thin-wire model to describe the profile of the EAS ionization plasma. Within both the disk and the trailing column there are strong density gradients in the lateral and longitudinal dimensions, so an approach like [76] which treats the distribution more generally is likely a better approximation for σ_{rcs}. More on the current feasibility of EAS detection via radar is given in Chapter 3.

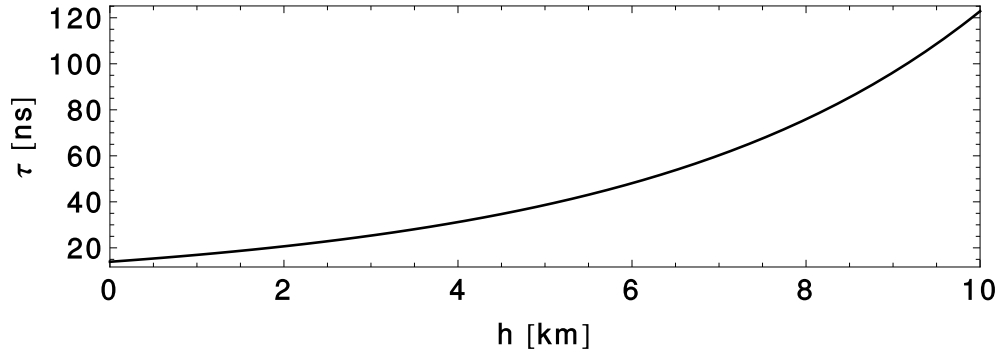

Figure 2.3: The mean lifetime of the ionization electrons in air for EAS altitudes. Taken from [76].

Around the same time, Chiba et. al. were making efforts to detect radio scattering from ionization deposits in dense media, to determine whether such a technique could be viable as a detection strategy for ultra-high energy ν in dense material [62, 78]. Though they did not use a particle shower to produce the ionization, their results demonstrated that radio reflections could indeed be detected from ionization alone in a dense material such as rock salt. On the theory side there have been advances in describing and modeling such neutrino induced cascades, the details of which will be presented in section 2.6.1 and Chapter 4. Several experiments [63, 64] including the very recent T576 (Chapter 5) have sought to detect the radar signal under laboratory conditions.

2.3 Meteors

The most intuitive readily-available (albeit possibly misleading, see below) picture for scattering radio from an ionization trail comes from meteor scatter. Indeed the model in [61] was primar-

ily built upon radio echo phenomenon. In meteor scatter, as a meteorite ablates in the upper atmosphere (80-100 km) the energetic material from the rapidly moving meteorite ionizes the surrounding atmosphere. The meteorite itself creates a moving front of ionization, but the trail is quasi-stationary, made up of 'cold' ionization electrons. Because the meteor is so massive (relatively, of course, most 'large' meteorites are the size of a grain of sand), the ablation can continue for many hundreds of meters, even kilometers, ionizing as it goes. Furthermore, because the atmosphere is less dense at high altitudes, the free electron lifetime is quite large, and so the longitudinal density gradient permits high ionization densities out to large distances. In fact, the lifetime is so large, that the primary reason for loss of return signal from a meteor trail is radial diffusion of free electrons through thermal motion [72]. For HF interrogation, some radar returns from larger meteor trails (those which would be clearly visible at night with the eye) can last for several minutes.

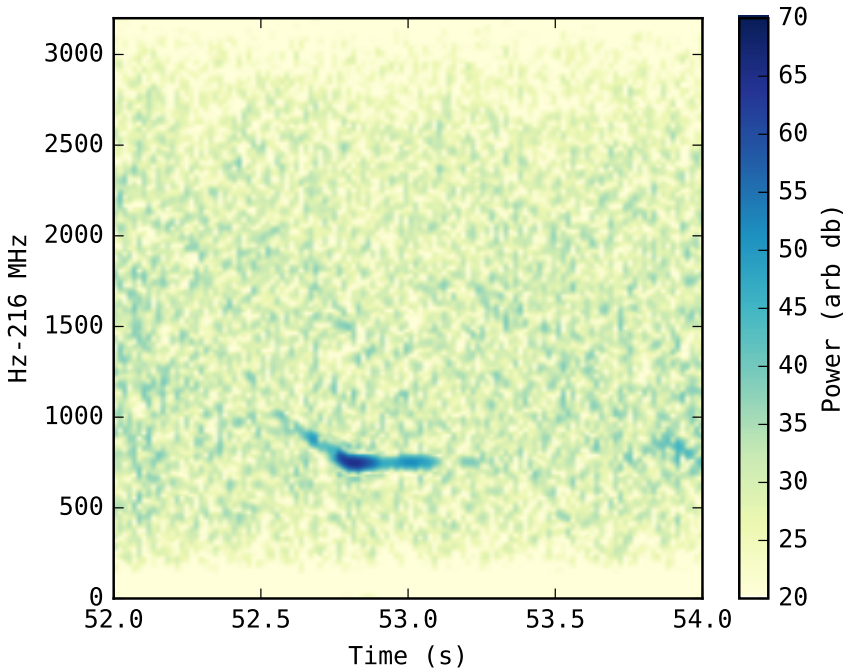

Figure 2.4: Spectrogram of a meteor detected at KU during the 2012 Perseids. ∼750 Hz corresponds to the carrier, having been downshifted and sampled at audio (8k) rate. Visible are the Doppler-shifting 'head-echo' and the stationary return from the persistent trail.

The two most prominent features of a meteor scatter signal are the head-echo and the trail, shown in Figure 2.4. The head echo is a reflection from the moving ionization front of the meteor

that Doppler shifts a sounding signal accordingly. Some study of the properties of the head echo are given in [79, 80, 81], with an extensive analysis of one particular radar observation given in [82]. The trail reflection is a reflection from the quasi-stationary ionization trail that is left in the wake of the meteor. When we talk about the reflection from the tail, we almost invariably refer to overdense scattering, that is, scattering for which $\omega < \omega_p$. The tail returns primarily CW at the carrier frequency, with slight Doppler shifting from drift in the atmosphere. The slight drift in the tail, caused by atmospheric wind, can be measured with sensitive enough radar systems, as shown in Figure 2.5, but in general, the trail is effectively stationary.

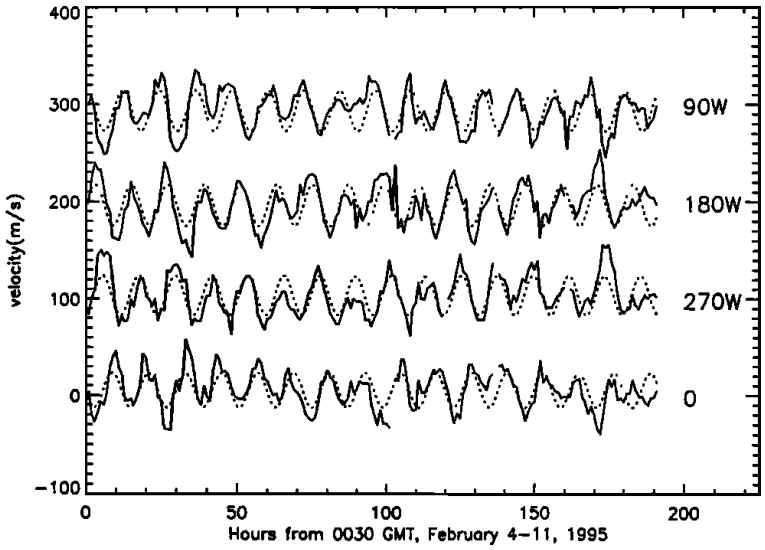

Figure 2.5: Measurement of a diurnal variation in Mesospheric winds above the south pole, as measured using slightly Doppler-shifted radar returns from sporadic meteor tail reflections. Taken from [83].

2.3.1 Comparison to UHECR

Bakunov et. al [84] calculated that the Doppler upshift shift from reflection off of the ionization front of a UHECR, for a short-baseline bi-static setup, would be roughly 3 orders of magnitude, e.g. a received frequency of 1 GHz for a sounding frequency of 1 MHz. In this way, it is qualitatively identical to the shifted head-echo of a meteor, but the Doppler shifts of the received signal from

UHECR are far more drastic due to the relativistic velocity of the shower front.

Similar to the ionization trail of a meteor, the trail of a cosmic-ray shower is effectively stationary. However, as mentioned previously, the free-electron lifetime at EAS altitudes ($\sim$10 km, $\mathcal{O}$(10 ns)) are many orders of magnitude shorter than at meteor ablation altitudes ($\sim$100 km, $\mathcal{O}$(minutes)). This results in an effect where reflections from different parts of the stationary tail reflect to the receiver in such a way as to produce an *effective* Doppler shift, which will be discussed further below. Therefore, a reflection from a meteor trail is not a good analogue for the reflection from a UHECR ionization column due to this difference in the free electron lifetime.

2.4 RF Interactions with Plasma

There are many rich physical systems where ionization plasmas and RF interact. One such system is fusion reactors, where the scattering of RF and lasers from the dense plasma within a tokamak is used to quantify the plasma number density [85]. Another is the ionosphere, where long plasma lifetimes can result in a dense enough background ionization to reflect low to medium frequency waves. Yet a next is arc discharge, such as lightning, sparks, and laboratory plasmas. Not only is RF scattering from such plasmas interesting, but the RF produced by transient plasmas can be useful in physical applications. The NASA-supported HiCal [86] instrument, for example, was a small payload built to fly on a balloon and produce a high voltage RF pulse to be detected by the ANITA instrument. ANITA, the Antarctic Impulsive Transient Antenna, is a radio interferometer array of 48 dual polarized antennas attached to a balloon that floats in the stratosphere above Antarctica to listen for Askaryan signals from neutrino interactions in the ice. This high amplitude and impulsive RF pulse from HiCal served two purposes:

1. To quantify the surface roughness of the antarctic ice.

2. As a calibration source for the ANITA instrument.

The primary event topology for ANITA is a shallow angle neutrino interaction in the ice producing RF which propagates up through the atmosphere to be detected. The instrument is also

sensitive to the reflected geomagnetic signal from downgoing UHECR reflected back up off the ice.

The characteristics of both of these signals, as received by ANITA, depend strongly on the surface of the antarctic ice. Both signals breaking out through and reflecting off of the surface will be altered by the surface, and a characterization of its roughness in ANITA's band is important. Two HiCal missions have flown, one with both ANITA-3 and ANITA-4. HiCal produces a high voltage pulse, emitted through a broadband bi-cone antenna, which can be detected by ANITA at least out to 700 km. ANITA detects each HiCal pulse twice-once directly, and once reflected up off of the surface. A comparison of the two provides a reflection ratio as a function of angle and frequency. Along with measurements of solar reflectivity, The HiCal results, shown in Figure A.2 comprise a measurement of the surface reflection ratio which shows deviation from previous theoretical models of surface roughness. Current models [87] have much better agreement with the HiCal data, which now provides a comprehensive measurement of the reflection coefficient as a function of angle, in the 200-600 MHz band.

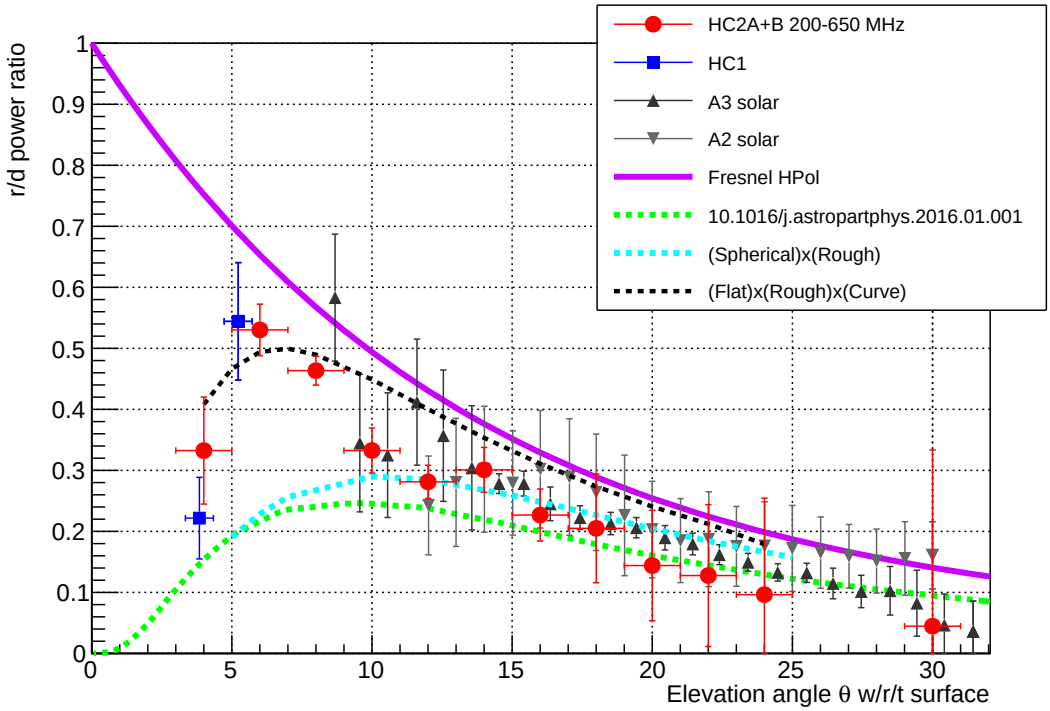

Figure 2.6: The reflected/direct power ratio as a function of angle for the antarctic continent, as measured by several instruments. The black curve is the most recent theoretical treatment. Taken from [87]

More details about the HiCal instrument are given in Appendix A.

2.5 TARA

The Telescope Array RADAR (TARA) project was the first dedicated experimental effort to detect UHECR using radar. A re purposed 40 kW (nominal) television transmitter broadcast CW at 54.1 MHz through a phased array of 8 Yagi-Uda antennas into the air above the Telescope Array surface detector array from the east. To the West of the TA surface detector array, roughly 40 km away on Long Ridge, Millard County, UT, USA, were positioned several log-periodic dipole antennas with a sensitive bandwidth from 50-100 MHz. Three of these antennas were connected to the primary TARA data-acquisition system (DAQ), described in detail in [59]. A further two were connected to an independent DAQ called the remote stations. If an EAS of sufficient energy were

to occur within the region illuminated by the transmitter, the broadcast signal would be reflected to the distant receivers and captured by the various DAQs. The EAS would also be detected by TA, so that any radar report would be validated by coincident detection. Now we will briefly describe the experimental effort and results.

2.5.1 FD Trigger

The Telescope Array has three florescence detectors (FD), as described in a previous section. One of these, located on Long Ridge, overlooks the sky above the TA surface detector from the west. Of the various trigger techniques employed by TARA, the simplest was to take a trigger from the FD, and use that to trigger an RF capture [60]. Since some fraction of FD triggers represent true EAS events, this system guaranteed that radar data was captured when an EAS was present.

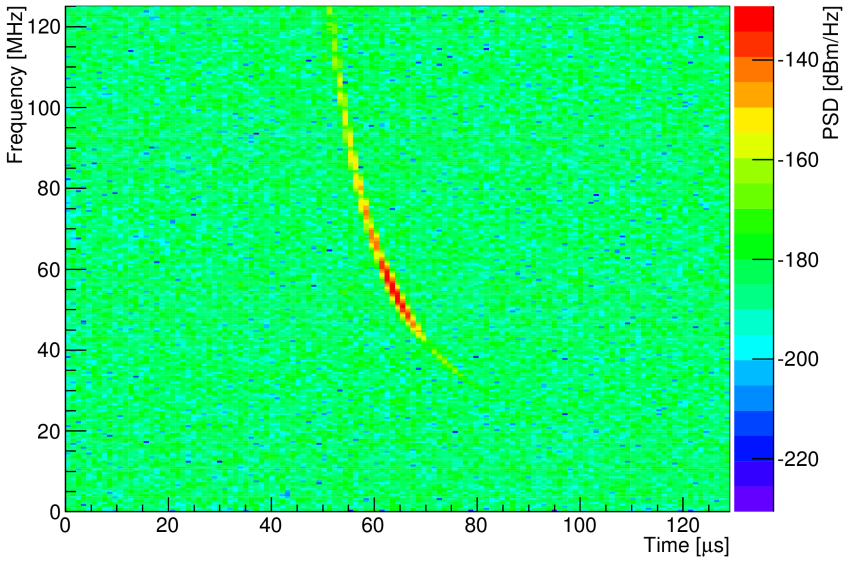

Figure 2.7: A simulated radar reflection template used for the matched filter signal search from FD-triggered data described above. Taken from [60].

For the analysis, a matched filter technique was used to look through the FD-triggered dataset. In this method, individual simulated signal templates for each true CR event were constructed using shower information from TA. These simulated templates included all geometry, antenna, and front-

end characteristics of the TARA receiver, and were specific to each true CR event according to the thin-wire model. An example is given in Figure 2.7. These templates were then cross-correlated with their corresponding triggered TARA event. Candidate events were selected based on their peak cross-correlation with the matched filter. This analysis yielded no results, and set an upper limit on the thin-wire cross section model at $\mathcal{O}(10^{-4}\sigma_{rcs}^{TW})$. This is a strictly model-dependent limit, however, because the templates were constructed using the thin-wire model.

2.5.2 Matched Filter Trigger

TARA also implemented a matched filter trigger, analogous to the signal search method described above, where instead of using a specifically tailored template for each event, a bank of template signals were cross-correlated continuously with the incoming data stream, and high cross-correlation values would register a trigger. At the time of this writing, results from this technique have not been published.

2.5.3 The Remote Stations

Desiring an independent triggering scheme and a more isolated environment, a third detection strategy was developed called the remote stations [65]. This was a standalone DAQ which triggered on the expected signal from an EAS. While this trigger was model-dependent as well, the system could trigger on a wide variety of different chirp-rates (as described in section 3.2.1). There were 4 total deployments of the remote stations. The data from the first two deployments, from June 2015-September 2015 was corrupted by a hardware fault, unfortunately rendering it unusable [66]. The data from the third deployment, from Feb-April 2016, contained no directly coincident events with the TA surface detector. An analysis of the remainder of the data is forthcoming. The fourth deployment was not a part of the TARA experiment, but instead the remote stations were re-designed to run parasitically off of terrestrial FM radio broadcasts (as opposed to the dedicated TARA transmitter). More on the remote stations is presented in Chapter 3;

2.6 The Case for Radar

At this point we have discussed radar techniques in air and in dense media. Though the outlook for radar detection of EAS in air is not as optimistic as it was several decades ago, it seems feasible that a neutrino interaction in a dense material, such as ice, could produce a shower dense enough to be detected. The relative RF transparency of ice makes it a useful place for radio studies, as evidenced by the Askaryan experiments throughout the polar regions. The free electron lifetime has been measured as a function of temperature in ice [88] showing it to be the same order of magnitude as at EAS altitudes, $\mathcal{O}$(10 ns). But due to the increase in density of the material, the electron density is similarly 3 orders of magnitude greater. Some authors [89] cite a free proton plasma lifetime of >100 ns which could potentially reflect considerable radio for an extended duration, more analogous to a stationary meteor trail.

There are two large advantages of radar over Askaryan methods for neutrino detection at the highest energies. The first is aperture, and the second is variable transmitter output power. The Askaryan signal is highly forward beamed on a cone of order degree width. So even if a rare neutrino event occurs within the sensitive volume of an Askaryan detector, it still must have a favorable geometry such that the cone intersects a receiving antenna. The radar method does not suffer from this aperture restriction. While there is an increase in the scattered amplitude at the specular reflection point, there will be scattering into a far greater amount of solid angle than the Askaryan signal. Additionally the scattered signal amplitude is directly proportional to the energy of the shower and the output power of the transmitter. To lower the effective energy threshold of a detector, the transmitter amplitude can be increased. Such advantages make the radar detection of neutrinos in ice a worthwhile pursuit, at least until, as in air, the method is sufficiently exhausted.

2.6.1 Current Models

There are several current models (besides the one here presented in Chapter 4) [89, 90] treating the problem of radar reflections in the ice. These deal with the macroscopic shower and build up

a physical picture of coherent scattering from integrated particle distribution functions. Here they employ the Nishimura-Kamata-Greisen (NKG) parameterization [91] (as given in [90]) for the longitudinal profile of a shower, plotted for the case of a shower in ice in Figure 2.8. We note that the authors neglect the Landau–Pomeranchuk–Migdal (LPM) effect [92, 93] in the longitudinal profile. This effect, detailed for the radio problem in [94] and [95], is a suppression of low-energy bremsstrahlung and pair production in showers at very high energies, resulting in an effective lengthening of showers in the longitudinal dimension. This effect would have minimal impact on the radar problem as the extended tail of the distribution at high energies has a low number density relative to shower maximum, and therefore will not be part of the overdense scattering obtained below. The position of shower maximum moves longitudinally approximately 1 meter for every decade in energy, and the peak number of shower particles goes as the energy of the primary.

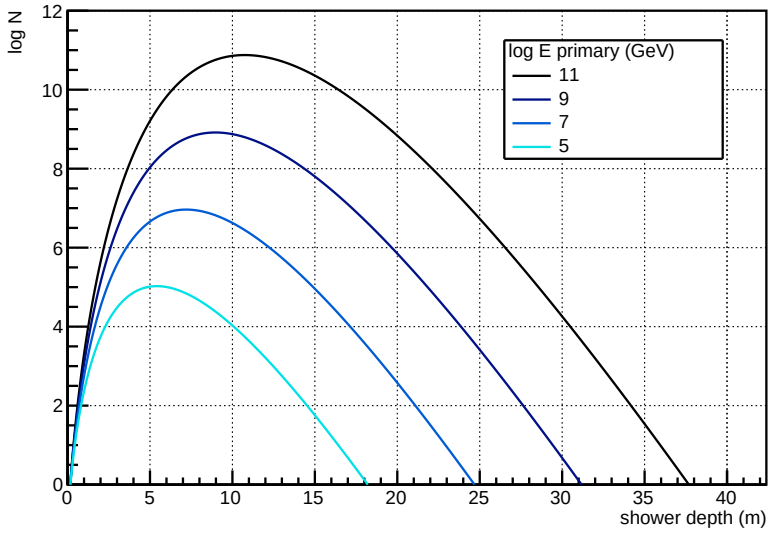

Figure 2.8: Longitudinal shower profiles for various primary energies as given by the NKG approximation as presented in [90].

The lateral distribution is similarly approximated using a parameterization for air showers with densities modified for the case of an in-ice shower. Once the shower profile is established, they build up a formalism for calculating the overdense radar scattering cross section σ_{od}, which we will elucidate here.

The model is built upon considering the ionization distribution as a series of concentric cylindrical areas of approximately static density, even though the distribution as a whole varies in number density in both the lateral and longitudinal dimensions. Each cylinder can be thought of as a shell of thickness Δx where the number density (and other parameters of the scattering) are constant over that length.

Because all electromagnetic waves are polarized, there must be an accounting of the efficiency of scattering from an object of some size with radio polarized in some direction. To solve this problem, the authors use a geometrical factor $f_{geom} = (1 - \vec{e_{tc}} \cdot \vec{e_c})(\vec{e_t} \cdot \vec{e_c}) f_{diff}$, where the vectors $\vec{e_{tc}}$, $\vec{e_c}$, and $\vec{e_t}$ are the unit vectors along the line separating the transmitter and the cascade, the direction vector of the cascade, and the polarization of the transmitter, respectively. To account for the position of the receiver the authors incorporate a Fraunhofer diffraction factor for an interrogating wavelength λ which they define as

$$f_{diff} = \frac{\text{sinc}^2[(\pi L/\lambda)\sin\alpha]}{< \text{sinc}^2[(\pi L/\lambda)\sin\alpha] >}, \tag{2.10}$$

where L is the longitudinal dimension of the cylinder and α is the angle at which the cascade reflection is 'viewed' by the receiver relative to the specular reflection point. The expression f_{diff} is given as a relative intensity of the scattered signal relative to the isotropic. Hence, there is an expected maximum in the reflected power at the specular point $\alpha = 0$ ($\theta_i = \theta_r$), with the power falling off as $|\alpha|$ increases. The assumption that f_{diff} may be approximated in this way relies on the longitudinal dimension of the plasma being larger than the lateral extent, which in general is only true for long plasma lifetimes, as discussed above. However plotting f_{diff} for several different longitudinal lengths of the plasma column, as in Figure 2.9, shows the expected behavior, where the intensity pattern of the reflection becomes more isotropic as the column becomes shorter.

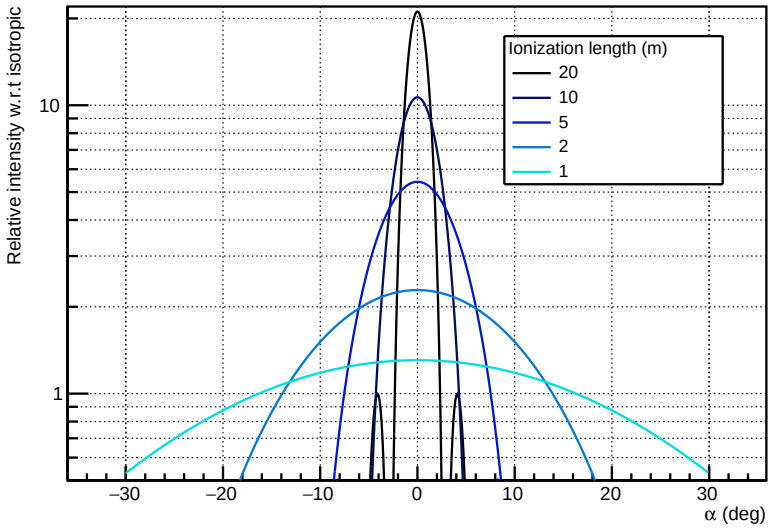

Figure 2.9: Relative intensity of a reflection from overdense regions of different longitudinal dimension, with respect to isotropy, as a function of the angle away from the pure specular point $\theta_i = \theta_r$, using an expression from [90].

The authors then continue and build up a model for calculating σ_{od} by incorporating a function for the skin depth f_{skin} for reflection off of each cylindrical shell. As described in a previous section, this is a function of the plasma frequency ω_p. At some radial distance r_{od} from the shower axis, the number density will become low enough such that the sounding RF will penetrate all shells with radius $r > r_{od}$, and so the overdense region is calculated as a sum over all N cylindrical shells with $r < r_{od}$. That is,

$$\sigma_{od} = \sum_{i=1}^{N} A^i \times f_{geom} \times f_{skin}^i, \tag{2.11}$$

where A^i is the area of the i-th cylinder, and incorporates a factor of .5 owing to the fact that the area itself is more of an ellipsoid than a cylindrical shell. Using this model, they are able to calculate a detector sensitivity limit for an in-ice experiment, given in Figure 2.10. They show two curves in the figure for different 'scattering efficiencies' η, which is a measure of, essentially, all the unknowns remaining in the problem. Specifically, the plasma lifetime and collisional rate. The sensitivity given is better than the projected ARA-37 sensitivity at 10 PeV, even for a non-optimized

detector configuration. Adding more stations and optimizing for the geometry of a shower would improve the sensitivity.

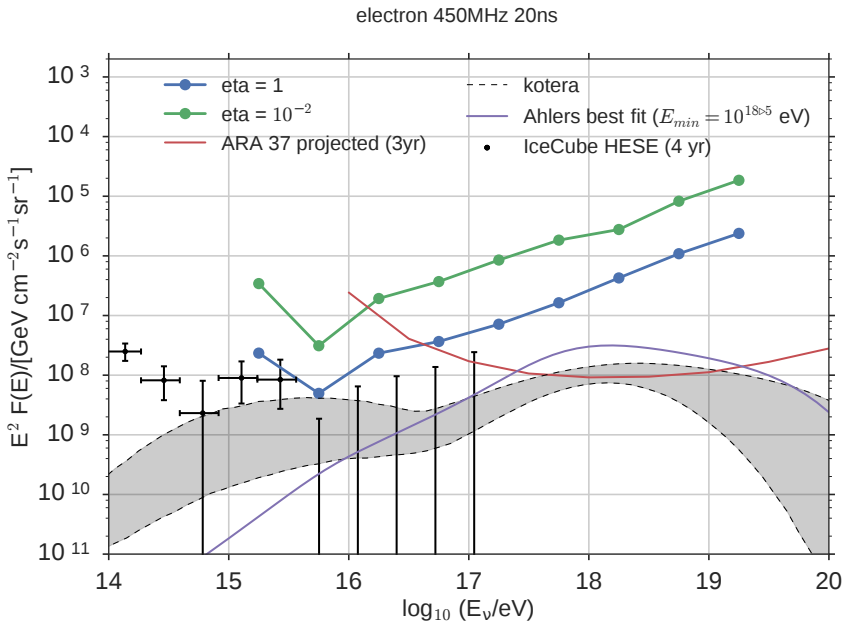

Figure 2.10: The detector sensitivity for a radar setup as presented in [90] for two different 'scattering efficiencies' $\eta = 1$ and $\eta = 10^{-2}$. Taken from [90].

While certainly a more robust model than any previous, this model still depends on an approximation of the shower ionization profile, and considers static geometric configurations as reflectors from a plasma which is developing very rapidly in time and space. While this may indeed be an accurate way to model the shower, for completeness, one could build up a model for scattering from individual particles within an ionization cloud which could be run within a monte-carlo program. Therefore, in Chapter 4 we present a new particle-level model specific to the neutrino induced cascade problem. Our model will focus more on obtaining the time-domain signals from a radar scatter, so as to inform potential trigger design.

Present in both models, however, is an increased sensitivity over both optical and Askaryan at $\mathcal{O}$(10-100 PeV). IceCube is proposed to expand in the coming years, but the primary case for radar is the potential to attain an analogous sensitivity to an expanded optical array at a fraction of the cost. More on the sensitivity of the radar method for an optimized detector configuration is

presented in Chapter 4.

Chapter 3

EAS Detection with the Remote Stations

This chapter is adapted from a paper published in Nuclear Instrumentation and Methods in Physics-A, https://doi.org/10.1016/j.nima.2018.02.051:

Implementation of a custom time-domain firmware trigger for RADAR-based cosmic ray detection

S.Prohira[1], D.Besson [1,2], S.Kunwar[3], K.Ratzlaff[1], R.Young[1]

[1] University of Kansas, Lawrence, KS, USA

[2] National Research Nuclear University, Moscow Engineering Physics Institute, 31 Kashirskoye Highway, 115409, Russia

[3] DESY, Zeuthen, Germany

3.1 The Remote Stations

The TARA remote stations (RS) [65] were an autonomous detector system that triggered on the expected reflected signal from the EAS. Developed with the instrumentation design lab (IDL) at KU, the RS featured custom electronics, firmware, and software, were solar powered, and remotely controllable via a microwave ethernet link. The RS were proposed during the TARA experiment to provide complementary measurements to the primary DAQ, described above. Such a system was feasible in the area around Delta, UT, due to the relatively low levels of anthropogenic backgrounds in the vicinity. They were implemented first in a pilot deployment in 2013-2014, using a prototype station and a simplified version of the electronics called the Transient Detector Apparatus (TDA) which simply monitored transient excursions above some threshold per unit time at the proposed RS site. This prototype station was solar powered and also served as a test of the power distribution system and the System Health Monitor (SHM), a remotely accessible http interface to monitor PV voltage, current draw, enclosure temperature, TDA rate, and various other system diagnostics.

The first full deployment of the RS took place in June 2014. A single system, the schematic of which is given in [59], took data for approximately 5 months, after which a second system was added in October of 2014. A photo of the remote station in this second configuration is given in Figure 3.1. These systems took data until September 2015, minus some down-time for repairs and upgrades which happened periodically throughout the deployment interval.

Figure 3.1: The remote stations in the 2-station configuration during their second deployment on Long Ridge, Millard County, UT, USA.

These implementations of the RS were plagued by one critical issue that severely compromised the data taken during this interval. A faulty piece of hardware in the trigger path resulted in only very high SNR events triggering the device. Based on previous theoretical and subsequent experimental limits placed on the radar cross-section of EAS, the chance of a primary event with sufficient energy to trigger the stations during this period is statistically highly unfavored.

This issue was discovered and isolated during the trip to retrieve the stations at the culmination of their initial deployment (September 2015). It was decided in the subsequent few days that rather than attempt a preliminary analysis on data that was likely devoid of events, an attempt at a re-design and re-deployment would be a better use of resources. As the diagnosed problem, which will be elucidated in this section, was a hardware issue, it was decided that the entire hardware-based trigger should be migrated to firmware. This led to a drastic reduction in systematic error within the trigger, as well as remote control over formerly hardware trigger parameters. Most significantly, it led to an order of magnitude improvement in SNR sensitivity.

The remainder of this chapter is dedicated to an upgrade to the RS systems. This upgrade was

made in late 2015 and the stations were re-deployed from February-April 2016. After this, a noise reduction technique, described below, was implemented, and the stations were further deployed for the Autumn of 2017 at the University of Kansas Field Station.

3.2 Trigger

3.2.1 Theory

The cold plasma produced by an EAS as it traverses the atmosphere is effectively stationary in 3-space, with ionization electrons having O(1-10 eV) energies. The plasma is not, however, stationary in 4-space, since the plasma lifetime in the troposphere and lower stratosphere is O(10 ns) [67]. Therefore, the moving shower front precedes a short-lived stationary plasma with an evolving number density. This unique physical phenomenon results in a scattered signal with a very unique signature; the phase relationships between different reflections from different parts of the shower combine coherently to result in a frequency-shifted return signal.This was exploited in the first iteration of the TARA Remote Stations (RS), and is further exploited in the trigger described herein.

"Heterodyning" is the extraction of a modulation from a sinusoidal signal by mixing it with a second sinusoid, using the simple identity $2cos\theta cos\phi = cos(\theta - \phi) + cos(\theta + \phi)$. For FM radio, $\theta = (\omega_0 + \omega_{mod})t$, where ω_0 is a carrier frequency and ω_{mod} is some audio-frequency modulation. Using $\phi = \omega_{lo}t$, where $\omega_{lo} = \omega_0$ is the local oscillator in a radio receiver, results in two heterodyne frequencies: the difference term (leaving only the modulation), and the sum term, which is up-shifted and easily filtered. The phase of a linear frequency-shifting signal may be written $\theta = \omega t + \kappa t^2$, where ω is the angular frequency and κ is the rate of change of the frequency in units of s^{-2}. Setting ϕ to a time-delayed copy of θ with delay δt, the resultant difference heterodyne is a monotone frequency $f_m = 2|\kappa|\delta t$. This is shown diagrammatically in Figure 3.2.

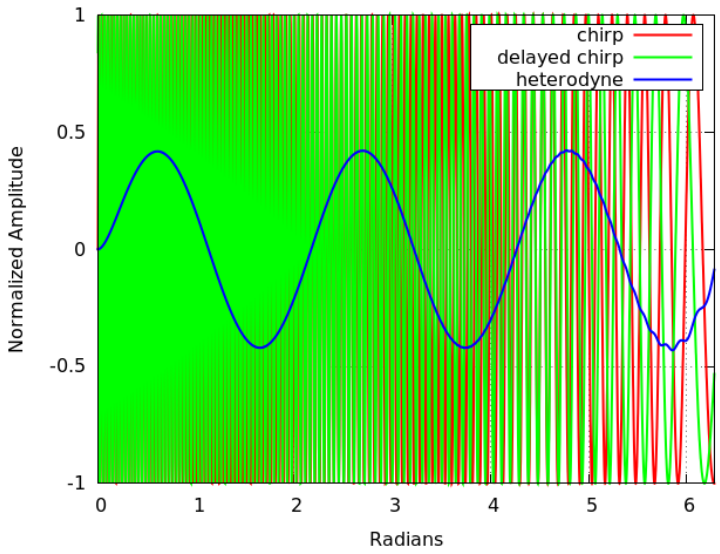

Figure 3.2: An example of the heterodyne method. A chirp with a starting angular frequency of 200 Hz and a chirp rate $\kappa = 15 Hz/s$ is mixed with a copy of itself, delayed by $\delta t = .1s$. The resultant monotone, f_m is 3 Hz.

For an EAS we expect κ of 1-3 MHz/μs. Therefore, with a δt of order 100 ns, we expect monotones in the hundreds of kilohertz range. Post-mixing, we can envelope-detect the heterodyne output from the input linear chirp, and then trigger on these monotones.

In the first revision of the RS [65], the delay was provided by a long cable, and the mixing and envelope detection was analog. This analog approach has been fully migrated to firmware to allow for a more robust trigger with greater versatility.

3.2.2 Firmware implementation

3.2.2.1 Overview

The heterodyne-output trigger is now a series of modules on a Xilinx Spartan-6 FPGA [96], written in VHDL. A block diagram of the signal chain is given in Figure 3.3. An Analog Devices AD9634 analog-to-digital converter (ADC) clocked at 250 MS/s digitizes our incoming signal with 12-bit resolution. This signal is then split, with one half routed into a 16,384 word first-in, first-out (FIFO) buffer, and the other half routed to the trigger path. The read/write FIFO is written to disk when a trigger is registered.

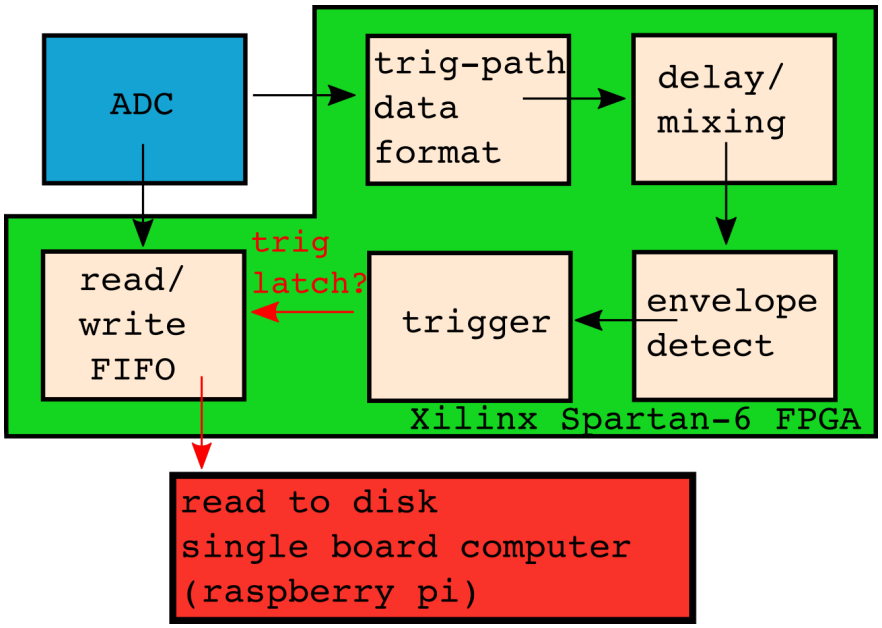

Figure 3.3: Block diagram of the RS trigger path. Upon satisfaction of trigger logic, the write-data FIFO is read out and written to disk.

The trigger path begins with a formatting module that takes the incoming ADC and formats it into a string of signed 12 bit words. This formatted data is then sent to a 32 bit FIFO which serves as our mixer. We set a read point (25 samples x .4 ns per sample = 100 ns) into this FIFO as our delayed signal. The mixer outputs a normalized, sample-by-sample product of the two input sample streams, direct and delayed. This product is then sent to the envelope-detection module, primarily a single-pole, infinite-impulse-response (IIR) low-pass filter. This filter configuration was selected for its rapid response time. Finally, the envelope is sent to a 3-part trigger module. Details of the individual portions of the trigger path are given below, and a plot of Xilinx Chipscope on-chip traces is shown in Figure 3.4, with the various signals labeled.

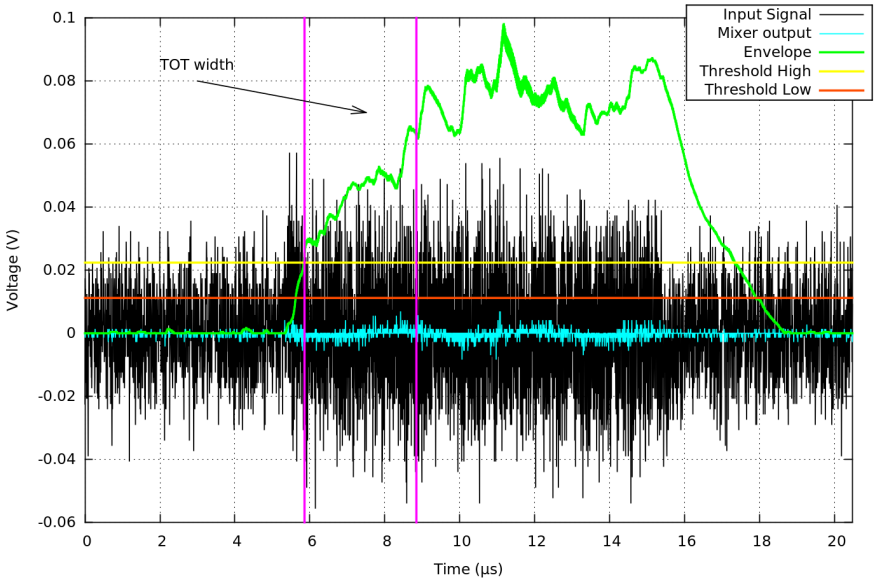

Figure 3.4: An example trigger, showing CHIPSCOPE on-chip signals. A low SNR linear chirp is embedded within noise and sent through the trigger path, resulting in the very high SNR output trace (green). Such a chirp corresponds to, in one theoretical framework (see section 3.3.4), a 10^{19}eV primary proton with a 1 MW effective radiated power TX at 20 km from the receiver, traveling orthogonally to the TX-RX baseline.

3.2.2.2 Formatting

The data from the ADC has 12 bit resolution, sent to the FPGA as the 6 central bits of two consecutive 8-bit words. Though the raw data is stored this way in the write-buffer FIFO for continuity, it is an inconvenient format for mathematical operations. Therefore the formatting module strips the MSB and LSB from each word and concatenates the two consecutive words that make up 1 sample. These are then passed as signed 12-bit vectors through the remainder of the trigger path.

3.2.2.3 Mixer

The mixer module is a simple dual-port RAM FIFO implemented with the Xilinx CORE generator, with a write depth of 30 samples. This allows us to change the delay between direct and delayed signals in the heterodyne as needed. The frequency of the heterodyne monotone is proportional to the delay time, by $f_m = 2|\kappa|\delta_t = 2|\kappa|nT$, where n is the number of delay samples and T is the sampling period. Each input sample is mixed with the delayed sample specified by the read point,

which provides the heterodyne data. The output is normalized to prevent overflow further down the trigger path.

3.2.2.4 Filtering: Envelope detection

The mixer output is then sent to the envelope-detector module. In hardware, a simple envelope detector is a rectifier and resistor in series followed by a capacitor to ground. In firmware, we can square the input values and then low-pass filter them. We chose a custom single-pole IIR because the calculation only delays the input by 2 samples, as opposed to a finite-impulse-response filter, which typically need hundreds of samples to achieve similar filtering capabilities [97]. The simple differential equation governing the low-pass filter described above, with associated resistor and capacitor values R and C is

$$\frac{v_i - v_o}{R} = C\frac{dv_o}{dt}, \tag{3.1}$$

where subscripts designate the input and output voltages, and the difference is the voltage drop across the resistor. With the assistance of Laplace transforms, this can be translated into a time-domain transfer function $H(t) = x(t)/y(t)$, where x, y are the input and output circuit voltages as a function of time,

$$H(t) = \omega_{rc} e^{-\omega_{rc} t}, \tag{3.2}$$

where $\omega_{rc} = 1/RC$. We can then discretize this signal for our digital application using a discrete version of the Laplace transform, and with the substitution $y(t) \rightarrow y[n]$ arrive at an expression that can be translated into VHDL,

$$y[n] = \omega_{rc} x[n] + e^{-\omega_{rc} T} y[n-1], \tag{3.3}$$

n is the current sample and T is the sampling period. Motivation for the term "infinite-impulse response" is evident in this last expression-each filter output value is a function of both the incoming data sample $x[n]$ and the last filter output sample $y[n-1]$. Because of this recursion, the output values theoretically only ever approach zero asymptotically and hence persist at a non-zero value

infinitely (though zero values are achieved in practice due to limitations of resolution).

Though a sharper cutoff is possible with higher-order filters, each extra pole in an IIR introduces instability and delay. We found empirically that the single-pole filter offered the best mix of filtration and stability. Therefore, our module implements the above single-pole IIR, with coefficients chosen for a -3 dB point at 300 KHz. The input stream from the mixer is re-sampled at 10 MHz, squared, fed through the filter, and then a 4 sample running-average is used to smooth the output, which is then sent to the trigger module.

3.2.2.5 Trigger

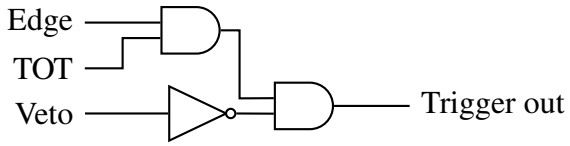

Figure 3.5: Trigger logic circuit diagram.

The 3-fold trigger logic uses the simple circuit shown in Figure 3.5. There is a threshold requirement, a time-over-threshold requirement, and a transient veto module. The threshold is a simple two-fold edge threshold. The incoming data must rise above a high threshold and then remain above a low threshold to satisfy the edge trigger logic. The TOT logic goes high once the input stream has satisfied the edge trigger logic for a specified amount of time, and thereby suppresses short-duration signals. The third parameter is a transient veto. In this module, the time derivative of the incoming envelope is monitored, and if it rises above a certain threshold, this logic goes high and vetoes the remaining trigger logic. This is an important addition to the trigger because very short, high-amplitude transients are broadband, and thus thwart both the heterodyne and the low-pass filter. In addition, since the amplitude envelope of the expected EAS reflection steadily increases as the shower progresses (the shower density increases, and the transmitter-shower-receiver baseline decreases, with shower depth) the slope of the envelope for a true signal should be very small. The three parameters-edge threshold, TOT width, and transient-veto threshold are set at runtime via commands sent to the FPGA over Serial Peripheral Interface (SPI). Examples of trigger

logic are given in Figure 3.6.

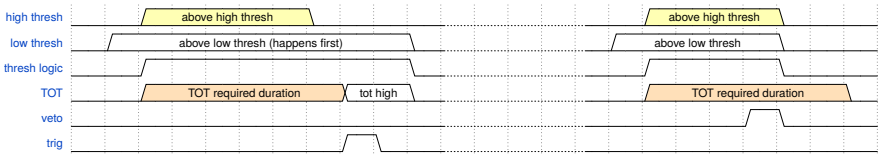

Figure 3.6: example timing diagrams of the trigger system. Left: The trigger envelope rises above low threshold then high threshold. After some amount of time, the time-over-threshold is satisfied, and the trigger goes high. the veto in this case stays low, indicating that there is not a transient present. Right: The trigger envelope rises above the low threshold and also the high threshold, but the veto goes high, which sends the threshold and time-over-threshold logic low, and so the trigger never goes high.

On negating the trigger, the veto module also communicates with the envelope module to zero the IIR filter, thereby counteracting one of the limitations of the IIR design. Due to recursion, the impulse response to high-amplitude signals requires many samples to relax to unobservable levels, so that if a sufficiently-high amplitude impulse arrives at the filter input and sends the transient veto high, the decay of the envelope could satisfy both the edge and TOT requirements even once the veto goes low, resulting in a false trigger. Therefore, when the veto goes high, it signals the envelope-detect module to zero the filter values, killing the impulse decay, and resetting the filter. Due to the simplicity of the IIR, the filtration/envelope detection recovers in 2 samples after this veto, resulting in a minimum of efficiency loss.

A plot showing the function of the transient veto module is given in Figure 3.7. High amplitude transients, which would trip a simple edge trigger, are killed by the veto so that they cannot satisfy the TOT requirement.

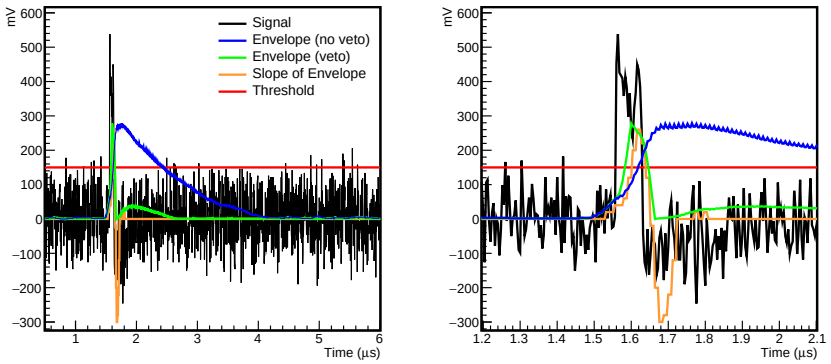

Figure 3.7: Operation of the trigger veto system. Due to the broadband nature of transients, high-amplitude spikes will trip the envelope detector, which rises above the threshold and satisfies the TOT width (blue online). With the trigger veto, which monitors the slope of the envelope rise, the envelope is truncated before the TOT can be satisfied (green online). Right panel is a zoom of the left.

If a trigger is registered, the read/write FIFO is then latched and written to disk, which in this case is the on-board flash memory of a Raspberry Pi single board computer (SBC). The SBC communicates with the FPGA via SPI, controlled using the open source WiringPi SPI library for C.

3.3 Performance

A first deployment of this system, without the transient veto and sampling at 200 MS/s, was part of the TARA experiment from Feb-April 2016. As of this writing, a re-deployment of the full system with veto, just north of Lawrence, KS at the Kansas Biological Survey KU Field Station, is underway. Instead of using a dedicated transmitter, the stations have been re-fitted to run at 250 MHz using FM radio broadcasts as the transmitted signal.

The following section represents data taken during the previous TARA deployment.

3.3.1 System Sensitivity

The trigger is sensitive to signals at low SNR. The trigger efficiency for a single chirp slope is given as a function of SNR in Figure 3.8. As evidenced by the figure, sensitivity begins below SNR of 1.

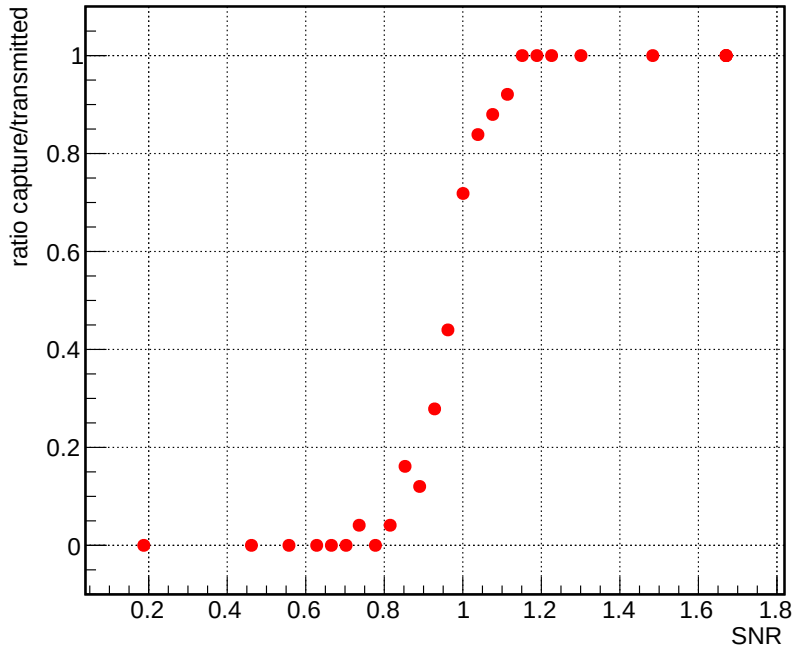

Figure 3.8: Ratio of captured pulses to transmitted pulses as a function of the SNR of the input chirp, for a chirp slope of -1.5 MHz/μs. The trigger turns on at SNR < 1.

3.3.1.1 In-Field Calibration

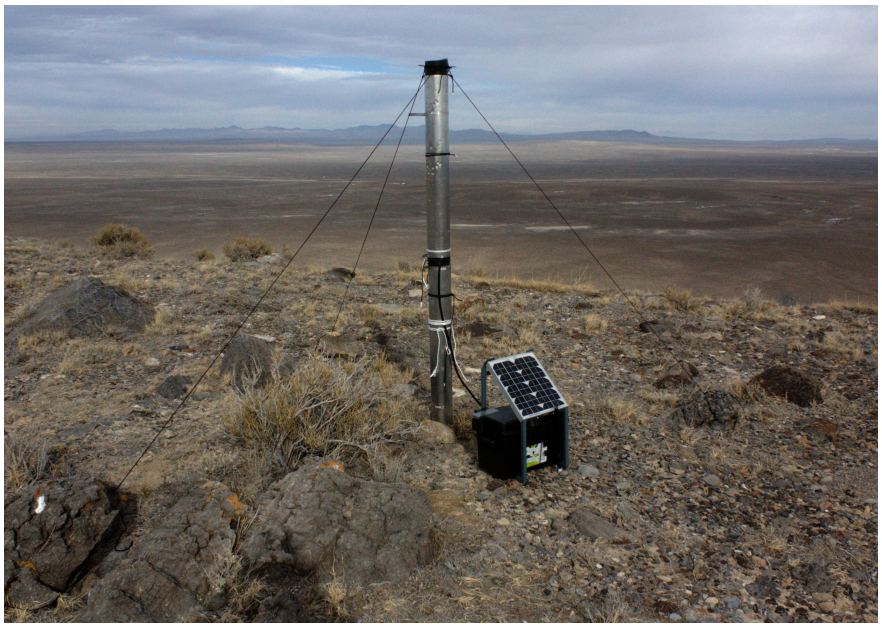

Figure 3.9: The chirp calibration unit deployed on Long Ridge, UT.

Deployed along with the RS was a system called the Chirp Calibration Unit (CCU), shown in Figure 3.9, which output a periodic chirp signal to calibrate the RS systems. The CCU is a custom board featuring a voltage controlled oscillator (VCO) governed by an ATMEL ATMEGA328 microcontroller, designed and built at the Instrumentation Design laboratory at KU. The chirp slope and duration of the VCO are set in the microcontroller firmware. The output of this board is attenuated to the desired amplitude and coupled to a custom 'fat' dipole, with a resonance at 70MHz and a sub-3 VSWR bandwidth of $\pm$20 MHz for full coverage of our expected signal region. An in-field CCU chirp captured simultaneously in RS1 and RS2 is given in Figure 3.10, showing that the full system, as deployed, is sensitive to chirps at SNR $\sim$1.

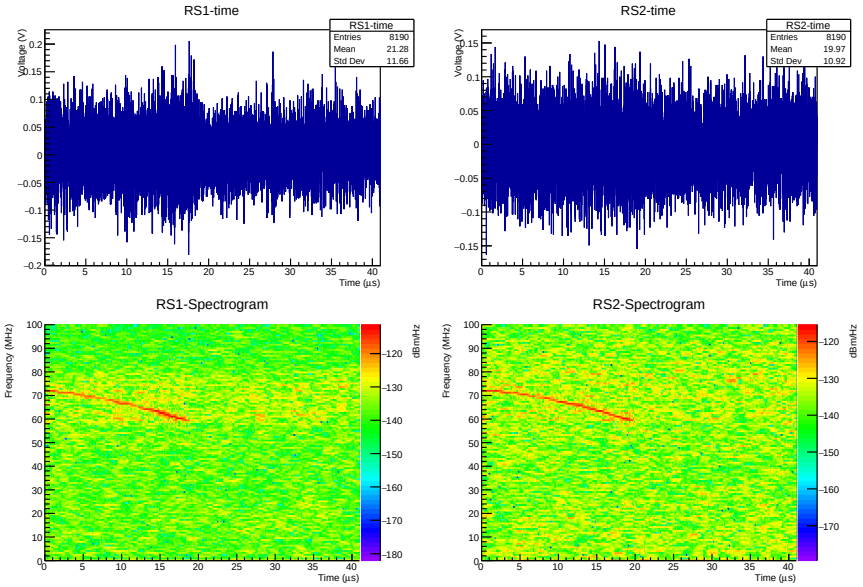

Figure 3.10: An example CCU pulse captured coincidently in RS1 and RS2 during deployment on Long Ridge, UT.

3.3.1.2 Galactic background

Another important metric is the measurement of the ambient background temperature. In principle, the ultimate noise floor to which a small-signal RF experiment should be sensitive to is the CMB. However, local galactic sources make it impossible to achieve this noise floor, as they contribute to the background temperature. One way to monitor the sensitivity of the system to galactic backgrounds is to take forced trigger snapshots periodically, and monitor the change in ambient background. For the deployment of RS rev. 2, these snapshots were taken at 6 minute intervals. Figure 3.11 shows a clear diurnal variation that correlates poorly with the solar altitude, but quite well with the altitude and azimuth of the galactic center with respect to the boresight pointing of the RS antenna. Such a study is essential to verifying that we are sensitive to the lowest possible signal levels, and not simply amplifying our own system noise.

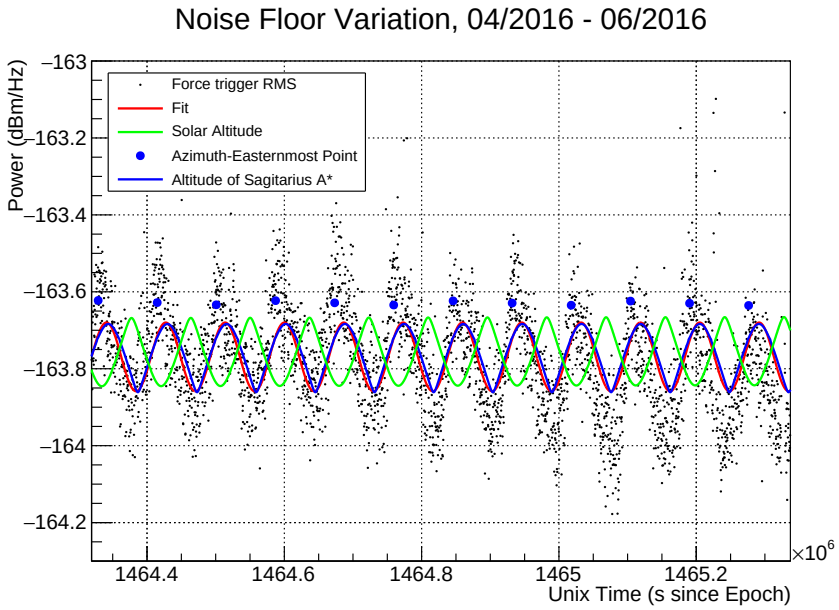

Figure 3.11: RMS power of forced triggers for April-June of 2016, zoomed in to a 12 day region. A sine-wave fit to the data matches very well with the altitude of the galactic center with respect to the boresight pointing of the antenna. Variation due to the solar altitude (green) is in poor agreement with the fit, suggesting true sensitivity to the galactic background.

3.3.2 Pointing

The RS employ a timing system that affords O(10) ns timing resolution per station. An iLotus M12M GPS chip provides a 100 pulse-per-second (PPS) line which is read by the FPGA, controlling 2 counters. A slow counter simply counts the number of 100PPS pulses since the top of the GPS second, which is indicated by a wider than usual pulse. A fast counter counts the number of system clock cycles between successive 100PPS pulses. These two counts are latched when a trigger is registered, and are written with the ADC data.

This high-resolution timing allows for the two stations to 'point' at the sources of signals. Naturally two stations cannot isolate a point in 3 space, but the knowledge that most anthropogenic backgrounds are restricted to the ground plane effectively allows us to use pointing to isolate noise sources. Figure 3.12 shows the maximum cross-correlation value of coincident events captured by RS1 and RS2 as a function of the time difference of the trigger timestamps (RS1-RS2). The trigger point slewing inherent to time domain threshold triggers has been corrected for algorithmically.

Figure 3.12 clearly shows noise sources, as well as the CCU in 2 different amplitude configurations, as hot spots in the plot. Events which do not obviously cluster with others, are in the largely forward region (small Δt), and which have a high cross-correlation value will be the events of interest in the final analysis.

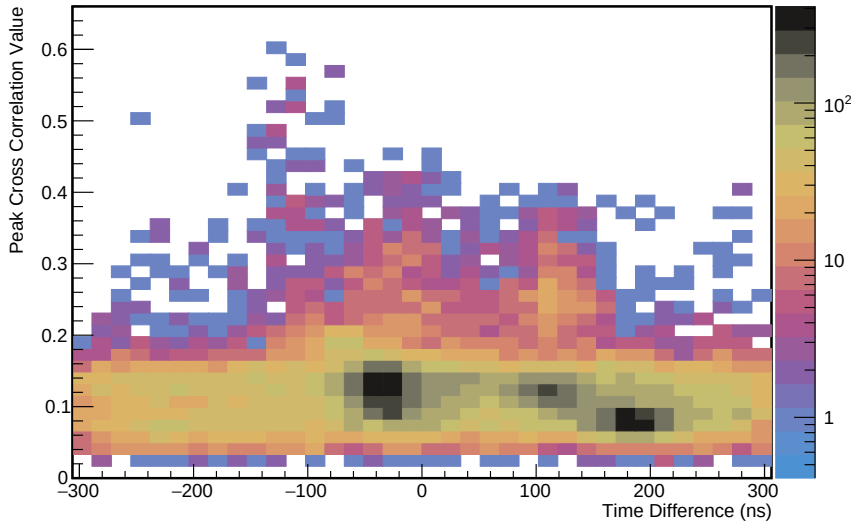

Figure 3.12: maximum cross-correlation value of coincident events between RS1 and RS2, as a function of the difference between the trigger timestamps. The causal window for events is $\pm$200 ns, since the stations were placed roughly 70 meters apart. Events out near $\pm$200 ns are aligned along the axis connecting the two antennae, while events near 0, which arrive at the antennas simultaneously, come from sources equidistant to both stations. The bright spots at 0 ns and cross-correlation values of .25-.4 are the CCU for varying levels of SNR. Bright hot spots at low cross correlation values correspond to man-made structures in the vicinity.

3.3.3 Durability

As stated, the stations were deployed in the Utah desert from February through December of 2016, though they only took active data through August. The TARA transmitter ran from Feb-May, and after that the RS only took forced-trigger data, from which the above galactic background plots were made. This means that the stations ran in sub-zero freezing conditions during winter, and also through average summer temperatures of 35 C. The CCU, as well as both stations, returned after this deployment in perfect working order.

3.3.4 Feasibility

The initial analysis from the TARA experiment reported no signal. An analysis of the data from the initial RS run is ongoing. Several theory papers [98, 76] have subsequently made different predictions for the expected return signal, predicting much smaller amplitudes than those for which TARA was designed. These papers include the effects of collisions within the plasma itself, as well as a modified treatment of the plasma lifetime in the atmosphere, primarily resulting from interactions with, and possible attachment to molecular nitrogen and oxygen, both of which are still open questions for detection of reflected RF from air-shower plasmas.

If the most conservative of the macroscopic models is correct, then the relative received power for a bi-static setup at a TX-shower-RX path length of approximately 20 km is -260 dB, for a 10^{18} eV primary proton interacting in air. For an average -164 dBm galactic background temperature (taken as the noise floor in our simulations), at least 94 dBm (2.5 MW) of transmitted power is required for a signal with SNR$\geq$1. TARA fell short of this number by 3 orders of magnitude, which is consistent with the lack of signal reported. One way to overcome this large transmitter power requirement is to re-design the system to parasitically exploit ambient FM as the transmitted signal. The combined output power of the FM broadcasts in any major metropolitan area is likely to exceed this power requirement, and the inherent isotropy of FM broadcasts translates into an potentially enormous effective target volume, thus raising the statistics on higher energy UHECR.

A feasibility study of this concept ran at the KU Field Station from September to November of 2017. In this scheme, the RS are running parasitically off of the FM broadcasts in the Kansas City metropolitan area. The major FM broadcasts in the greater Kansas City metro area sum to $>$2.5 MW. In the conservative case outlined above, we would then be sensitive to showers with primary energies of 10^{18} eV at distances of 20 km from the point of maximum TX output power. Our system is set up roughly 40 km from the center of Kansas City, but the metro area (including Olathe, Lawrence, and Overland Park) extends to within 5 km of the receiver, meaning that there is considerable TX power in the air surrounding the RS. Indeed, our receiving antennas are pointed in the direction of greatest power, due East, to Kansas City. Our very large detection volume in this

FM scheme, with a footprint area of roughly 6000 km^2, will be traversed by 60 UHECR per year with energies of 10^{20} eV. During our 2 month run, this will subject our instrument to approximately 10 events at this very high energy. Detection of these 10 events may be possible depending upon trigger efficiency and the on-site noise condition (which is always subject to change).

Chapter 4

Particle-level model for radar based detection of high energy neutrino cascades

This chapter is adapted from a paper accepted by Nuclear Instrumentation and Methods in Physics-A.

Particle-level model for radar based detection of high energy neutrino cascades

S.Prohira[1], D.Besson [1,2]

[1] University of Kansas, Lawrence, KS, USA

[2] National Research Nuclear University, Moscow Engineering Physics Institute, 31 Kashirskoye Highway, 115409, Russia

4.1 Part One: Particle-level model; RadioScatter; lab tests

4.1.1 Introduction

High-energy particles incident on dense media will produce a shower of secondary particles. As these shower particles traverse the interaction medium, they eject cold ionization electrons from atoms in the bulk, forming a tenuous particle-shower plasma (PSP), distinct from the energetic shower front particles responsible for ionization. For high incident particle energies ($E \geq 1$ PeV, consistent with, and beyond, the experimental reach of the IceCube[19] experiment), this plasma will become dense enough to reflect incident radio-frequency (RF) radiation[58]. It has been recently suggested[61][62][89][90] that this technique could be used to advantage in the field of high-energy neutrino physics, where low fluxes and small interaction cross-sections demand large detection volumes. In the radio scatter approach, a large volume of interaction medium, such as ice, is illuminated with radio-frequency (RF) energy by a transmitter (TX), and any PSP of sufficient density within this volume will reflect the incident RF to a distant receiver (RX). Several experimental tests have been made to detect this phenomenon[78][64], but none have approached the incident particle energies, and therefore densities, of a true high-energy neutrino/ice interaction. It is this scenario that we discuss here.

There are several advantages of the radio scatter method over the current RF-based detectors for high-energy neutrinos, including ARA[49], ARIANNA[50] and ANITA[51]. Those experiments seek to detect primary "Askaryan"[44] emissions from the showers themselves. "Askaryan radiation" [47][55] denotes collective Cherenkov radiation, confined to a cone of angular thickness $\sim$1 degree, beamed at the usual Cherenkov angle. Detection of such emission is therefore constrained to the limited solid angle of the cone, significantly limiting the geometric aperture. The radio scatter method does not suffer from this geometric limitation, and has acceptance over a much larger portion of the solid angle surrounding a high-energy neutrino shower axis. Additionally, whereas Askaryan signals are directly proportional to the energy of the primary neutrino, the radio scatter signal scales with both the neutrino energy as well as the output power of the sounding

transmitter, such that a strong transmitter can effectively lower the neutrino energy threshold. The impulsive signal shape of Askaryan emission is also easily mimicked by anthropogenic transients, particularly at the South Polar ARA site which is in close proximity to the Amundsen-Scott South Pole station, making background rejection challenging. The return signal from the radio scatter method would be a characteristic, coherent, $\mathcal{O}$(10 ns) burst of RF with frequency content set by the transmitter-shower-receiver geometry, permitting a well-tailored firmware trigger.

The PSP itself is a unique physical system. The cold ionization electrons are quasi-stationary, with energies of $\mathcal{O}$(10 eV) and an electron number density n_e decreasing longitudinally at a rate set by the ionization electron lifetime, while the shower front which produces them advances at $\beta \sim 1$. The lifetime of the PSP electrons (called the plasma lifetime τ) is medium-specific, and has not been experimentally verified. The best existing measurement of the ionization lifetime in ice is given in [88], and is $\mathcal{O}$(1-10 ns), with the lifetime dependent on the temperature and purity of the ice. Note that τ refers to the average time required for individual free PSP electrons to be captured by positive ions in the medium, in contrast to the much-longer lifetime of the shower itself. For our proposed in-ice experiment, the lifetime of the plasma electrons is not well-established; nevertheless, (as detailed below) our simulations indicate detectable, coherent radar returns for PSP lifetimes as short as 0.1 ns. Laterally, 90% of the shower particles are contained within 1 Molière radius from the shower axis, which for ice is order 10 cm.

Direct radio (Askaryan) emission from acceleration of the shower particles themselves is currently neglected in the RadioScatter module. This is due to the fact that it will be largely beamed within a few degrees of the Cherenkov angle, and therefore only comprises a small percentage of the detectable solid angle. Reflections from the relativistically moving shower particles are also neglected, as these predominantly manifest at frequencies beyond the range of our planned data acquisition system (DAQ), and are several orders of magnitude lower in number than the ionization electrons.

Several macroscopic models for radio scattering, treating the PSP monolithically, have been presented elsewhere[61][89][90][76][98]. Although computationally economical, such models re-

quire assumptions regarding the development and characteristics of the plasma. Here, we calculate the reflected radar signal from the PSP microscopically, by summing over the individual scatterers in showers produced by Monte-Carlo simulations such as GEANT4[99], accounting for charge motion in a plasma using the single-particle equation of motion (EOM). Particular attention is given to characterization of the time-domain signal, which is essential in developing experimental trigger techniques. In what follows we will describe the particle-level model, and how it has been incorporated into the RadioScatter software package to simulate RF scattering from PSP.

4.1.2 Particle-level PSP model

4.1.2.1 Derivation of the individual particle radiative contribution

Our goal is to calculate the reflected radio-frequency signal due to the PSP, which requires, primarily, determining the individual particle equation of motion, and the properties of electric field wave propagation within the medium.

Our calculation starts from the classical equation of motion for an electron with label A, under the influence of an incident plane wave from a source at a distance R_A, and subject to collisions with frequency ν_c,

$$m\left(\ddot{\mathbf{x}}_A + \dot{\mathbf{x}}_A \nu_c\right) = -q\mathbf{E_0}, \tag{4.1}$$

with

$$\mathbf{E_0} = E_0 e^{i(\mathbf{k}\cdot\mathbf{R_A} - \omega t)} \hat{\boldsymbol{\varepsilon}}_A. \tag{4.2}$$

The symbol q is the electric charge. ω is the angular frequency of the source field. The unit vector $\hat{\boldsymbol{\varepsilon}}_A$ is the polarization vector of the source field as evaluated at the charge A, and $\mathbf{k}$ is the wave vector of the source electric field, and is complex. It will play an important role in calculations of the scattered field in what follows. A diagram of the angles is given in Figure 4.1.

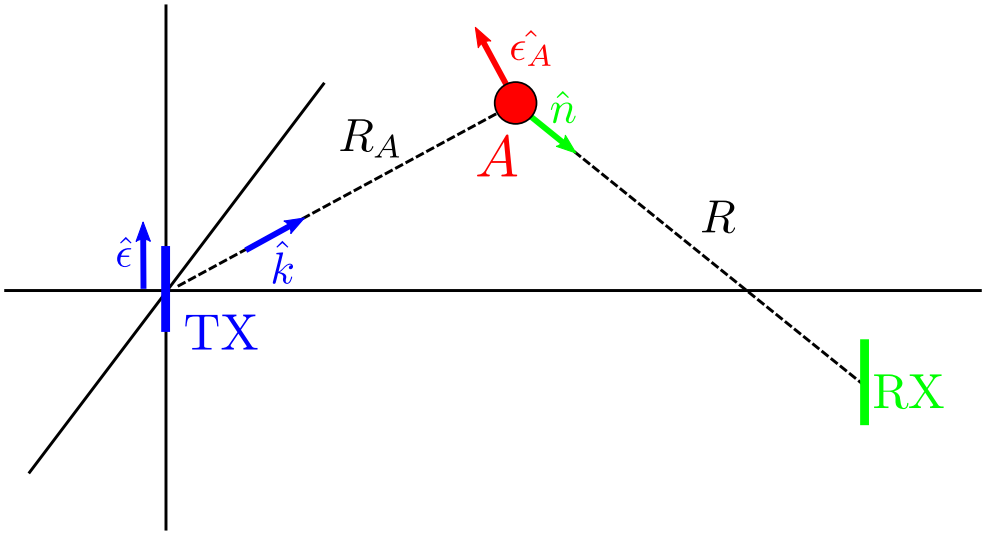

Figure 4.1: The angles used in the derivation of the individual particle scattering contribution presented in the text. The direction of the wave vector $\hat{k}$ points from transmitter (TX) to the charge A. $\hat{n}$ points from the charge A to the receiver (RX). The polarization of the source is labeled $\hat{\varepsilon}$, and the polarization of field at charge A is $\hat{\varepsilon_A}$, which is perpendicular to $\hat{k}$ and lies in plane with $\hat{\varepsilon}$.

The collisional term ν_c is expressed as a sum over the species in the plasma, as in [67].

$$\nu_c = \sum_s n_s \bar{v_e} \sigma_s; \tag{4.3}$$

here, n_s and σ_s are the number density and collisional cross-section, respectively, of species s, and $\overline{v_e}$ is the mean thermal velocity of the PSP electrons. (More discussion of collisions will follow in a later section.) Solving for the acceleration of the charge in Eq. 4.1 gives

$$\ddot{\mathbf{x}}_A = -\frac{q\omega E_0 e^{i(\mathbf{k}\cdot\mathbf{R_A}-\omega t)}}{m(\omega + i\nu_c)}\hat{\varepsilon_A}. \tag{4.4}$$

For charges with negligible velocity, such as the ions and ionization electrons in the PSP cloud,

the electric field from a charge A takes the form

$$\mathbf{E_A} = \frac{q}{R^2}\hat{n} + \frac{q}{c^2}\left[\frac{\hat{n}\times(\hat{n}\times\ddot{\mathbf{x}}_A)}{R}\right]_{ret}, \tag{4.5}$$

where the evaluation of the acceleration field takes place at the retarded time, $t' = t - |\mathbf{R}|/c$ with t the time at some distant receiver, and the unit vector $\hat{n}$ points from the charge to the receiving antenna. In the plasma approximation, the first term in Eq. 4.5 cancels due to equal and opposite contributions from electrons and ions. However the second term is only nonzero for the free electrons, as the ions in a dense medium are fixed. So the problem reduces to calculating only the acceleration field of the free ionization electrons.

The far-field Larmor equation for the electric field of the charge A, under an incident field $\mathbf{E_0}$ and including the effects of collisions as above, is then

$$\mathbf{E_A} = -\frac{q^2\omega}{c^2 m(\omega + i\nu_c)}\left[\frac{\hat{n}\times(\hat{n}\times\mathbf{E_I})}{R}\right], \tag{4.6}$$

where

$$\mathbf{E_I} = \frac{V_0}{R_A}\hat{\boldsymbol{\varepsilon}}_\mathbf{A} = \frac{V_0 e^{i(kR_A-\omega t_A)}}{R_A}\hat{\boldsymbol{\varepsilon}}_\mathbf{A}, \tag{4.7}$$

which is simply the incident field $\mathbf{E_0}$ at the point A. The quantity $V_0 = E_0 \times 1m$ is the source field evaluated 1 meter from the transmitting antenna, with units of Volts. For simplicity, it is assumed that the source $\mathbf{E_0}$ is plane polarized, and the wave vector $\mathbf{k}$ lies along the vector $\mathbf{R_A}$. The charge acceleration vector $\hat{\boldsymbol{\varepsilon}}_\mathbf{A}$, which is the polarization vector of the source at A, forms a plane with the polarization vector of the source, perpendicular to $\mathbf{R_A}$. The quantity R (without subscript) is the magnitude of the vector between the charge A and the receiver (Figure 4.1).

When dealing with the propagation of waves in a dense medium, the properties of the medium itself must be considered. For a general treatment of the radar problem, there are three propagation

regions for RF wave numbers k: free-space, in-medium, and in-plasma, which we denote as

$$k_0 = \mathrm{k}_0, \tag{4.8}$$

$$k_m = \mathrm{k}_m - i\xi(\omega), \quad \text{and} \tag{4.9}$$

$$k_p = \mathrm{k}_p - i\beta, \tag{4.10}$$

respectively. The non-italicized k represents the real part of k, $\xi(\omega)$ is the frequency-dependent attenuation coefficient of the medium, and β is the attenuation coefficient of the plasma due to collisions (discussed below). For the medium, $\xi(\omega)$ is the inverse of the attenuation length, a quantity representing the length over which a field amplitude is reduced by a factor of e [100]. For the ionization electrons in a plasma subject to the equation of motion of Eq. 4.1, the complex wave number k_p is [101],

$$k_p = \frac{\omega}{c}\mathrm{n}_p = \frac{\omega}{c}\left[1 - \frac{4\pi n_e q^2}{m}\left(\frac{1}{\omega^2 + i\omega\nu_c}\right)\right]^{\frac{1}{2}} \tag{4.11}$$

$$\approx \frac{\omega}{c}\left[1 - \frac{4\pi n_e q^2}{2m}\left(\frac{1}{\omega^2 + i\omega\nu_c}\right)\right] \tag{4.12}$$

$$\approx \frac{\omega}{c}\left[1 - \frac{\omega_p^2}{2}\left(\frac{1}{\omega^2 + i\omega\nu_c}\right)\right], \tag{4.13}$$

where we have used the binomial approximation for the index of refraction n_p, and have introduced the plasma frequency, $\omega_p = \sqrt{4\pi n_e q^2/m}$, where n_e is the electron number density in units of cm^{-3}. This number density is the local number density at the charge A. The imaginary part of this expression represents a damping of wave propagation in the plasma due to collisions,

$$\beta = \mathrm{Im}[k_p] \approx \frac{\omega_p^2}{2c}\left(\frac{\nu_c}{\omega^2+\nu_c^2}\right). \tag{4.14}$$

Continuing with our general assumption that a transmitter may be in free space interrogating a plasma within a dense medium, we must expand the quantity kR_A as a sum over the different regions and their associated wave vectors, shown visually in Figure 4.2.

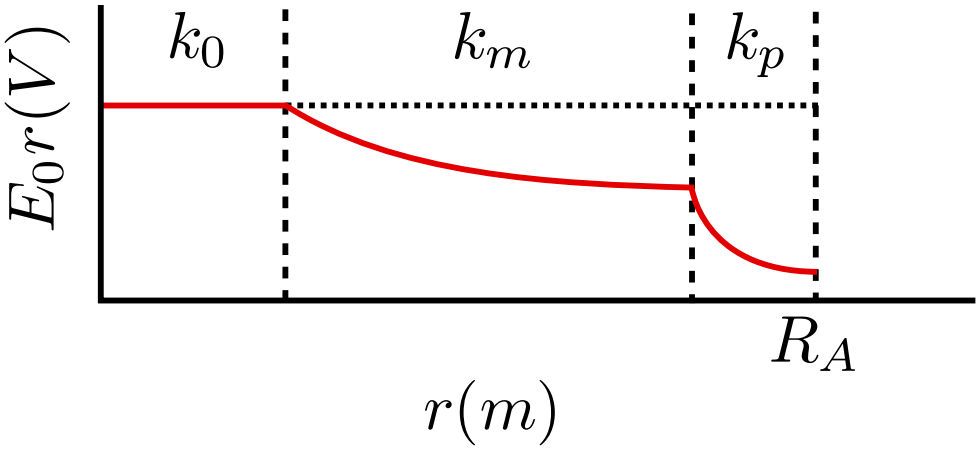

Figure 4.2: Cartoon representing the amplitude of a wave (solid line) as it propagates through mediums with different n and k.

The general distance between TX and the charge A, R_A, is broken down into the same three regions as for k above. The distances traveled in free space, the medium, and the plasma, are R_0, R_m, and R_p respectively, such that $R_A = R_0 + R_m + R_p$. We then expand the incident field $\mathbf{E_I}$ using these regions.

$$\mathbf{E_I} = \frac{V_0}{R_A}\exp\left[i(kR_A - \omega t)\right]\hat{\boldsymbol{\varepsilon}}_\mathbf{A} \tag{4.15}$$

$$= \frac{V_0}{R_A}\exp\left[i(k_0R_0 + k_mR_m + k_pR_p - \omega t)\right]\hat{\boldsymbol{\varepsilon}}_\mathbf{A} \tag{4.16}$$

$$= \frac{V_0}{R_A}\exp\left[i(\mathrm{k}_0R_0 + \mathrm{k}_mR_m + \mathrm{k}_pR_p - \omega t)\right]e^{-\xi R_m}e^{-\beta R_p}\hat{\boldsymbol{\varepsilon}}_\mathbf{A} \tag{4.17}$$

Because $k_p = k_p(\omega_p)$, $\omega_p = \omega_p(n_e)$, and $n_e = n_e(R_p)$, the product of the wave vector (real and imaginary) with the plasma path length R_p is in fact an integral over the distance R_p. For example, the damping term from the imaginary part of the wave vector, β, becomes

$$\exp\left[-\beta R_p\right] \rightarrow \exp\left[-\int_0^{R_p} \beta(r)dr\right], \tag{4.18}$$

which accounts for the variation in k_p as it traverses the plasma.[I]

Altogether, we now have an expression for the scattered field from an individual electron in the PSP cloud,

$$\mathbf{E_A} = \frac{\alpha E_I}{R}\hat{n} \times \hat{n} \times \hat{\varepsilon_\mathbf{A}} \tag{4.19}$$

where

$$\alpha = -\frac{q^2\omega}{c^2 m(\omega + i\nu_c)} \tag{4.20}$$

is complex with units of length. When the imaginary part of α goes to zero, that is, when $\nu_c = 0$ and there are no collisions, α is the familiar 'classical electron radius', and the collisional damping term β goes to zero. In this case,

$$k_p = \frac{1}{c}\sqrt{\omega^2 - \omega_p^2}, \tag{4.21}$$

which is the standard dispersion relation for electric fields in a collisionless plasma.

[I]This integration is currently neglected in the RadioScatter module, due to the computational expense involved. However, at the energies/densities/frequencies of interest to this problem (10^8-10^9Hz, 10^{15}-10^{21}eV) the single-value approximation is acceptable. For example, at 500 MHz and 100 PeV, the difference in attenuation of an incident wave between the single-value and integral method is $<$10%, with the single-value method being the more conservative, in terms of the strength of the signal returned. A future release will include the effects of this integration.

4.1.3 Applicability

The parameters α and β must be experimentally verified, as ν_c is not known for the case of a particle shower in ice. We can however use standard plasma theory[102] and also experimental data[72] to assess the validity of the above model. This single-particle expression is applied to all particles within a shower to attain the full scattered signal. Details about the sum, which incorporates the other main unknown of the model, the plasma lifetime τ, are given in a later section. What follows in this section pertains to the sum total scattered signal from a shower.

The characteristics of scattered RF, with angular frequency ω, reflected from a plasma are determined by the magnitude of ω relative to $\omega_p = \omega_p(n_e)$. For regions of high electron number density where $\omega < \omega_p$ ("overdense" regime), the wavenumber of Eq. 4.21 (collisionless regime) is fully imaginary, and therefore that region is opaque to incident RF, e.g. these fields are fully reflected. For $\omega > \omega_p$ ("underdense"), reflection is primarily due to Thomson scattering and the plasma is increasingly transparent. For example, the very diffuse plasma in the Earth's ionosphere is traversed with minimal scattering loss by ultra-high-frequency (UHF) RF transmissions from satellites (underdense regime), whereas low-frequency waves broadcast from Earth may be totally reflected (overdense regime).

Therefore, in general, overdense scattering is coherent and underdense scattering is incoherent, and so radar sounding is described in terms of overdense scattering. The effective cross-section of the overdense region of a generic radar target can be calculated from the standard bi-static radar equation, as follows:

$$\sigma_{eff} = \frac{(4\pi)^3 R_t^2 R_r^2 P_r}{P_t G_t G_r \lambda^2}, \tag{4.22}$$

where R_t and R_r are the distances from the shower to the transmitter and receiver, respectively, P_t and G_t are the transmitted power and transmitter antenna gain, and P_r and G_r are the received power and receiver antenna gain. In the case of a particle shower, σ_{eff} is bounded by the product of the transverse scale (of order the Moliere radius, or $\mathcal{O}$(10 cm) for ice) and the longitudinal scale (set by the radiation length, or $\mathcal{O}$(10 m) for ice) of the reflecting shower. In our case, the over-

dense/underdense boundary, in addition to being frequency-dependent, is evolving both spatially, over distances of cm, and temporally, over times of order ns. The spatial dependence on interrogating frequency $f = \omega/2\pi$ is shown diagrammatically in Figure 4.3, where $\omega_p/2\pi$ is plotted versus lateral profile for a 10 PeV shower. The x-intercepts indicate the lateral extent of the overdense region for different sounding frequencies, and the Moliere radius r_M is also indicated; the greater penetration of the higher-frequency signal is evident from the Figure.

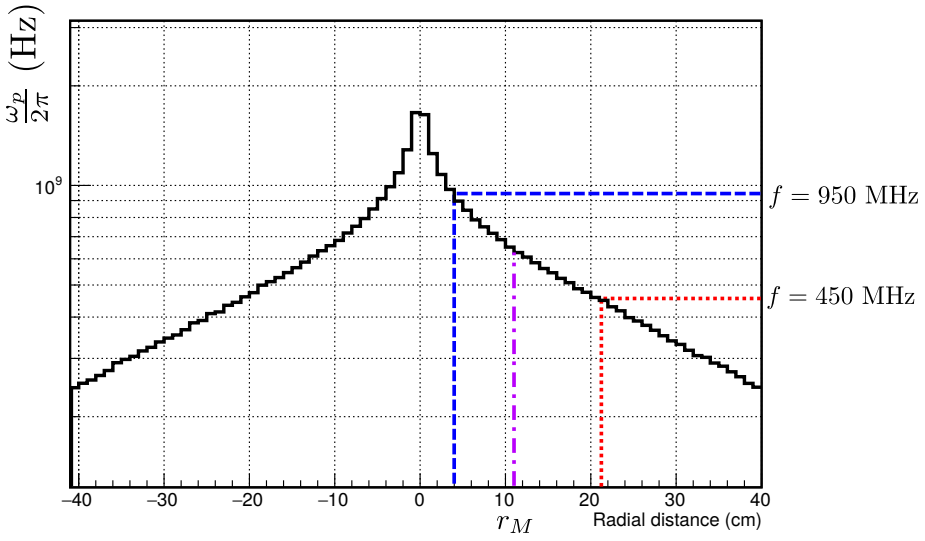

Figure 4.3: Shower plasma frequency $\omega_p/2\pi$ versus shower lateral profile for a 10 PeV shower. The effective corresponding radial extent of the overdense region is also shown for two interrogating frequencies. "r_M" denotes the Moliere radius in ice.

We can use this reasonable upper bound on σ_{eff} to assess the validity of Eq. 4.19, by plotting σ_{eff} versus primary particle energy for various interrogating frequencies. Figure 4.4 shows that σ_{eff} remains reasonable (e.g. on the order of the dimensions described above) up to high energies, across a wide range of frequencies. From a macroscopic standpoint, lower interrogating frequencies see a larger physical cross section of the shower (due to the plasma frequency) than high frequencies, but ultimately smaller σ_{eff} than high frequencies at high energies due to the λ^{-2} term in Eq. 4.22. We see this same behavior in the particle level treatment (Figure 4.4), where σ_{eff} scales with frequency once the overdense/underdense boundary is crossed ($\sim$1-10 PeV).

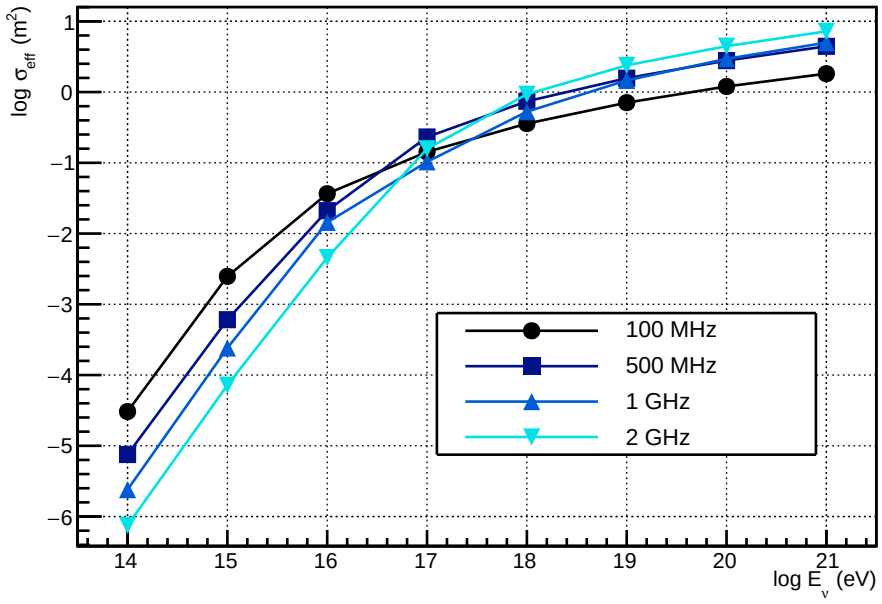

Figure 4.4: Effective scattering cross-section σ_{eff} as a function of primary energy, for a range of transmitted frequencies. The transmitter output is 1 Kw ($\sim$223 V) and the TX–RX baseline is $\sim$1 km, with showers thrown at random positions within the intervening volume. The plasma lifetime is 1 ns.

4.1.4 RadioScatter

The above model is incorporated into a software package called RadioScatter [103], which is open source and has been successfully run on several different flavors of Linux. The module is written in C++ and can be incorporated into user scripts or large Monte-Carlo packages such as GEANT4. The code, documentation, and example GEANT4 programs using RadioScatter are available at the referenced GitHub repository.

The polarization and angle conventions used in RadioScatter are presented graphically in Figure 4.5.

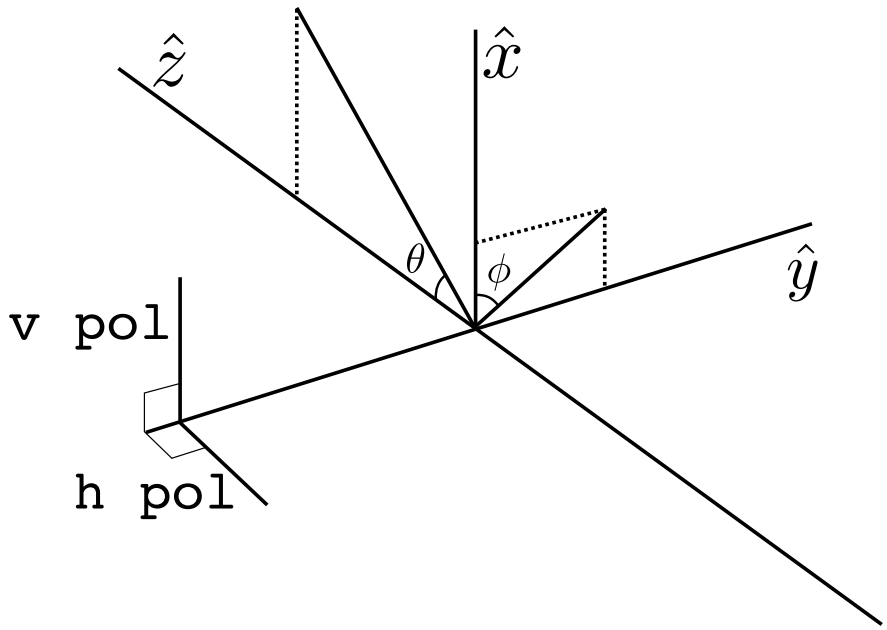

Figure 4.5: Geometry conventions used in RadioScatter, indicating what is meant by vertically (v pol) and horizontally (h pol) polarized antenna configurations used in the text and the module.

4.1.5 GEANT4 implementation

We now describe the actual implementation of RadioScatter within the GEANT4 simulation package. We describe how the PSP is generated, how number densities and collision frequencies are calculated, and the technique for calculating the scattered signal from the PSP.

4.1.5.1 Generation of the PSP

GEANT4 is the premier suite of simulation tools for particle interactions with matter. Users can specify nearly any projectile incident on nearly any target material and geometry, with access to individual four-momenta at run-time. GEANT4 provides this particle-level information to the user at each step of a shower's evolution, including the length of each step in mm (medium-density specific, and internally-defined in GEANT4) and the energy deposited in the medium over that step. GEANT4 utilizes an extensive library of materials and their properties, including radiation lengths and ionization energies. To find the number N of ionization electrons produced in each step of each shower particle, we therefore divide the amount of energy deposited in the step by the

ionization energy of the medium. In ice, for example, GEANT4 calculates an ionization energy of 69 eV. It is these ionization electrons which comprise the PSP cloud and from which we calculate the scattered signal.

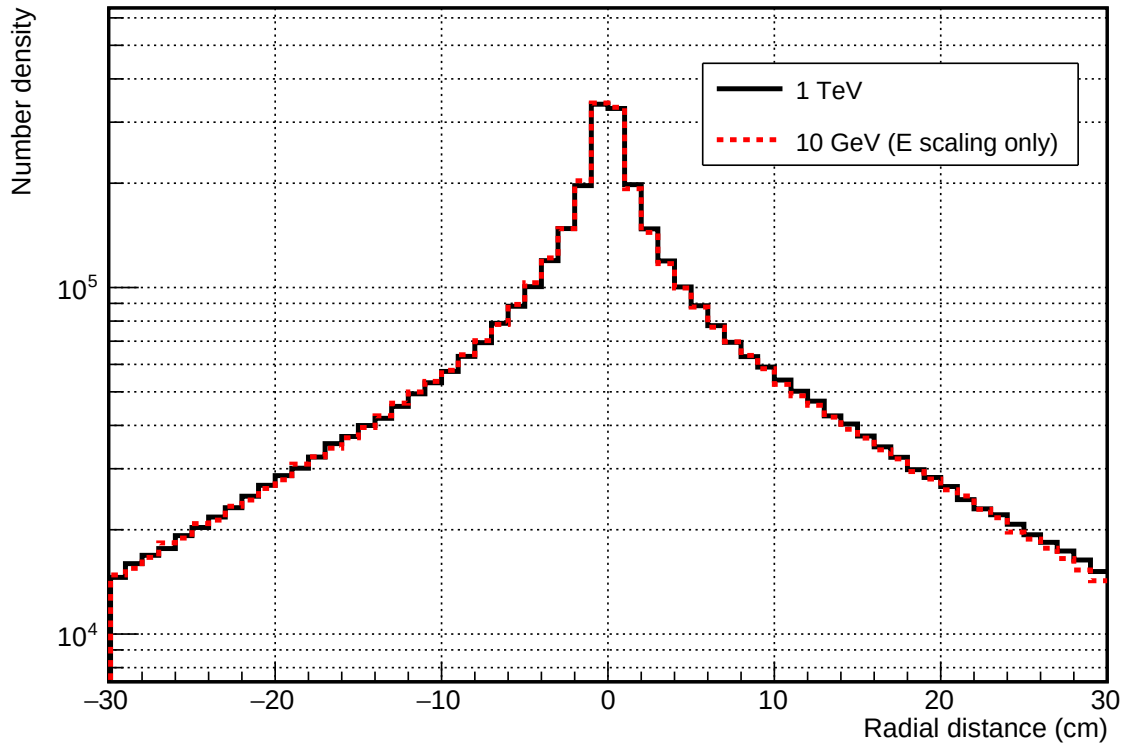

Figure 4.6: Example radial distribution of shower particles in GEANT4, showing the invariance in lateral distribution as a function of primary particle energy. The 10 GeV shower has been scaled by a factor of 100 and overlaid with an unscaled 1 TeV shower profile.

GEANT4 can produce showers on a personal computer at energies up to roughly 10 TeV, but beyond that, it becomes computationally inefficient to produce a large sample. Therefore, in order to efficiently produce showers at higher energies in large numbers, simple linear scaling is applied, both in the longitudinal direction and in time, to showers of lower energies. To calculate the correct scaling factors, numerous GEANT4 showers were produced at decades of primary particle energy from 100 MeV up to 10 TeV and analyzed.

The radial distribution for a shower in a medium is largely independent of primary energy, with 90% of the particles contained within 1 Moliere radius, which for ice is $\sim$10 cm. This is

shown in Figure 4.6, where a 10 GeV shower has been scaled by number density only, which makes the lateral shower profile match a 1 TeV shower profile. The longitudinal length of the shower scales with the primary energy, as does the shower duration. Therefore we apply the proper scalings to the longitudinal and time components for each ionization 4-vector in the shower for a target primary energy, and scale the number density accordingly. This results in shower profiles which mimic those at energies beyond what is accessible in GEANT4. A comparison of a 1 TeV shower with a 10 GeV shower that has been scaled up is shown in Figure 4.7, showing good agreement in longitudinal profile. For computational efficiency, a scaled 10 GeV shower is used in the RadioScatter module for all higher energies. While this is clearly not an ideal description of shower shape at very high energies, this technique allows for a reasonable approximation for the purposes of this simulation. We note that the longitudinal scaling factor required to scale a 10 GeV shower length up to that of a 1 EeV shower is $\sim$4, so the maximum scaling is overall less than an order of magnitude. The length and time scaling can be turned on and off by the user in RadioScatter.

We note that RadioScatter neglects the Landau-Pomeranchuk-Migdal (LPM) effect[92][93] in the longitudinal shower profile. This effect, detailed for the radio problem in [94] and [95], is a suppression of low-energy bremsstrahlung and pair production in showers at very high energies, resulting in an effective lengthening of showers in the longitudinal dimension. This effect would have minimal impact on the radar problem as the extended tail of the distribution at thigh energies has a low number density relative to shower maximum, and therefore will not be part of the overdense scattering discussed above.

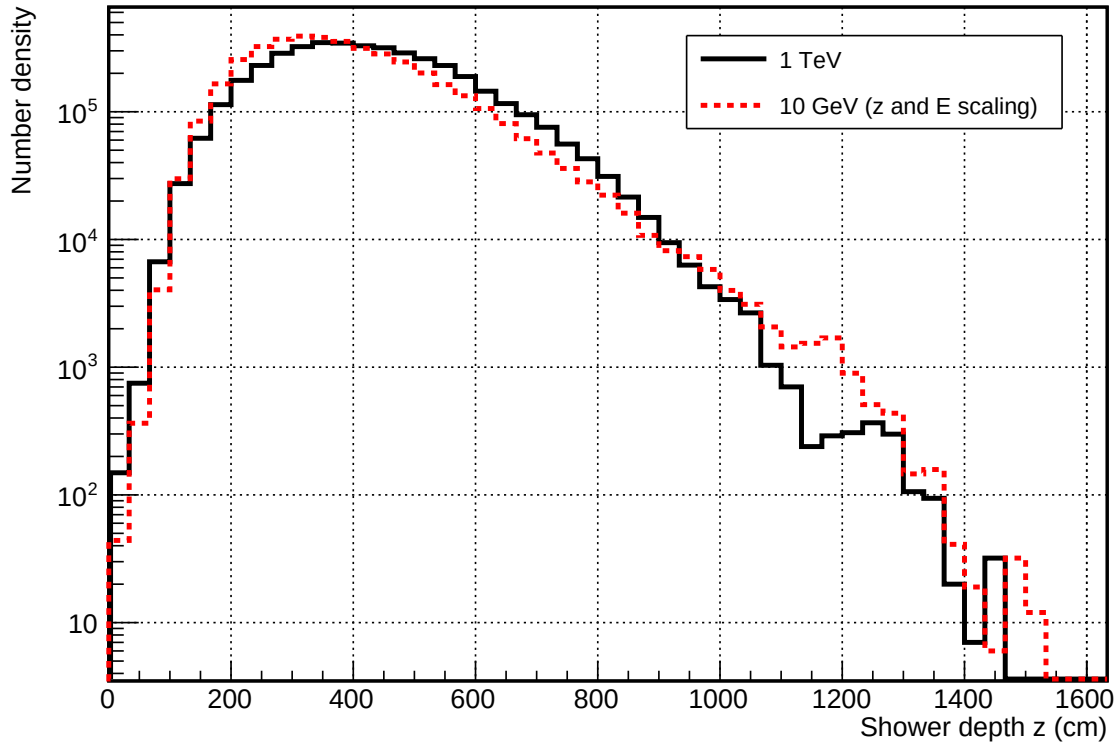

Figure 4.7: Longitudinal distribution of showers in GEANT4. A 10 GeV shower has been scaled in number density and the longitudinal dimension to match a higher energy, 1 TeV shower.

4.1.5.2 Calculation of the signal

From the 4-vectors of ionization electrons provided by the GEANT4 simulation, we calculate the scattered fields for a specified interrogation frequency using the real part of Eq. 4.19. The resultant fields for all PSP particles are propagated back to the receiver and summed in time bins corresponding to the user-defined sampling period. For example, the resultant real part of the total electric field at the receiver for a single sampling period T is given by

$$Re\left[\mathbf{E}_{tot}\right] = \frac{1}{T}\sum_{n=1}^{N}\int_{t}^{t+T}\Theta(t'-t_n^i)\Theta(t_n^f-t')Re\left[\mathbf{E}_n(t)\right]dt, \tag{4.23}$$

where $\mathbf{E}_n$ is given in Eq. 4.19. $t' = (t - |\mathbf{R}|/c)$ is the retarded time at the position of charge n, and the step functions ensure that the charge n exists at the retarded time, with t_n^i and t_n^f being the

production and recombination/attachment (initial/final) times, respectively, for charge n. These are a function of the plasma lifetime τ. The factor $1/T$ is present because, in practice, a standard digitizer effectively averages the measured voltage over the sampling period, so we similarly calculate the average value of each $\mathbf{E}_n$ over a single sampling period, in order that the displayed voltage will be independent of the time base, and sum these average values. We then take this electric field $\mathbf{E}_{tot}$ and multiply by an antenna effective length to obtain, e.g. the voltage read on an oscilloscope.

4.1.5.3 Example signal

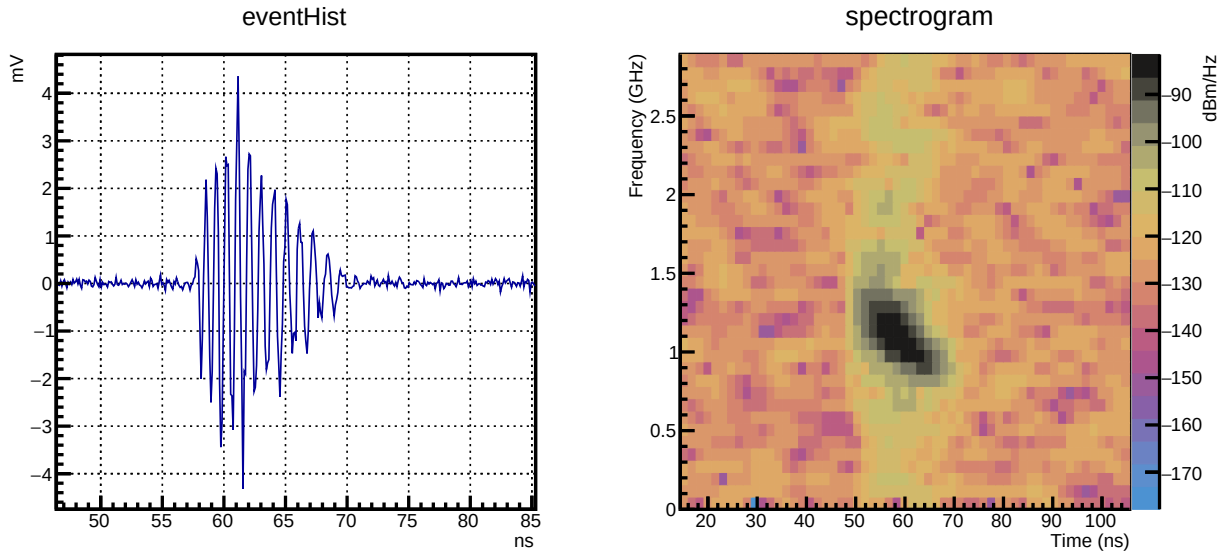

Figure 4.8: Simulated radio reflection for a 5 GHz bandwidth receiver, from an electron-initiated plasma consisting of 10^9 13.6 GeV primaries, superimposed upon thermal noise, with a sounding frequency of 1.15 GHz CW. The transmitter output power is 10 W and the plasma lifetime is 0.1 ns. The observed chirp-like signal is a function of the TX-PSP-RX geometry.

Figure 4.8 is an example of a simulated reflection from a GEANT4 shower using RadioScatter, where we have used Eq. 4.1.5.2 to build up a time-domain signal. In this simulation, a 13.6 GeV electron beam with a bunch count of 10^9 electrons (scaled per the above discussion, to the parameters of our upcoming SLAC testbeam, discussed below) is incident on high-density polyethylene (HDPE). The target is interrogated with 1.15 GHz continuous-wave (CW) radio signal at 100 mW output power, with horizontally polarized (i.e., antennas in the same plane as the shower axis) TX

and RX. The plasma lifetime is set at 0.1 ns, and will be discussed further below.

The 'chirp' signal of Figure 4.8 is a function of the TX/RX proximity to the shower in this test-beam setup. For geometries where the TX-PSP baseline is much greater than the length of the shower itself, the 'chirp' is replaced by a CW return at a shifted frequency away from the carrier. Experimentally, such a unique signal can be used to advantage in a low signal-to-noise trigger, as in [65][66]. The phase relationships between reflections from different parts of the plasma as it progresses through 4-space result in a coherent frequency shift of the received signal, even though none of the scatterers themselves have any appreciable 3-velocity, and the interrogating radio is monochromatic. This shift, observed in both the horizontal and vertical polarizations, is a function of the TX-PSP-RX geometry, and can be used to deduce position and direction information of the primary particle. Detailed analysis of the frequency shift/geometry relationship will be elucidated in a forthcoming article.

The TX–RX–PSP geometry for this event is shown in Figure 4.9. In this example, the coordinate system is set so that the shower vertex occurs at (0,0,0) and the shower evolves in the $+\hat{z}$ direction.

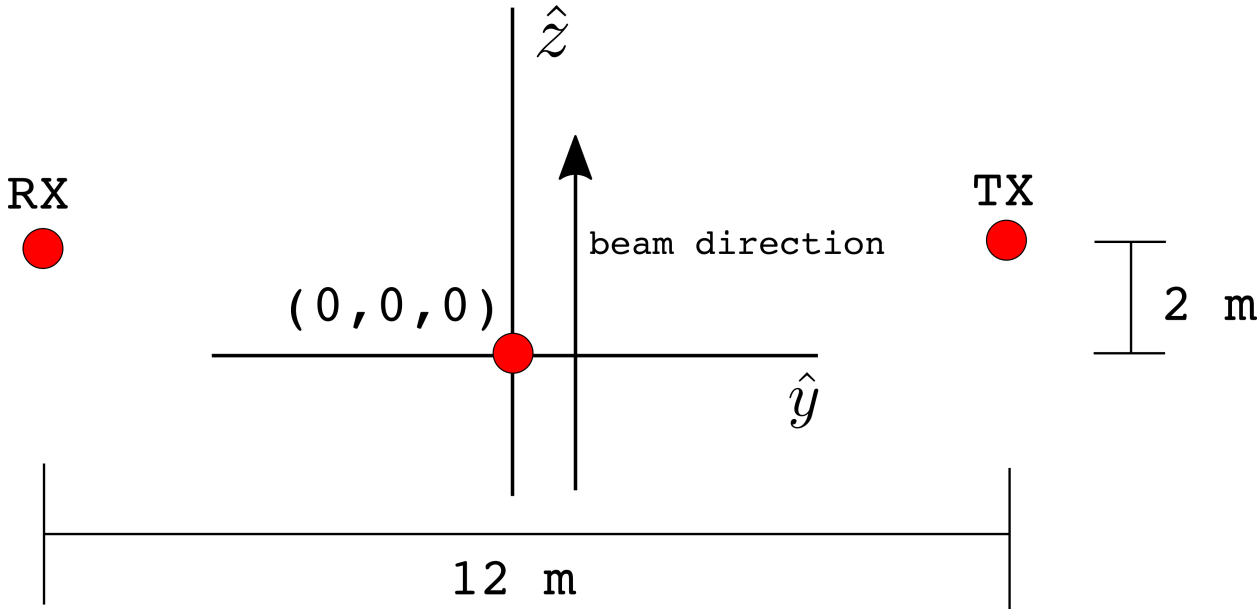

Figure 4.9: The geometry of the radar set-up for Figure 4.8. The shower vertex is at (0,0,0) with the shower progressing in the $+z$ direction.

4.1.5.4 Plasma lifetime

A primary unknown in the PSP problem is the true plasma lifetime τ for a given material, presumably dominated by ionic recombination or attachment to neutrals. In the classical picture, a free charge will oscillate in phase (or directly out-of-phase, if the charge is negative) with an incident field. In the limit that τ for this charge approaches zero, that is, $\tau << 1/f$, where f is the interrogation frequency, the charge does not "live" long enough to make a full oscillation. Instead, the charge gets a 'kick' from the field, with a direction dictated by the polarization and phase of the incident RF at that point in 4-space[104].[II] The different time-scales are compared graphically in Figure 4.10. For this reason, we expect to see coherent scattering even for lifetimes well below the period of an interrogating wave, since the individual, short-time kicks are correlated, being functions of the incident wave. And indeed, though the amplitudes are diminished, coherent scattered signals are seen in the simulation at lifetimes as short as 100 ps.

[II]This 'kick' is due to the interrogating field. We assume the electron pops into stationary existence upon ionization, gets a kick from the field, and pops out of existence upon attachment or recombination. It is assumed that the start and end points of this process result in negligible RF emission, due to the non-relativistic velocities involved.

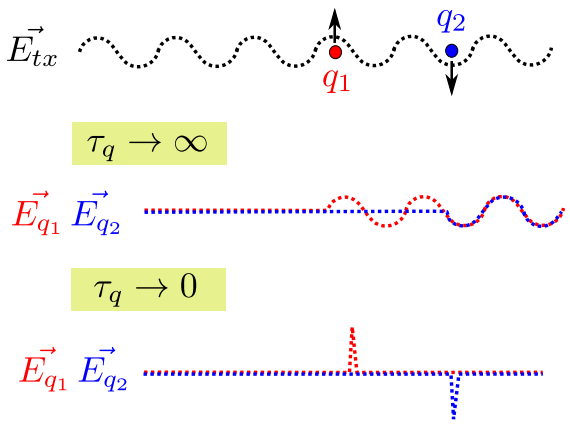

Figure 4.10: Graphical representation of the limiting cases for the free electron lifetime τ. As $\tau \to \infty$, once the charges q_1 and q_2 are freed from the medium, they begin to radiate in phase with the incident field. As $\tau \to 0$, the charges move only briefly (less than a single oscillation period), and their polarity is given by the instantaneous phase of the incident RF.

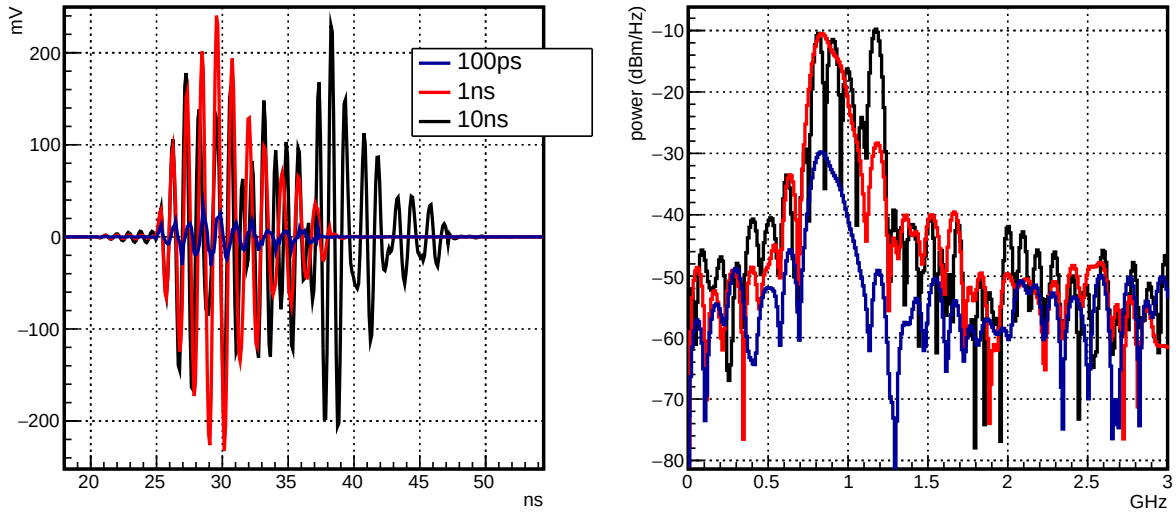

Figure 4.11: Time-domain signals (left) and frequency spectra (right) for various user-defined lifetimes in RadioScatter. The interrogating frequency is 1.15 GHz, and the geometry (Figure 4.9) is such that we expect chirp-like behavior during shower progression.

The plasma lifetime τ is user-defined at runtime in RadioScatter. Changing τ changes the

phase relationships for re-radiation of the incident signal as a function of time. Using the same TX and RX geometry as in Figure 4.9 and a sounding frequency of 1.15 GHz, the resultant signals for $\tau = 100$ ps, 1 ns, and 10 ns are given in Figure 4.11. The chirp-like frequency shift, an expected function of the geometry of the setup and the progression of the shower, is observed for all lifetimes. The duration of the return signal scales with lifetime, with the spectrum becoming more dominated by the carrier frequency as the lifetime increases. This is fully expected, as the carrier component of the Fourier spectrum is increasingly well-defined with more cycles. That is, the return signal becomes dominated by reflection from a stationary conductor as the plasma lifetime increases. Comparison of empirical results, derived from our testbeam experiment, with these simulation signals will provide experimental bounds on τ.

4.1.5.5 Collisions

Collisional effects, which become evident at primary energies $> 10^{16}$ eV, and should roughly scale with density, are a further unknown in the model. The three dominant collision species are electron-electron, electron-ion, and electron-neutral.

We employ Eq. 4.3, using simple atomic and molecular cross-sections for the σ_s terms. In general, the dominant collisional species in a plasma is a function of the degree of ionization of the medium. For a dense material such as ice, the number density of neutral, non-ionized molecules exceeds the number density of free charges by several orders of magnitude, so it is likely that the electron-neutral collision rate dominates. But, because the transport and collision rates are not well-known for ice, we calculate the collision frequency using the molecular cross section of water [105], and, in the absence of experimental data, multiply by a factor of three to conservatively account for all species, including ions and electrons. Our testbeam experiment measures the sum of these three collisional effects.

4.1.5.6 Antenna response

RadioScatter allows the user to input an antenna gain pattern as a text file with gain, specified separately for TX and RX, as a function of polar and azimuthal angles. If no such antenna pattern is used, the antenna effective height[106] is set at λ, essentially making it an idealized antenna with dipole gain at every frequency. This can of course be changed by the user. Planned for future releases of RadioScatter is an antenna system response that can be convolved with the received signal. This response can be a complex effective height, or a group delay, or an impulse response– i.e., all the variables which characterize the dispersion and amplitude response of an antenna.

4.1.6 Upcoming experimental test

The end station test beam (ESTB) facility at the SLAC National Accelerator Laboratory is a user facility which allows researchers to install targets and detectors downstream of a $\mathcal{O}$(1 Hz) switched electron beam (roughly 10^9 10 GeV particles per bunch) from the main linear accelerator. We have proposed using the well-characterized T-510 experiment[52] target of high-density polyethylene (HDPE) to approximate an in-situ PSP mimicking that of a neutrino/ice interaction. We will then interrogate the PSP within the HDPE target with CW radio, and measure the scattered RF signal. Figure 4.12 shows the experimental setup, which was originally designed and optimized for measuring the combined Askaryan and geomagnetic emissions from air showers.

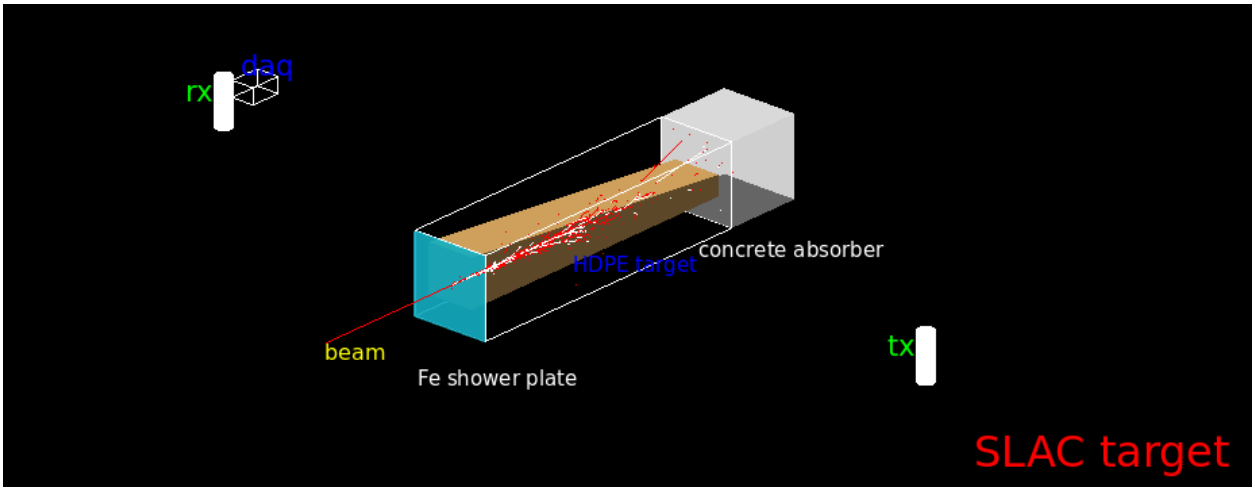

Figure 4.12: GEANT4 representation of the SLAC beam line test, showing a particle shower inside of the HDPE target. The size and type of antennas are not to scale, although the relative distances are approximately accurate for an interrogation frequency of 2 GHz.

This experiment, T-576, is tentatively scheduled for mid-2018. The expected signal for the configuration shown in Figure 4.12 is presented in Figure 4.8, with separation distances as given in Figure 4.9.

4.2 Part Two: Expected Science Reach

We now consider the radar signals from showers induced by high energy neutrino collisions in ice. In what follows, the transmitting frequency is 450 MHz unless otherwise stated, and, for distant neutrino interactions, the measured attenuation length $L_A = 1/\xi$ of ice [107] is used in all calculations. Additionally, a plasma lifetime of τ_p =1 ns is used for all calculations.

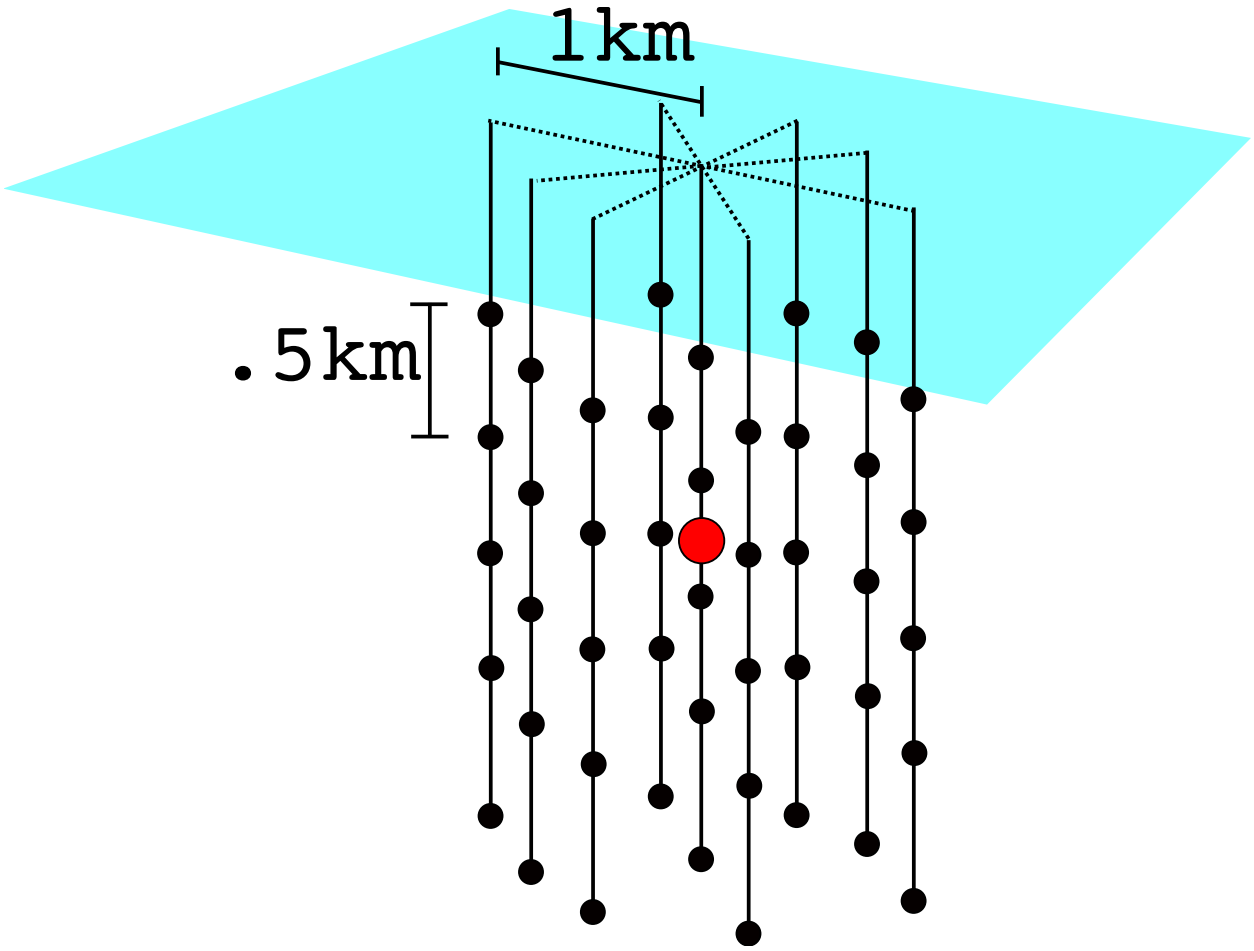

Figure 4.13: An example detector setup for an in-ice radio scatter system. The larger red circle is the transmitter, and the smaller black circles indicate receivers. This station spacing is largely based on measurements of radio attenuation length in ice, to maximize effective volume.

4.2.1 Effective Detector Volume

The main advantage of the radar technique over current strategies is the ability to scale up the transmitter power, and thus effectively increase the volume of ice in which a candidate neutrino signal may be detected. Since RF/optical experiments detect signals produced by particle showers, as opposed to detecting the shower particles directly, an energy-dependent "effective volume" quantifies the amount of sensitive target material accessible to a given detector.

Figure 4.14 shows the effective volume of a proposed radio scatter experiment in ice for various values of transmitter output power. The TX-RX configuration for Figure 4.14 is shown in

Figure 4.13, and consists of a single transmitter surrounded by 45 receiving antennas, 5 on each of 9 'strings'. To produce this plot, $N(E)$=5000 showers were produced at each decade of energy from 10^{14} eV to 10^{19} eV and distributed randomly within a V=10×10×2.8 km volume, to mimic the ice sheet at the South Pole. The effective volume $V_{eff}(km^3sr)$ at each point in energy E is given by Eq. 4.24.

$$V_{eff} = 2\pi V \frac{n(E)}{N(E)}. \tag{4.24}$$

Here, $n(E)$ is the number of events detected at each energy. For simplicity we use a solid angle factor of 2π instead of 4π to restrict our study to down-going neutrinos (given Earth absorption), and assume a uniform distribution of interaction points within the target volume. We set an edge detection threshold of 45 μV at each receiver, corresponding to a signal-to-noise ratio (SNR) against thermal noise for a 1.2 GHz bandwidth of roughly SNR$\sim$3, and, given the characteristic signature of radar signals, we consider an event to be "detected" if any of the antennas trigger at this level. We mention that trigger SNR thresholds of 1:1 have been achieved in experiments designed to detect radar reflections from extensive air showers[60]. For a 9-station deployment around a single, centrally located 10 kW transmitter, a radio scatter experiment is projected to have greater sensitivity than IceCube above 1 PeV, and the projected sensitivity of the newly-deployed ARA phased array[108] up to $\sim$0.5 EeV. The increase in effective volume over current strategies is even more pronounced by raising the transmitter power to 100 kW (the typical output power for a terrestrial FM radio station). The radio scatter method is therefore a potential technique for bridging the gap between existing optical and RF detection schemes, essential to establishing the neutrino flux spectrum above 1 PeV[109].

Not included in the calculation (at the time of this writing) is a full treatment of the bending of rays in the slowly changing index of refraction over the upper $\sim$200 m of the Antarctic ice sheet. This is a geometric effect which will primarily result in re-distribution of signal flux and the presence of some shadow zones at horizontal viewing angles[110]. We have therefore placed our receivers and transmitter in deep ice ($>$ 200 m deep), where the index of refraction is nearly constant, to mitigate the effect of such ray bending in the simulation.

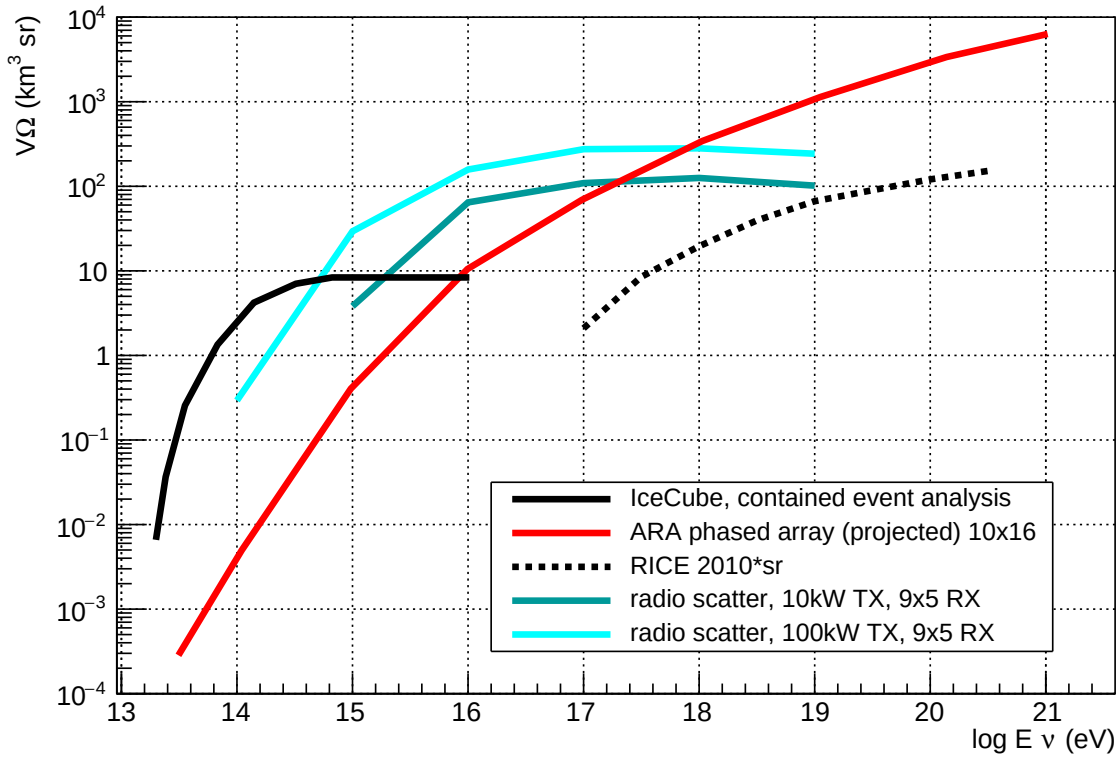

Figure 4.14: Effective volume for a radio scatter experiment, for SNR=3, as a function of primary particle energy, for a 1 TX, 9 station configuration. Each station is a vertical string of 5 antennas. The geometry is shown in Figure 4.13. Curves correspond to fixed transmitter output power. For comparison, we also show the effective volume for RICE (reproduced from [48]), IceCube, and the projection for the ARA phased array with a ten station (16 phased antennas per station) configuration(reproduced from [108]).

4.2.2 Geometric acceptance

The geometric acceptance for the radio scatter technique is perhaps the most compelling rationale for further development of the technique, and is largely responsible for the apparent advantage over Askaryan detectors at $<$ EeV energies. The Askaryan signal exploited by current experiments is forward-beamed, with measurable amplitudes constrained to the Cherenkov angle, corresponding to a restricted geometric aperture[55]. By contrast, the radar scatter is more isotropic, with measurable returns over a large portion of solid angle for a given shower direction and transmitter location. The reflection is increasingly localized to the specular reflection angle as τ and energy

increase (e.g. anything that increases the length of the PSP, as detailed in [90]), but for <10 ns lifetimes and < EeV energies, the advantage in geometric acceptance over Askaryan is pronounced.

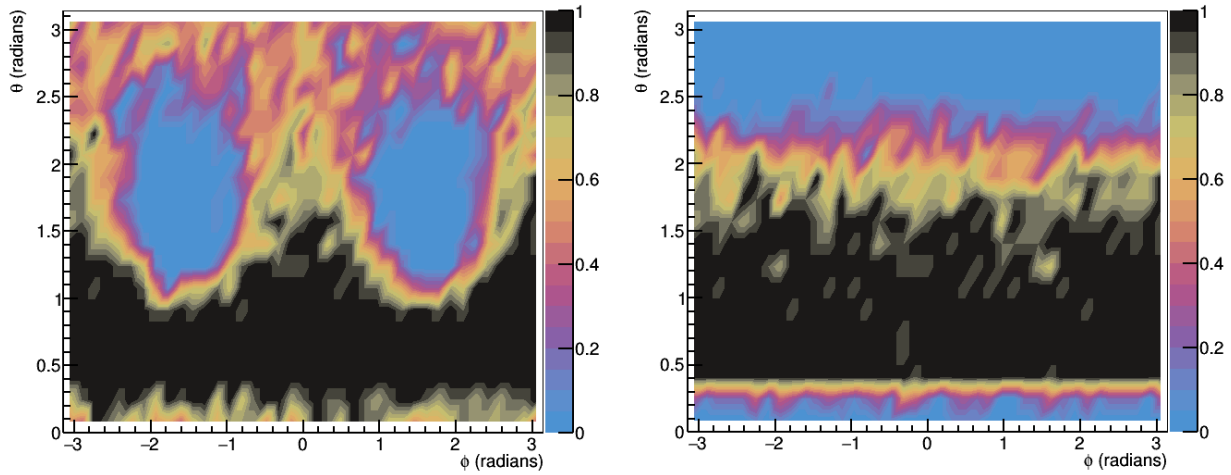

Figure 4.15: Trigger efficiency maps for a requirement of SNR≥10 as a function of angle for a 10^{16} eV primary ν at a radial distance of 1 km from the shower vertex. Left: vertically polarized TX and RX (perpendicular to, and out of the plane of, the shower axis). Right: horizontally polarized TX and RX (parallel to, and in the plane of, the shower axis). Angle and polarization conventions are shown graphically in Figure 4.5.

Figure 4.15 shows the trigger efficiency at SNR≥10 for a 10^{16} eV primary ν with τ =1 ns at a fixed radial distance of 100 m from the receiver as a function of spherical coordinates ϕ and θ. To produce these maps, the transmitter position is fixed at $\mathbf{r_{TX}}$ =(100, 0, 0)m, the shower is produced at $\mathbf{r_s}$ =(0, 0, 0)m, with it's momentum direction vector $\hat{\mathbf{p}}_\mathbf{s}$=(0,0,1). The received signal is calculated, sampling in azimuth and elevation, at a fixed radial distance r_{RX} =100m from the vertex. A trigger efficiency (i.e. n/N, where n is the number detected and N is the number thrown) is then calculated at each point. These threshold maps are very similar to dipole radiation patterns for vertical and horizontal antennas, respectively. We observe that a high percentage of the solid angle map has high trigger efficiency.

4.2.3 Potential experimental realization

An in-ice radio scatter telescope could be co-deployed with a proposed future expansion to the current IceCube experiment, with no additional drilling overhead. The geometry of Figure 13, with 9 holes drilled to a depth of 2.5 km, and each of the 8 perimeter holes laterally displaced 1 km from the center hole is roughly commensurate with that Gen-2 proposed upgrade. The transmitter is deployed in the center hole, along with one detector string, each consisting of 5 antennas separated vertically by 500 m. This value is approximately half of the estimated radio-frequency attenuation length in the upper half of the South Polar ice sheet.

For a 10-100 kW transmitter, an isolated location is most desirable, so as to not interfere with other experiments. A remote Antarctic location, such as Dome C, or a location in Greenland may be candidates for such a deployment. In this paper, we have assumed the well-parametrized ice properties measured at South Pole, which also sites other neutrino detection experiments and therefore offers an opportunity for complementarity. A sufficiently deep transmitter at South Pole should not interfere with other experiments, with RF "leaking" out to the air only at angles approximately normal to the surface. Transmission from ice to air will be suppressed at more glancing angles, owing to the Fresnel coefficients.

We have only considered CW here so far in this article, but a detailed study of modulation of the transmitted signal will follow. Modulation of the transmitted signal (standard practice in conventional radar systems) is a further way to lower SNR, increase vertex resolution, and increase sensitivity at lower energies.

Both the transmitter and the detector strings could be solar-powered during the austral summer, and wind-powered in the austral winter. Data may be relayed from the strings to a central hub via microwave ethernet link, or both power and data may be transferred via trenched cables.

We mention that a preliminary implementation of the method could be performed by deploying a single transmitter and incorporating a new firmware module trigger into the existing ARA experiment at South Pole. The ARA array, though not ideally spaced for a radio scatter experiment, covers a sufficiently large area to be sensitive to the radio scatter method. Details of an

implementation for ARA will be presented in a companion article.

4.2.4 Discussion and outlook

We have presented a particle-level model for radio/PSP interactions that can be simply incorporated into a GEANT4 simulation via the software module RadioScatter. We have shown that the sum of reflections from individual scatterers results in an appreciable scattered signal amplitude with coherent phase. We have included the effect of plasma screening and collisions, and observe appreciable signal amplitudes for plasma lifetimes as short as $\mathcal{O}$(100 ps). An in-ice detector with a single 10 kW transmitter has been presented, which has higher calculated sensitivity to neutrinos between 1 PeV and 1 EeV than current optical and Askaryan detectors. This model will be tested in a test-beam experiment at SLAC, planned for spring, 2018. Many of the unknowns in the problem, including the plasma lifetime τ, are direct observables in this experiment. Pending experimental verification, we hope that the radio scatter method can be incorporated into future high energy neutrino detector designs.

Chapter 5

SLAC T576: Coherent Radio Echoes from an Electron-Beam Induced Particle Cascade

5.1 Introduction

A particle shower in a medium produces high energy particles that traverse that medium, ejecting ionization electrons from atoms in the bulk as the shower evolves. For high enough incident energies, this ionization may become dense enough to reflect at radio wavelengths, approximating a short-lived, cylindrical conductor. The Telescope Array RAdar (TARA) [59] project was the first dedicated experiment to attempt detection of the extensive air shower (EAS)[24] from a cosmic ray interaction in the atmosphere using the radar method. TARA reported no signal [60], but placed a strong experimental limit on the extant model of in-air radar reflections [61]. Several experiments have sought to detect radar reflections from ionization deposits in a laboratory setting [62, 63, 64]. The Chiba [62] group reported positive results for reflections from ionization deposits in dense material, albeit not from particle shower-induced ionization. The T576 experiment at SLAC was designed to make the first direct measurement of radar reflection from the ionization produced by a particle shower.

The $\mathcal{O}$(1-10 GeV) electron beam at SLAC has a nominal bunch number of 10^9 electrons. Di-

recting this beam into a target of high-density polyethylene (HDPE) produces a shower equivalent to that produced by a 1 EeV primary neutrino, which can be interrogated with radio in an effort to quantify the ionization parameters of a true neutrino-induced cascade. To that end, Testbeam experiment 576, or T576, ran in May 2018.

5.2 Experimental Setup

The End Station Test Beam facility provides users a $\mathcal{O}$(1 Hz) bunch of high energy electrons switched from the main linear accelerator (linac) over into End Station A (ESA). ESA is a 'parasitic' user facility at SLAC; i.e., the parameters of the electron bunch (energy, beam current) are selected by the main linac user, rather than the End Station user. For our purposes this was actually advantageous, as a scan of energies and currents allowed investigation of how a putative signal depends on those parameters. For T576 the beam current was typically $\sim$250 pC, corresponding to roughly 10^9 electrons per bunch. The run-time variation of the beam current is shown in Figure 5.6. The primary electron energy varied from 10–14.4 GeV throughout the experiment, with most of the data accumulated at 14.4 GeV. At the point where the beam exits the beam pipe at the end of the ESA, the bunch is highly collimated, occupying less than a cubic centimeter in volume.

Figure 5.1 shows the target assembled on-site at End Station A at SLAC. The HDPE target was initially constructed for the T510 [52] experiment, for which it was used to study the geomagnetic emission from a particle shower created within the plastic target. For T576, the HDPE target was aligned with the beam by placing it on top of large concrete blocks. Transmitting and receiving antennas were positioned around the target in various configurations throughout the experiment, as described in detail below. Two different types of antennas were used: an LPDA having voltage standing-wave ratio (VSWR) less than 3.0 over a 1-18 GHz bandwidth, and a Vivaldi antenna with a 0.6-6 GHz bandwidth. The transmitter and receiver amplification was varied throughout the experiment as well, in order to quantify and mitigate backgrounds and also investigate the scaling properties of observed signals.

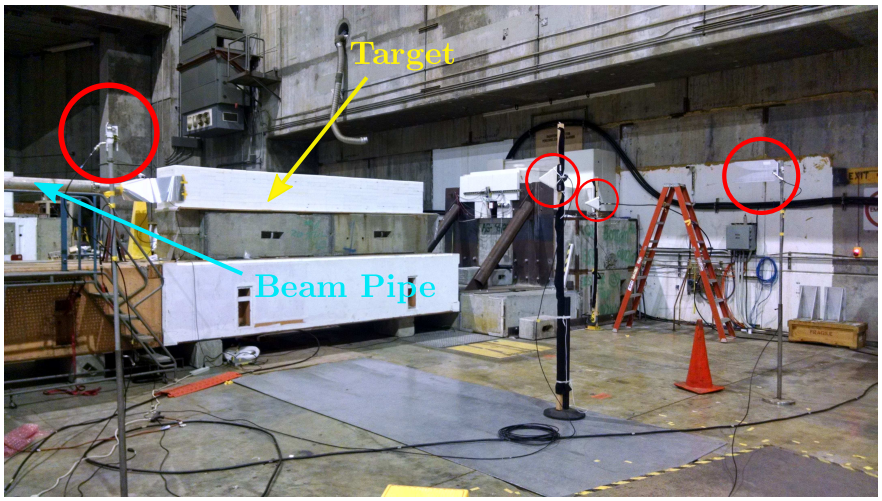

Figure 5.1: The T576 experimental setup. The large white rectangular polyhedron at the center is the HDPE target. The beam enters from the left, with the entry point shielded by aluminum sheeting in an effort to mitigate transition radiation (TR). The circles (red online) indicate the receiver/transmitter antennas. Second from left is the transmitter, the others are receivers.

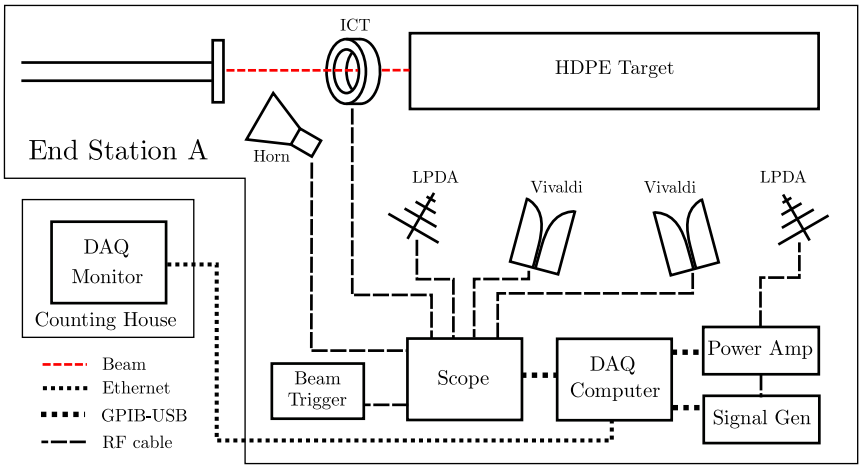

Figure 5.2: The T576 signal chain. The DAQ system and transmitter resided in the End Station A, and were remotely monitored via an Ethernet link from the 'counting house', a remotely accessible location for users while the beam is on. The various components shown are described in the text.

A typical signal chain and the DAQ configuration are presented in Figure 5.2. In the later analysis section, more detail will be given on the amplification and filtration choices made for various 'runs' during the experiment. The DAQ was a Tektronix TDS-694C 4-channel, 10 GS/s digital oscilloscope, connected to a laptop via a GPIB-USB adapter. This laptop was remotely accessible via a network link from the 'counting house', which allowed for control of all scope parameters and real-time readout of the data. The transmitter, a Rhode and Schwartz SMHU signal generator, was also controlled remotely via the same computer with another GPIB-USB adapter, allowing real-time frequency and output level tuning. The final piece of equipment (also controlled via GPIB cable) was an Instruments for Industry SMCC100 power amplifier for the transmitter, permitting output level variation, as well as automatic levelling control and queries for forward and reflected power. As no personnel are allowed inside of the End Station during operation, having such a high degree of remote control over the parameters of the experiment was critical for minimizing down-time for hardware adjustments, thereby allowing accumulation of as much data as possible. An integrating current toroid (ICT) was used to monitor the beam current for every event, and occupied the 4th channel of the scope for the duration of the experiment.

The scope was triggered by either a) a logic pulse from the accelerator itself or b) a sharp transition radiation signal from an s-band horn (indicated by 'horn' in Figure 5.2), depending on the run. The TR horn signal was very sharp and consistent, but most of our data was taken using the beam logic pulse as a trigger since it could be modified remotely to allow precise time shifts of trigger point relative to the true arrival of the beam. Later runs substituted a third receiver antenna for the s-band horn, to better characterize the expected reflection signal as a function of angle.

Part-way through the run, the reported power amplifier output level began to drift by approximately 20% compared to the actual output power (determined by observing signal strength in the scope). In what follows, we therefore assume a 20% systematic error on the transmitter output power.

5.3 Specific Measurements and Goals

For T576 and the radar problem, there are model-dependent and model-independent measurements that can be made. Model-dependent measurements in this case correspond to those observables which are dependent on multiple parameters, e.g., the plasma lifetime and the microscopic scattering physics. The spectral content, temporal duration and angular distribution of signal are important observables that will ideally either falsify or confirm different models. Simple measurements of coherence [111], that is, whether the received power in the signal region scales with distance as R^{-4}, and linearly with transmitter power, are considered model-independent measurements.[I] For T576, we attempted as many different combinations of measurements as possible to test our results in both model-dependent and independent manners.

Figure 5.3 shows the configuration for one run. In this run, all three receivers are positioned on one side of the target. One receiver was positioned at the specular reflection point for shower maximum (calculated to be roughly 3 m longitudinally into the target), with the other two set off at either side. This provides a model-dependent measurement. A large stationary conductor in the target region was positioned so as to reflect at the specular point; reflected amplitudes should decrease sharply as the receivers move away from this point, assuming a sufficiently long plasma lifetime. If, however, the plasma lifetime is short, then the majority of scattering may be in the single-particle regime, which is far more isotropic. Observation of reflection in the non-specular receivers would therefore point to a short plasma lifetime.

The overall goal of T576 was to measure an unambiguous radar reflection from a particle shower. The next sections will discuss the challenges to making such a measurement and the analysis of the data. As will be discussed, the extremely high backgrounds made many of these goals difficult to attain. However, after applying a particularly sensitive method for small-signal detection in large backgrounds, we present strong suggestions of a signal which warrant further investigation.

[I] The R^{-4} scaling derives directly from the radar equation, which more specifically prescribes a scaling $\propto R_1^2 R_2^2$, where R_1 is the distance from transmitter to reflector and R_2 is the distance from reflector to receiver. For a fixed baseline, the received power should scale linearly with transmitter power.

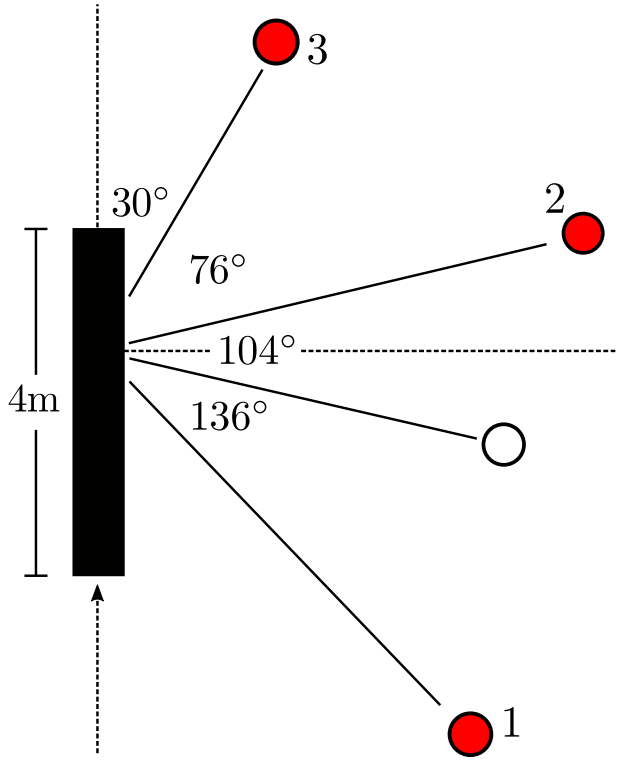

Figure 5.3: The setup for run 11 of T576, viewed from above, and drawn to scale. Closed circles are receivers, labeled by their DAQ channel number, open circle is the transmitter. One receiver is at the specular reflection point relative to calculated shower maximum; the others are separated from the specular angles by 30–40 degrees.

5.4 Backgrounds

There were several backgrounds at ESA during T576 data-taking. The typical radio-frequency (RF) backgrounds, anthropogenic and generic low-level electromagnetic interference (EMI), were relatively low within the thick concrete bunker-style building of the ESA. Occasional bursts of communications radio were observed, but well-below trigger threshold. The two most pernicious backgrounds were observed to be room reflections and a very strong RF signal from the beam/target interaction itself.

5.4.1 Spurious Reflections

The ESA is characterized by many sharp angles, reinforced concrete, and randomly placed metallic equipment accumulated over decades of previous experimentation. For most particle physics applications, this is irrelevant, but for radio, each conducting surface is a reflector that can affect the signal seen at the receiver. The reflections in the room were so pervasive that moving a receiving antenna relative to the transmitter by several centimeters could, in extreme cases, reduce the received amplitude of a CW signal by an order of magnitude. Typically such reduction is achieved through active carrier cancellation (a procedure whereby the transmitted signal is split and one half is fed directly into the line of the receiver, to be combined with the signal arriving at the receiving antenna. With proper alignment, the phase of the combined signal cancels the otherwise-large carrier in the receiver completely, and thus allow for smaller SNR signals to be seen in the receiver stream), but at ESA, reflections from myriad surfaces required scanning for receiver nulls empirically. Once a receiver was positioned at such a null, an additional 'foil test' calibration was performed to verify that the addition of a reflecting surface at the expected location of the reflecting shower would result in a clear signal enhancement (compared to the no-foil configuration) at that receiver. For some configurations, it was observed the foil test would result in a further nulling of the signal, indicating a poor receiver location for that particular frequency. For others, such as the one shown in Figure 5.4 the amplitude of the carrier with the foil in place is approximately twice

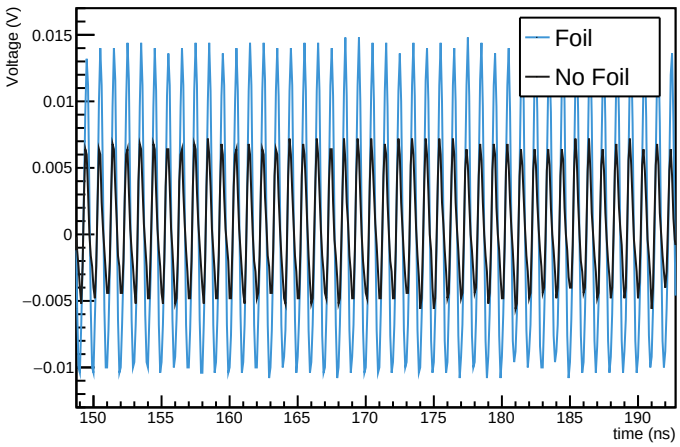

Figure 5.4: A 'foil test', for which a conductor (here 0.3 m $\times$ 1 m) is placed at the expected ionization maximum point on the target, to estimate how a reflection should be observed in the receiver. In this test, the foil reflection is in phase with the ambient background, indicating a good receiver position.

larger than without, indicating a favorable receiver position.

The foil tests were also quite useful from a simple physics standpoint – reflections with a piece of foil on the order of the expected dimension of the ionization plasma gave a crude approximation of the signal amplitude to be expected during the run. In good agreement with pre-run simulation, amplitudes of $\mathcal{O}$(1 mV) were observed.

5.4.2 Beam Splash

The second, far more challenging background was the so-called $\sim$100 mV, several hundred nanosecond duration 'beam splash', which likely is the result of somewhat complicated physics at the point at which the beam strikes the target. This background likely combines sudden appearance [112], transition radiation [113, 56, 114], and Askaryan radiation[44, 47], plus myriad reflections from the room and from within the target itself. Beam splash was observed at all values of θ, as shown in Figure 5.6, but was more pronounced in the forward beam direction, as expected (additional details on beam splash will be presented in the analysis section).

It is worth noting that beam splash would not be present for an experiment seeking to use this

technique to detect in-ice neutrinos. The only background to the radar signal, from the shower itself, would be the Askaryan signal, over a very restricted solid angle.

5.5 Data Analysis

This section describes data analysis for one of the cleanest runs, towards the end of the experiment, when most of the backgrounds had been at least partially-characterized. We follow a technique, first taught to the author by JP Ralston, which employs several different methods of matrix decomposition to filter background and extract signal [111]. We present evidence for a possible signal, and suggest a follow-up beam test with slightly different parameters to definitively establish this signal.

5.5.1 Setup

For this run (run 11), antennas were aligned vertically (VPol), and there was no active carrier cancellation. The present analysis will focus on data taken using a transmit frequency of 1 GHz and 5–25 W output power. The layout of the receivers are given in Figure 5.3, and the plots to follow are based on data taken from channels 1 and 2, which were both Vivaldi receiver antennas. There was no filtration or amplification on the input of the receivers, to avoid possible saturation effects, and to initially maximize receiver bandwidth.

5.5.2 Raw Data

Figure 5.5 shows an event from run 11 taken in the counting house at run-time. The 4 panels on the left are the oscilloscope time traces, uncorrected for cable delays and time-of-flight. From top to bottom these are CH1, CH2, CH3, and CH4 (ICT), respectively; corresponding Power Spectral Densities (PSD) are presented in the right panel. As evident on the Figure, the amplitude of the beam splash is greater than 100 mV. In Channel 3, downstream of the beam, the amplitude exceeds 1 V. The heavy peaking in the spectrum is likely a combination of system response and the room

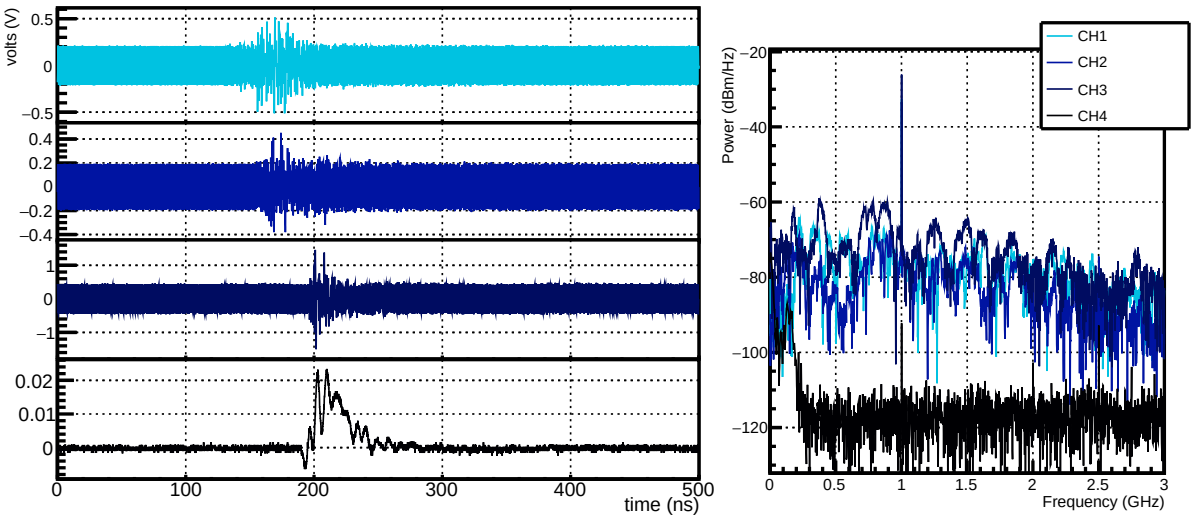

Figure 5.5: A typical T576 event. The 4 left panels are channels 1-4 from top to bottom, respectively, and the right panel shows their associated PSD. The offsets on the x-axis are due to air and cable propagation delays.

itself, with natural nulls at certain antennas for certain frequencies, as observed during the foil tests. The carrier is evident in the PSD.

Though the beam splash is large, it is exceedingly stable, which will later be extremely important to the background subtraction procedure. The shot-to-shot variation depends on the amount of charge in the bunch, as seen in Figure 5.6, where the energy in the beam splash scales with the beam charge measured by the ICT. This is useful for building up a background 'template' and for constructing 'null' data, to train the analysis techniques. Previous experiments [113] have made measurements of transition radiation which show a quadratic scaling of TR energy with beam charge, indicating coherence. The electron number N_e only varied by roughly 20% during our run, but our fit in log-log space has a slope roughly halfway between the expectation for complete incoherence (slope=1, corresponding to the green line in Figure 5.6) and complete coherence (slope=2, corresponding to the red line). Interestingly, as the receiver is moved relative to the shower, the coherent contribution of the beam splash increases, albeit only slightly. To improve our signal sensitivity, the data at this point are up-sampled by a factor of 5 and then filtered at $\pm$300 MHz from the carrier using a time-domain software bandpass filter.

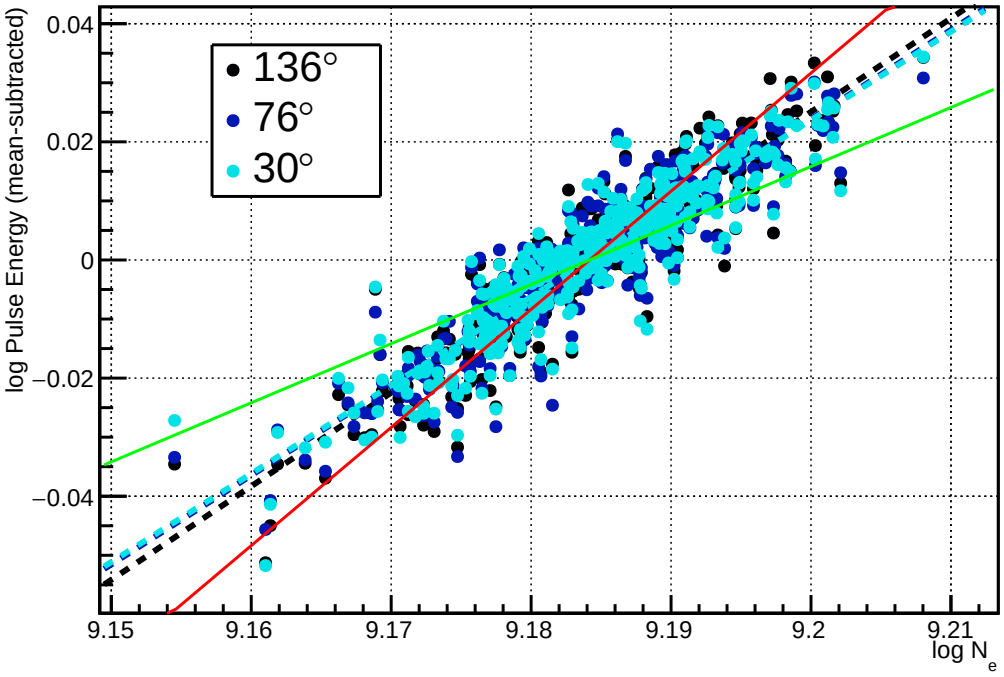

Figure 5.6: The ICT-measured electron number per bunch versus pulse energy, as measured by the antennas indicated by their angle from the beam momentum direction. The mean has been subtracted from all distributions in order to highlight the trend. Total coherence would correspond to a slope of 2 (red line), incoherence to a slope of 1 (green line).

5.5.3 'Null' Data

To train the background-subtraction procedure, we developed a routine for building up what will be called 'null' data, which are devoid of signal. These consist of carrier-only (beam OFF) data events added to beam splash-only (carrier OFF) data events, and constructed as follows:

1. A real event is selected from the data file.

2. A carrier-only event (beam OFF, carrier ON) is selected from a carrier-only file with the same frequency and output power settings. It is matched to the real event in both amplitude (via scaling) and phase (via cross correlation with the first 100 ns of the real event).

3. A template of beam-only events is produced by averaging over a beam-only run of 90 events. This template is then scaled using the measured value from the ICT and aligned, in time, with the real event via cross correlation, windowed around the beam onset.

4. Now that the carrier-only event is aligned with the real carrier in the pre-signal region, and the beam-only event is aligned with the real beam splash in the signal region, the carrier-only and beam-only events are summed together to produce a 'null' event, which contains no signal.

An example of this procedure is shown in Figure 5.7. Indicated in the Figure are the carrier-only (TX ON/Beam OFF) and beam-only (TX OFF/Beam ON) events used to make the null event, along with the real event and the resultant null event. This method of construction of the null data is important because the phase relationship between the carrier and the beam splash changes from shot-to-shot, so any analysis technique needs to treat this variation carefully. It is essential that our null data set has identical carrier/beam phase relationships as the real data. Many techniques for background reduction, such as simple averaging, will fail in this case, due to the lack of fixed phase in the carrier. Similarly, monitoring for power scaling at the signal region is not possible, as sometimes the carrier and beam splash add constructively, and sometimes destructively.

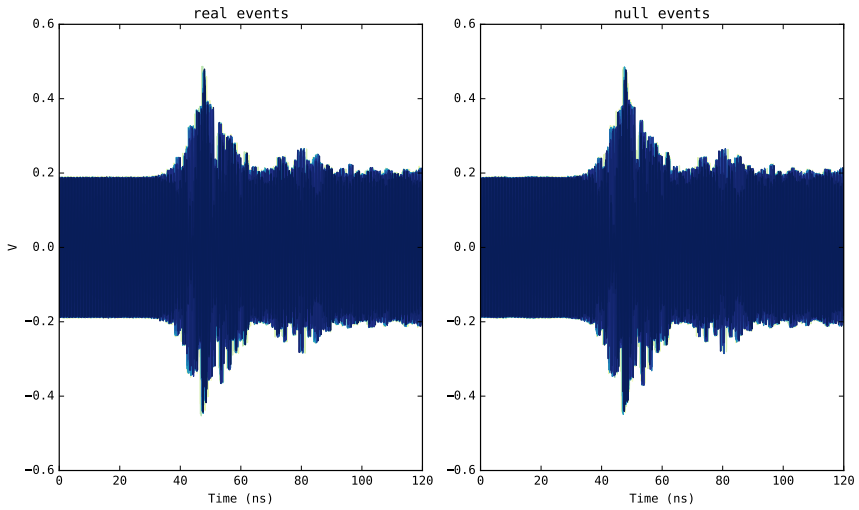

Figure 5.7: An example of 'null' data construction. A carrier-only (TX ON / Beam OFF) event is phase aligned with the carrier of a real event, and a beam-only (TX OFF/ Beam ON) event is phase aligned with the beam splash of a real event. The two are summed to produce an event which mimics real events in phase and amplitude.

In what follows, every analysis step was carried out concurrently on two sets of data: real and null. The lack of a signal appearing in the null data gives confidence that any signal observed in the real data is not an artifact of our signal-extraction procedure.

5.5.4 Overview of Analysis Techniques

Figure 5.8 shows the full data set for this analysis (e.g. all events from the cleanest run) as well as the associated null set. The analysis methods employed are based closely on [111], with necessary modifications specific to T576; we will use the vocabulary of that reference here. The procedure resembles pattern-matching routines for signal processing such as the Karhunen-Loeve technique, and is particularly suited to low-SNR data. It primarily involves decomposition of data into a basis of *patterns*, which are orthogonal modes (analogous to Fourier modes) that describe the data. The power of the process, built on singular value decomposition (SVD), is that instead of pre-defined modes, as in Fourier or wavelet decomposition, the SVD method finds an orthogonal basis within the data itself to describe the data. This basis of patterns, or 'eigenpatterns', or 'modes' (these terms will be used interchangeably) is ordered in significance by corresponding singular values,

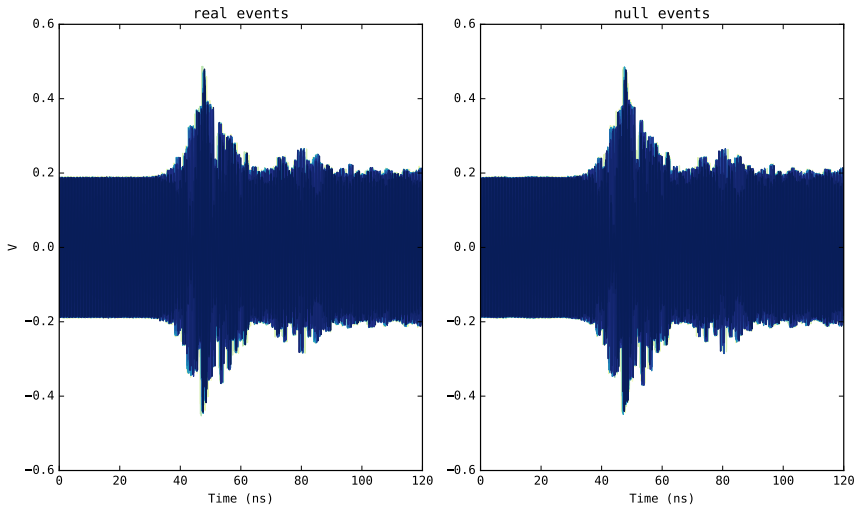

Figure 5.8: The data sets used in this analysis. Left: Real data from the run. Right: Null data produced via the procedure described in the text.

or eigenvalues (i.e., weights). The relative scale of the weight is a measure of how well the data are described by that corresponding pattern. For T576, we expect that the beam background will occupy the most significant patterns in the decomposition, and by removing these, we can then reconstruct the reflected signal event, evident as less significant patterns in the decomposition.

Following [111], we use the following terminology:

1. A *vector V* is synonymous with an event captured by the DAQ.

2. A *pattern* is a basis mode from the decomposition, or an eigenvector, weighted by its associated eigenvalue.

3. A *filter f* is a combination of one or more patterns which can be used to isolate, and, if desired, subtract components of the data. It can be thought of as a weighted sum over normal modes (again, the analogy to Fourier modes is useful here, in that a signal is built up of a sum of weighted normal modes).

The Single-Valued Decomposition is symbolically defined as:

$$M = u\Lambda v*, \tag{5.1}$$

where M is a matrix to be decomposed, and u and v are matrices containing the singular vectors of M. These are the patterns which describe the data in M, and are ordered by the matrix Λ, which has the singular values along its main diagonal. The singular values are the weights of the corresponding patterns in u and v.

5.5.5 Carrier subtraction

Careful removal of the carrier from the T576 data is useful in isolating the signal. Removal of the carrier via successive sine-subtract filtration [115] is possible, but not problem-free. First, fitting a sine wave is susceptible to fitting errors; small errors in the subtraction can mean incomplete removal of an enormous background. Fits can be improved with pre-filtering the data, but this costs information content. Second, the amplitude of the carrier in sine-subtraction must be fixed to one value. If not, the amplitude envelope must also be extracted by a fit to data, for which the amplitude may vary. Third, the presence of harmonics requires further fitting and subtraction, each potentially removing too much or too little information, and possibly introducing artifacts.

Using decomposition to remove the carrier solves these problems, if, for example, the modulations in amplitude are periodic or in any way repetitive, and the harmonics are stable. This is because the decomposition will yield the most significant mode of the data, which is not necessarily a Fourier mode, and may be some complicated (but correlated, e.g. from the same source) structure. It can then be removed in whole or in part by the filtration method described below.

Because a carrier naturally has some periodicity, it is useful to break the data up into bins, to see if there exists an optimal binning for background-subtraction. To find such a binning, we can use a decomposition. First we construct a vector V out of the *pre-signal* region and partition it into bins of length D, then we build a matrix out of these chunks, with each chunk corresponding to a row in this matrix.

$$M_{ij} = V_{(i*D+j)} \tag{5.2}$$

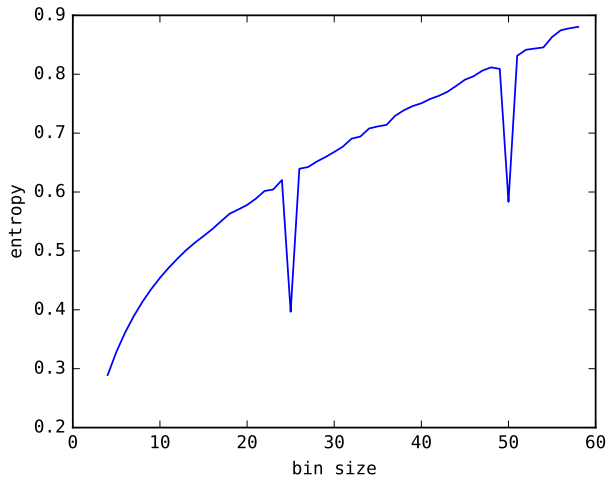

Figure 5.9: The Von Neumann entropy as a function of the bin size D, as described in the text.

If the vector has length N, such that there are $d = N/D$ chunks in V, then the matrix M has dimensions $d \times D$. We can then perform SVD on this matrix and examine the 'orderliness' of the singular values Λ as a function of the bin size D. This orderliness can be quantified by calculating the Von Neumann entropy $S = -\sum_{ij} \Lambda_{ij} \log(\Lambda_{ij})$ for the singular values in Λ and plotting that quantity against the bin size. If there are no significant patterns (e.g. if the vector is uncorrelated noise) the entropy will exhibit the standard logarithmic dependence, and vary as $\log(D)$. A downward excursion from the $\log(D)$ curve indicates that the data is more orderly with that binning. Figure 5.9 shows such a plot for this analysis. As evident in the Figure, the values are all well below $\log(D)$, with a strong downgoing excursion at $D = 25$, indicating an optimal binning for this run.

When we subsequently bin with $D = 25$, the resultant distribution of singular values indicates that the carrier can be described fully by a small number of modes n. We can then zero out the remainder of the singular values,

$$\Lambda'_{ij} = \Lambda_{ij}\Theta(n-i), \tag{5.3}$$

and reconstruct the matrix M' by reversing the SVD, using the truncated matrix of singular values Λ'. The indices of the new matrix can then be flattened to recover a filter $f_{carrier}$ which can then

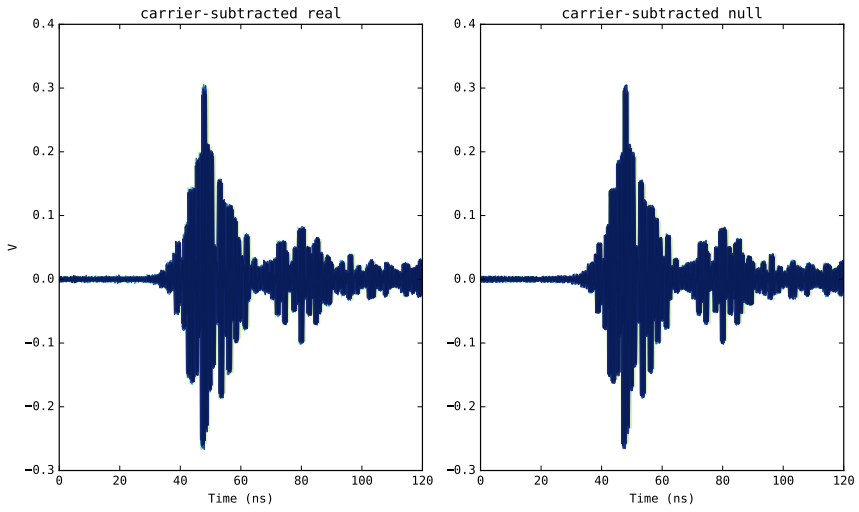

Figure 5.10: The data sets with the carrier removed through the process described in the text. Left: Real data. Right: Null data.

be subtracted from the signal region of the same event. The results of this filtration are shown in Figure 5.10 for both real and null data, in which the $\sim$200 mV carrier has been reduced to the level of noise by this procedure. The carrier removal was performed on each event individually using the above procedure.

5.5.6 Alignment of the Sets

At this point we have two carrier subtracted sets, real and null, although some trigger-point jitter from the experiment still remains. We therefore subsequently align all of the events in both the real and null data sets, to the same, single reference event (selected arbitrarily, and subsequently discarded from the analysis) via a cross-correlation routine. The aligned, carrier-subtracted waveforms (all overlaid) are shown in Figure 5.11, zoomed slightly to better illustrate the quality of the alignment.

5.5.7 Extraction of the Signal

Now that we have carrier-removed and aligned waveforms, we perform decomposition of the remaining waveforms, removing the most prominent modes, corresponding to the beam splash, and

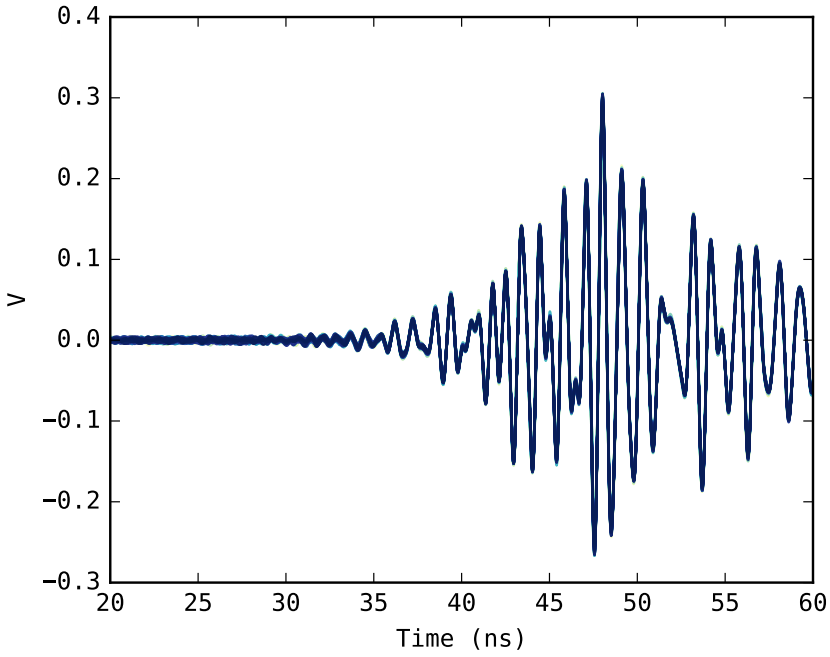

Figure 5.11: Carrier-removed data aligned via cross-correlation. All events from both real and null sets are overlaid (∼180 events).

the least prominent modes, corresponding to uncorrelated noise, and then, finally, performing a careful average on what remains to accentuate any possible signal.

We first build up two matrices, M^R and M^F for real and null data respectively, which have the following structure:

$$M_{ki} = V_i^k. \tag{5.4}$$

Here k is a label for identifying the event (e.g. $k = 1,2...N$ for N events) and i is the index of the data within V^k. Therefore, M is a matrix in which each row is an event. We next make a decomposition of each matrix, which will simultaneously decompose all events into a basis for each full set, real and null. We then examine the normalized distribution of singular values Λ_α, equivalent to the diagonal vector of the singular values within the matrix Λ. As shown in Figure 5.12, where we have plotted $\sqrt{\Lambda_\alpha}$ to emphasize the shape of the curve, the two sets follow the same trend (the distribution is truncated above n=30 for readability).

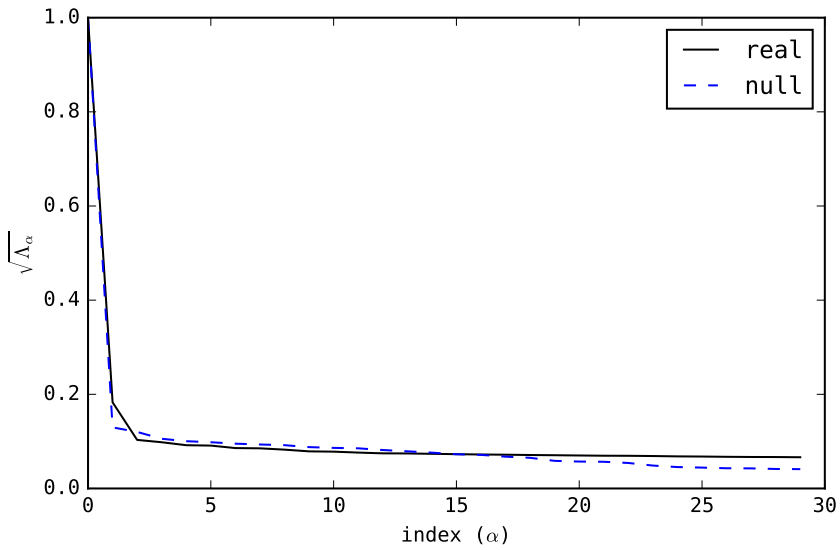

Figure 5.12: The normalized distributions of singular values for real and null sets after decomposition.

We now present the results of this analysis. The time-versus-frequency plots (spectrograms) that follow have units of power in V^2Hz^{-1}. The colorbar scale is the same for real and null, and varies from plot-pair to plot-pair.

By inspection (via comparison to the original waveforms), it is evident that the beam splash, as expected, corresponds to the first singular values in both real and null sets. This is shown in Figure 5.13, for which we plot the average spectrogram of all events in the set, real and null, after reversing the decomposition, but prior to removal of any patterns (hence $M^{R\prime} = M^R$, $M^{F\prime} = M^F$). This is useful as a reference in what follows. We then truncate the singular values in the opposite way as before, that is, we zero the most significant singular values, (and also remove the n>40 modes to further suppress noise) and then reverse the decomposition to recover the filtered events. Finally, we construct a power spectrogram of each event, and, finally average the spectrograms. The result of this procedure is shown in Figure 5.14, in which we observe a clear difference in the time-spectral content between the real and null sets. There is a clear scaling at the time when the reflected radar signal is expected (roughly 42-45 ns into the trace as pictured) in the real set, but not in the null set. Moreover, if we selectively examine each pattern and reverse the decomposition for each one singularly, in no case do we observe scaling at the signal onset point in the null data

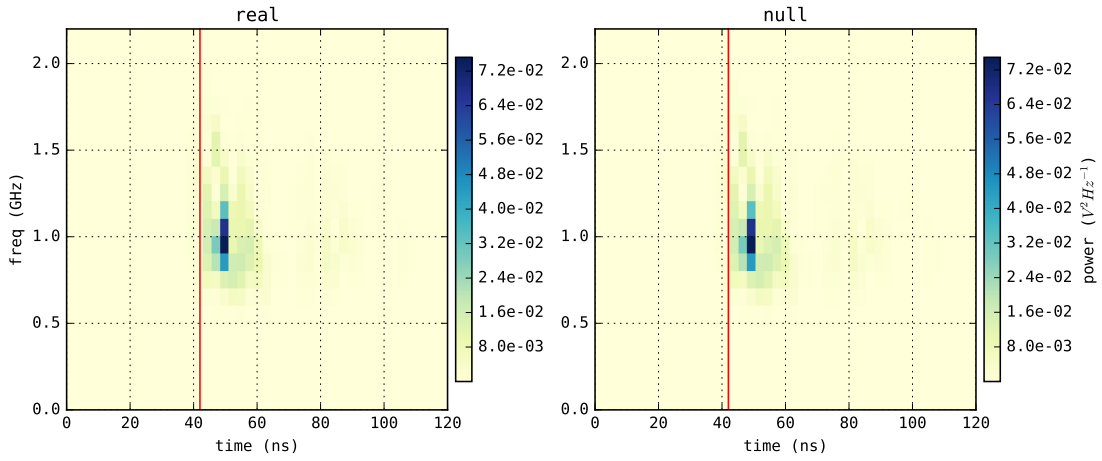

Figure 5.13: The average of all events, real and null, after reversing the decomposition, without removing any patterns. The solid vertical line indicates the approximate expected signal onset point, in time.

(excepting, of course, the first two beam splash patterns).

The scaling in the signal region, which is only observed in the real data, is a suggestive hint of a signal. Of particular interest is the timing of the signal onset. It is clear by comparing Figures 5.13 and 5.14 that the peak strength of the scaling in the signal region of the filtered data occurs before the peak strength of the beam splash in the unfiltered data. Calculations (based on cable delays and the known time of beam-on-target) similarly predict arrival of the reflection, in the receivers, 5-10 ns before the peak of the beam splash.

Figure 5.15 shows a comparison of the real data to simulated signal, which has been produced using the RadioScatter code [103] using the exact specifications of this run and a plasma lifetime of 10 ns. The agreement is quite good, with the difference in power between data and simulation less than 10% and a very similar spectrogram shape. We note that we have not yet fully incorporated the full system response into the analysis chain; this is currently in progress. Accounting for cable losses (small, given the modest cable runs) and antenna inefficiencies are expected to reduce the signal power in the simulation by a few percent. Consistent with the noisy environment, the data trace is somewhat 'messier' than the simulation. A more careful selection of patterns, e.g.

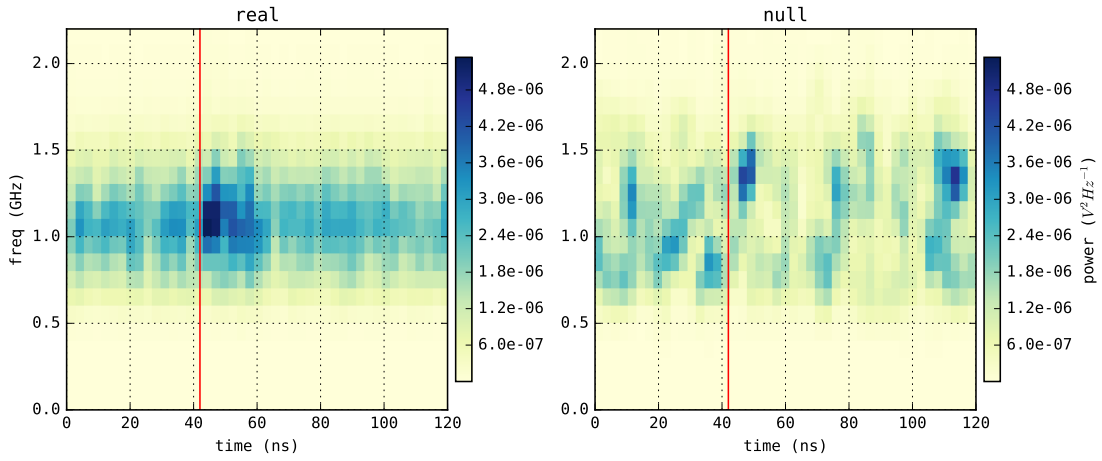

Figure 5.14: The average of all events, real and null, after reversing the decomposition and removing the most significant patterns, which correspond to the beam splash. The solid vertical line indicates the approximate signal onset point.

eliminating some of the less significant noise modes, would likely clean up this background a bit. Although a full analysis of the noise modes has not yet been performed, we present an example noise mode (representative of all modes above n=10 or so) in Figure 5.16.

We follow the same procedure outlined above for data taken when the output power of the transmitter was reduced from ∼25 W to a nominal value of ∼5 W. For the latter data, the power of the carrier in the pre-signal region was actually observed to be smaller by a factor of 3.6 rather than 5 The resultant summed spectrogram is shown in Figure 5.17, where there is a suggestion of scaling in both signal regions commensurate with the different outputs, although we observe only a factor of ∼1.5 difference between the peak power in these two spectrograms rather than the factor of 3.6 cited above. Nevertheless, the shape of the signal is similar and the time onset identical to within one bin. Simulations predict that this configuration should produce radar reflections with an SNR of about two, in fair agreement with the data.

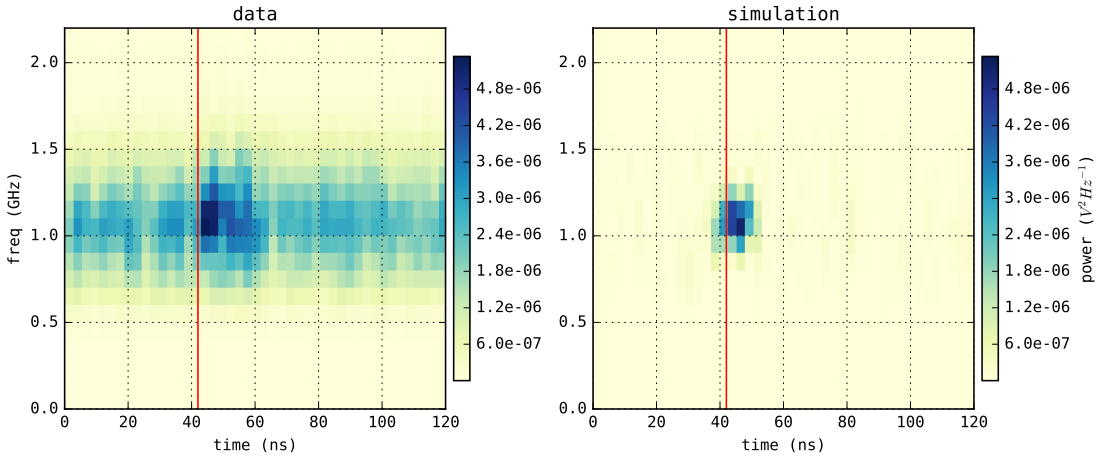

Figure 5.15: A comparison of the resultant filtered data to the RadioScatter simulation, for the same geometry and transmitter settings as the real run, with a plasma lifetime of 10 ns. The solid vertical line indicates the approximate signal onset point.

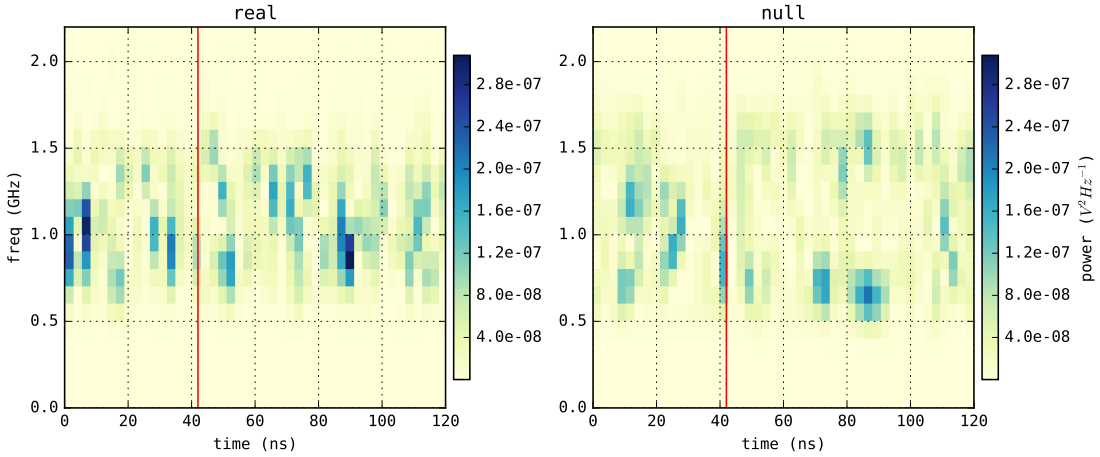

Figure 5.16: An example of an higher-order mode with singular value $n = 15$. The solid vertical line indicates the approximate signal onset point.

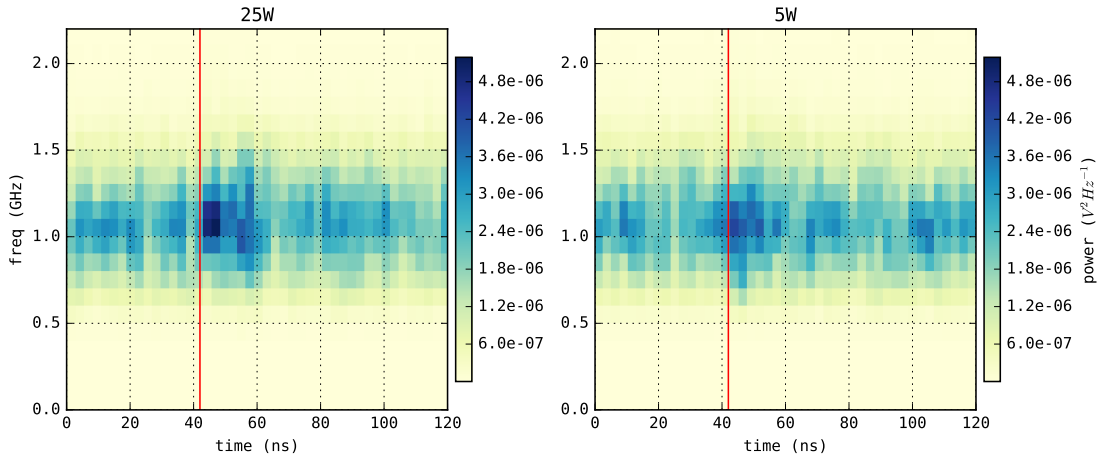

Figure 5.17: The average of all events, for 25 W output and 5 W output, after reversing the decomposition and removing the most significant patterns. The solid vertical line indicates the approximate signal onset point.

5.6 Significance

We now present a quantitative assessment of the significance of the signal hint presented here, based on our analysis of the real and null data sets. To assign a significance to the observed excess, we employ a 2-d sideband subtraction technique, shown diagrammatically in Figure 5.18. The adjacent sidebands in x and y are averaged and subtracted from the signal region. This ensures that the apparent excess in the signal region is not simply a sum of the backgrounds from any residual beam splash plus carrier, at the point where they cross in the signal region.

Mathematically,

$$< x >= \frac{\int x_1 dA + \int x_2 dA}{2}, \tag{5.5}$$

where dA indicates integration over the bounded area of the associated label, and similarly,

$$< y >= \frac{\int y_1 dA + \int y_2 dA}{2}, \tag{5.6}$$

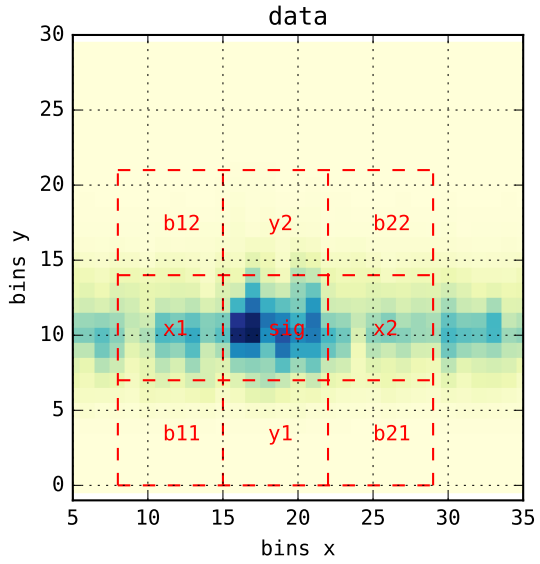

Figure 5.18: The sideband subtraction method. Regions with similar labels (x, y, b) are integrated, and these integrals are averaged, then subtracted from the signal region.

and

$$< b >= \frac{\int b_{11} dA + \int b_{12} dA + \int b_{21} dA + \int b_{22} dA}{4}. \tag{5.7}$$

The regions 'b' are selected as 'ambient' background, or an overall level which sits below the beam splash remnant ('y') and the carrier-subtraction remnant ('x') such that e.g. the carrier remnant is $< x > - < b >$. The signal-region excess η is then,

$$\eta = \int sdA - (< x > - < b >) - (< y > - < b >) - < b > \tag{5.8}$$

$$= \int sdA - < x > - < y > + < b > . \tag{5.9}$$

We justify this procedure as follows: if the beam splash is sufficiently broadband, as it seems to be, then the amplitude of the remainder of the beam splash in the signal region (whatever has not been fully removed by the SVD method) will be well approximated by an average of the regions

co-located in time, but with frequencies above and below the signal region. Similarly, along the time axis, the remnant of the carrier (leftover from subtraction) should not prefer any particular region, therefore the average of the regions before and after the signal region should approximate the remainder of the carrier within the signal region. These backgrounds are then subtracted from the signal region. Because both of these backgrounds ($< x >$ and $< y >$) also contain an overall ambient background ($< b >$), we must add this background back in to avoid over-subtraction, as in eq. 5.8.

We perform a sideband subtraction for each event in both the data and background sets, and plot the result in Figure 5.19, where the x-axis is presented in units of the standard deviation of the background distribution σ_{null}. There is a clear excess in the integrated power η for the signal events. The mean of the real data sideband-subtracted distribution is $2.36\sigma_{null}$ from the mean of the null distribution, at -.$28\sigma_{null}$. By inspection, some of the events in the real data distribution are consistent with the null data, while some show a significance greater than $5\sigma_{null}$. For the purposes of this analysis, we use the mean of the real data excess distribution to estimate a significance of $2.36\sigma_{null}$.

The process of performing the same analysis on the real and null sets eliminates analysis systematics, which would be present in both. Therefore, the main systematic is in the construction of the null data.

5.7 Discussion and Next Steps

The results presented here, based on analysis of the receiver at the specular reflection point, comprise the majority of the usable data from the experiment, given the challenges outlined above. The signal significance of 2.36σ is large enough to warrant further investigation. At the time of this writing, a further beam test is scheduled for fall, 2018, with several planned improvements.

In considering how this next run might improve on the results presented herein, the main challenge is clearly mitigation of the background from beam splash. While some amount of RF from

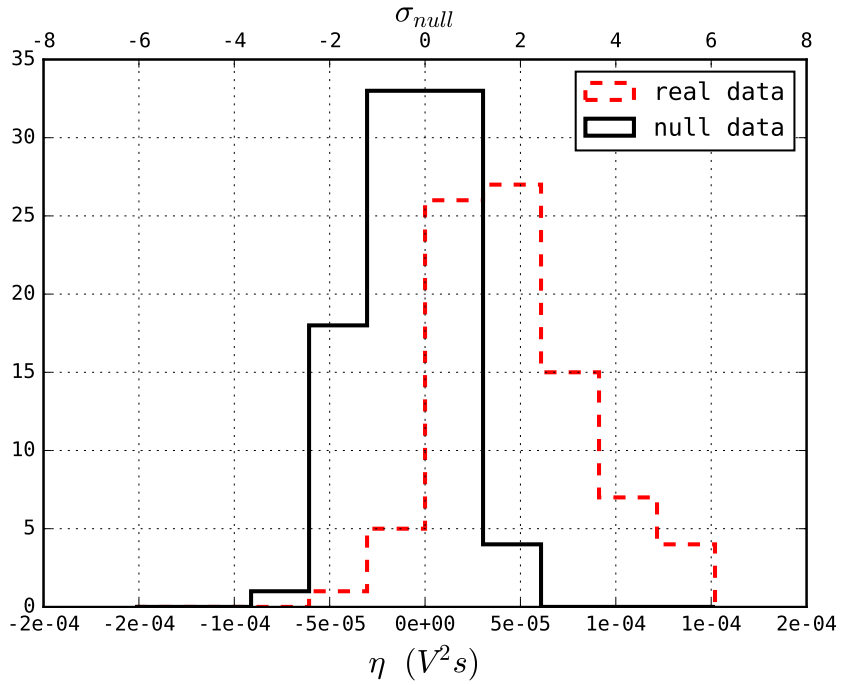

Figure 5.19: The significance of the signal using the 2D sideband subtraction routine. X axis units are given in $V^2 s$ and also in terms of standard deviations of the null data distribution, denoted σ_{null}.

the shower was expected[113], we had not anticipated such a high amplitude signal. As this is a discovery experiment, we were disinclined towards heavily filtering, so as to retain as much information as possible. However, in so doing, the large amplitude of the beam splash required a zoomed-out scope amplitude setting, resulting in only very coarse resolution given our 8-bit scope digitizer. Trigger point slewing and averaging can compensate to some degree, but, for the future, either a higher resolution DAQ or one of several known techniques to increase the digitization resolution of the data would be useful. Additionally, the most important hardware upgrade would be use of a more powerful transmitter. The simplest way to deal with the beam splash and also increase the resolution of the putative signal is simply to amplify the transmitter by another factor of 2-10, such that the reflection is well above noise after background subtraction. Noting that he beam splash amplitudes begin to fall off drastically above 1.5 GHz, we will also employ a power amplifier which has a higher frequency band of operation. Additionally, an option to run using a signal generator which is phase-locked to the beam arrival would be useful from an analysis stand-

point. Finally, another improvement over this run will be better (or rather more well-characterized) antennas, with added directionality. This will effectively increase our transmitter power in the direction of the shower, increasing SNR.

The main 'smoking gun' signals we will look for during the next run are:

- a $R_1^{-2}R_2^{-2}$ dependence on the putative signal in the real data, where R_1 is the transmitter-shower baseline and R_2 is the shower-receiver baseline,
- a scaling of the return signal duration as a function of frequency,
- a frequency shift of the return signal at receivers displaced from the specular point, and
- a scaling of the return signal as a function of azimuth, with signal amplitude trending differently than the pure carrier amplitude.

These measurements may be difficult given the restrictions of hardware and the space, but will be central to the experimental program for run 2, now that we believe our backgrounds and primary experimental challenges are well-known.

Chapter 6

Conclusion

In this dissertation we have presented a discussion on radar-based detection techniques for cosmic ray and neutrino induced cascades. We first discussed (briefly, and with much abridgment) the history of cosmic ray and neutrino discovery, which is full of insightful theory and ambitious experimentation. We then went through the theory of radar techniques in physics, building up to contemporary models of neutrino cascade detection by discussing meteor scatter and EAS detection with TARA. We then presented the contemporary models, including macroscopic and microscopic treatments of the radar problem. Finally, we presented the first analysis of data from the SLAC T576 experiment, which suggests that the technique requires further exploration, and may yet be a robust detection technology for $\mathcal{O}$(PeV) and greater neutrinos. Here we will briefly summarize these chapters, and draw some final conclusions from them.

In chapter 2 we discussed the history of the radar problem, beginning with a discussion of radar in general, and ending with a contemporary model for neutrino induced cascade detection in ice. This model by de Vries et.al. [90] is the most comprehensive macroscopic model to date for the radar problem, and suggests that the technique is a promising detection technology for the energy region just out of reach of IceCube, and just below the main sensitivity of Askaryan type detectors. The model presented in chapter 4 of this dissertation is a particle-level model describing the same phenomenon. It is the only such model in existence, and the only one (that the author is aware

of) which treats the radar problem from within a monte-carlo program on a particle-level basis. The many advantages of such a model have been presented, the most significant of which is the lack of dependence upon a model of the shower distribution. By harnessing the power of a monte carlo such as GEANT4, the assumptions about shower development, and the associated simulation systematics, are removed. This model has been incorporated into a module called RadioScatter, written in c++, which is open source (https://github.com/prchyr/RadioScatter) and can be used in any program which supplies the 4-vectors of shower particles for a given shower. This simulation agrees well with the model by de Vries et. al. in terms of sensitivity, and a detailed comparison of the methods is forthcoming. The primary conclusion from the discussion of models presented here is that the sensitivity at 10^{15-17}eV is, if validated, the best among all available technologies currently under development, which is reason alone to warrant further investigation of the method.

In chapter 3 we presented a firmware-based trigger for the chirp-like signals expected from UHECR radar reflections. This trigger achieves in-field sensitivity at an SNR<1, with full efficiency below an SNR of 2, making it a tremendously robust detector for chirp-like signals. While the first deployment of this trigger system as part of the TARA experiment yielded no direct coincident events with the Telescope Array, a forthcoming, more detailed analysis of the data may be able to set a less model-dependent limit on the UHECR radar detection problem than the limit published by the TARA collaboration [60]. At the very least, such an analysis will fully elucidate the sensitivity and capabilities of such a trigger, for potential future use in a neutrino cascade detection experiment, or possible future Askaryan experiments, wherever a chirp-like signal is expected.

Finally, in chapter 5 we presented the first results from the T576 experiment, measuring radar reflections from an electron-beam induced cascade in a plastic target at SLAC. This experiment, first performed in May 2018 with an imminent second run scheduled for October 2018, observed an excess in the signal region with a 2.36σ significance above simulated 'fake' data, using an eigendecomposition method. This significance is conservative. The distribution of the excess in the signal region has many events which rise above a 5σ signal significance. We choose to conservatively quote the significance of the mean of this distribution, to account for possible systematics in the

relatively new and advanced analysis technique employed here. We believe that this significance is enough to warrant further investigation of the method, which will occur within the coming months at SLAC. When coupled with the model predictions and relatively low cost required to implement a radar based system, these results suggest a viable path forward for 10^{15-17}eV neutrino detection. We present this conclusion in the context of exciting developments in the radio astroparticle community at large, making the case for radar as a promising neutrino detection technology.

References

[1] IceCube, Science **361**, 147 (2018).

[2] V. F. Hess, Phys. Z. **13**, 1084 (1912).

[3] J. G. Anderson, Transactions of the Faculty of Actuaries **17**, 219–221 (1945).

[4] W. C. Röntgen, Nature **53**, 274 (1896).

[5] T. Huege and D. Besson, PTEP **2017**, 12A106 (2017), 1701.02987.

[6] A. M. Hillas, J. Phys. **G31**, R95 (2005).

[7] K. Greisen, Phys. Rev. Lett. **16**, 748 (1966).

[8] G. T. Zatsepin and V. A. Kuzmin, JETP Lett. **4**, 78 (1966), [Pisma Zh. Eksp. Teor. Fiz.4,114(1966)].

[9] HiRes, R. U. Abbasi *et al.*, Phys. Rev. Lett. **100**, 101101 (2008), astro-ph/0703099.

[10] Pierre Auger, J. Abraham *et al.*, Phys. Lett. **B685**, 239 (2010), 1002.1975.

[11] F. Close, *Neutrino* (Oxford, 2010).

[12] F. L. Wilson, Am. J. Phys. **36**, 1150 (1968).

[13] C. L. Cowan, F. Reines, F. B. Harrison, H. W. Kruse, and A. D. McGuire, Science **124**, 103 (1956), http://science.sciencemag.org/content/124/3212/103.full.pdf.

[14] Particle Data Group, C. Patrignani *et al.*, Chin. Phys. **C40**, 100001 (2016).

[15] D. W. McKay and J. P. Ralston, Phys. Lett. **167B**, 103 (1986).

[16] IceCube, M. G. Aartsen *et al.*, Nature **551**, 596 (2017), 1711.08119.

[17] M. Bustamante and A. Connolly, (2017), 1711.11043.

[18] A. Connolly, R. S. Thorne, and D. Waters, Phys. Rev. **D83**, 113009 (2011), 1102.0691.

[19] IceCube, M. G. Aartsen *et al.*, Science **342**, 1242856 (2013), 1311.5238.

[20] P. A. Čerenkov, Physical Review **52**, 378–379 (1937).

[21] N. Jelley, A. B. McDonald, and R. H. Robertson, Annual Review of Nuclear and Particle Science **59**, 431 (2009).

[22] Super-Kamiokande, Y. Fukuda *et al.*, Nucl. Instrum. Meth. **A501**, 418 (2003).

[23] K. Abe *et al.*, (2011), 1109.3262.

[24] P. Auger, Review of Modern Physics **11**, 288 (1939).

[25] N. Chiba *et al.*, Nucl. Instrum. Meth. **A311**, 338 (1992).

[26] HAWC, T. DeYoung, Nucl. Instrum. Meth. **A692**, 72 (2012).

[27] H. Kawai *et al.*, Nuclear Physics B **175-176**, 221 (2008).

[28] T. A. Collaboration, Fermilab **96/024** (1996).

[29] Telescope Array, T. Abu-Zayyad *et al.*, Nucl. Instrum. Meth. **A689**, 87 (2013), 1201.4964.

[30] Telescope Array, E. Kido, PoS **ICHEP2016**, 1203 (2017).

[31] R. M. Baltrusaitis *et al.*, Nucl. Instrum. Meth. **A240**, 410 (1985).

[32] T. Abu-Zayyad *et al.*, Nucl. Instrum. Meth. **A450**, 253 (2000).

[33] MAGIC, E. Lorenz, New Astron. Rev. **48**, 339 (2004).

[34] VERITAS, J. Holder *et al.*, Astropart. Phys. **25**, 391 (2006), astro-ph/0604119.

[35] CTA Consortium, M. Actis *et al.*, Exper. Astron. **32**, 193 (2011), 1008.3703.

[36] M. A. Markov and I. M. Zheleznykh, Nucl. Instrum. Meth. **A248**, 242 (1986).

[37] AMANDA, F. Halzen *et al.*, Nucl. Phys. Proc. Suppl. **77**, 474 (1999), hep-ex/9809025, [,474(1998)].

[38] ANTARES, M. Ageron *et al.*, Nucl. Instrum. Meth. **A656**, 11 (2011), 1104.1607.

[39] KM3NeT, A. Margiotta, Nucl. Instrum. Meth. **A766**, 83 (2014), 1408.1392.

[40] IceCube, M. G. Aartsen *et al.*, Phys. Rev. Lett. **113**, 101101 (2014), 1405.5303.

[41] LOFAR, G. Heald *et al.*, J. Astrophys. Astron. **32**, 589 (2011), 1106.3195.

[42] LOPES, T. Huege *et al.*, Nucl. Instrum. Meth. **A662**, S72 (2012), 1009.0345.

[43] Pierre Auger, B. Fuchs, Nucl. Instrum. Meth. **A692**, 93 (2012).

[44] G. A. Askar'yan, Sov. Phys. JETP **14**, 441 (1962), [Zh. Eksp. Teor. Fiz.41,616(1961)].

[45] E. Zas, F. Halzen, and T. Stanev, Phys. Rev. **D45**, 362 (1992).

[46] G. M. Frichter, J. P. Ralston, and D. W. McKay, Phys. Rev. **D53**, 1684 (1996), astro-ph/9507078.

[47] D. Saltzberg *et al.*, Phys. Rev. Lett. **86**, 2802 (2001), hep-ex/0011001.

[48] I. Kravchenko *et al.*, Phys. Rev. **D73**, 082002 (2006), astro-ph/0601148.

[49] P. Allison *et al.*, Astropart. Phys. **35**, 457 (2012), 1105.2854.

[50] S. Klein *et al.*, IEEE Transactions on Nuclear Science **60**, 637 (2013).

[51] ANITA, P. W. Gorham *et al.*, Astropart. Phys. **32**, 10 (2009), 0812.1920.

[52] T-510, K. Belov *et al.*, Phys. Rev. Lett. **116**, 141103 (2016), 1507.07296.

[53] ANITA, P. W. Gorham *et al.*, (2018), 1803.05088.

[54] P. Schellart *et al.*, Phys. Rev. Lett. **114**, 165001 (2015), 1504.05742.

[55] ANITA, P. W. Gorham *et al.*, Phys. Rev. Lett. **99**, 171101 (2007), hep-ex/0611008.

[56] K. D. de Vries *et al.*, Astropart. Phys. **74**, 96 (2016), 1503.02808.

[57] P. Motloch, J. Alvarez-Muñiz, P. Privitera, and E. Zas, Phys. Rev. **D93**, 043010 (2016), 1509.01584, [Addendum: Phys. Rev.D94,no.4,049905(2016)].

[58] P. Blackett and C. Lovell, Proc. Roy. Soc A **177**, 183 (1941).

[59] R. Abbasi *et al.*, Nucl. Instrum. Meth. **A767**, 322 (2014), 1405.0057.

[60] R. U. Abbasi *et al.*, Astropart. Phys. **87**, 1 (2017), 1603.05217.

[61] P. Gorham, Astropart. Phys. **15**, 177 (2001), hep-ex/0001041.

[62] M. Chiba *et al.*, SUSY07 (2007).

[63] K. de Vries, A. Ó Murchadha, K. Hanson, and T. Meures, Proceedings of The 34th International Cosmic Ray Conference — PoS(ICRC2015) **236**, 1168 (2016).

[64] K. DeVries *et al.*, Proceedings of Science **(ICRC2017)**, 1049 (2017).

[65] S. Kunwar *et al.*, Nucl. Instrum. Meth. **A797**, 110 (2015), 1504.00779.

[66] S. Prohira, S. Kunwar, K. Ratzlaff, R. Young, and D. Besson, Nucl. Instrum. Meth. **A890**, 126 (2018), 1709.08587.

[67] Y. Raizer, *Gas Discharge Physics* (Springer, 1991).

[68] E. V. Appleton, R. Naismith, and I. L. J., Philosophical Transactions of the Royal Society of London A: Mathematical, Physical and Engineering Sciences **236**, 191 (1937), http://rsta.royalsocietypublishing.org/content/236/764/191.full.pdf.

[69] R. A. W. Watt, L. H. Bainbridge-Bell, A. F. Wilkins, and E. G. Bowen, Nature **137**, 866–866 (1936).

[70] R. C. Colwell and A. W. Friend, Nature **137**, 782–782 (1936).

[71] R. C. Colwell and A. W. Friend, Phys. Rev. **50**, 632 (1936).

[72] D. McKinley, *Meteor Science and Engineering* (McGraw-Hill, 1961).

[73] J. Crispin and A. Maffett, Proceedings of the IEEE **53**, 833 (1965).

[74] J. H. Van Vleck, F. Bloch, and M. Hamermesh, Journal of Applied Physics **18**, 274 (1947).

[75] T. Terasawa *et al.*, Proceedings of the 31st International Cosmic ray Conference (2009).

[76] J. Stasielak *et al.*, Astroparticle Physics **73**, 14 (2016).

[77] S. Nijdam, G. Wormeester, E. Van Veldhuizen, and U. Ebert, Journal of Physics D: Applied Physics **44**, 455201 (2011).

[78] M. Chiba *et al.*, AIP Conference Proceedings **1535**, 45 (2013).

[79] S. Close, M. Oppenheim, S. Hunt, and A. Coster, Icarus **168**, 43 (2004).

[80] L. Dyrud *et al.*, Earth Moon and Planets **102**, 383 (2008).

[81] S. Close, M. Oppenheim, S. Hunt, and L. Dyrud, Journal of Geophysical Research: Space Physics **107**, SIA (2002).

[82] J. Kero *et al.*, Monthly Notices of the Royal Astronomical Society **416**, 2550 (2011).

[83] J. Forbes, N. Makarov, and Y. I. Portnyagin, Geophysical Research Letters **22**, 3247 (1995).

[84] M. I. Bakunov, A. V. Maslov, A. L. Novokovskaya, and A. Kryemadhi, Astropart. Phys. **33**, 335 (2010).

[85] H. Salzmann and K. Hirsch, Review of Scientific Instruments **55**, 457 (1984).

[86] P. W. Gorham *et al.*, J. Astron. Inst. **06**, 1740002 (2017), 1703.00415.

[87] S. Prohira *et al.*, ArXiv e-prints (2018), 1801.08909.

[88] M. P. De Haas, M. Kunst, J. M. Warman, and J. B. Verberne, The Journal of Physical Chemistry **87**, 4089 (1983), https://doi.org/10.1021/j100244a019.

[89] K. D. de Vries, K. Hanson, and T. Meures, Astropart. Phys. **60**, 25 (2015), 1312.4331.

[90] K. D. de Vries *et al.*, (2018), 1802.05543.

[91] K. Kamata and J. Nishimura, Progress of Theoretical Physics Supplement **6**, 93–155 (1958).

[92] L. D. Landau and I. I. Pomeranchuk, Dokl. Akad. Nauk SSSR **92**, 535 (1953).

[93] A. B. Migdal, Phys. Rev. **103**, 1811 (1956).

[94] J. Alvarez-Muniz and E. Zas, Phys. Lett. **B411**, 218 (1997), astro-ph/9706064.

[95] J. Alvarez-Muniz and E. Zas, Phys. Lett. **B434**, 396 (1998), astro-ph/9806098.

[96] Xilinx, Spartan 6 fpga, 2017.

[97] R. G. Lyons, *Understanding Digital Signal Processing* (Addison Wesley, 1997).

[98] M. Bakunov *et al.*, New Journ. Phys. **15**, 113027 (2013).

[99] S. Agostineli *et al.*, Nuclear Instruments and Methods in Physics Research A **506**, 250 (2003).

[100] M. Stockham, J. Macy, and D. Besson, Radio Science **51**, 194, https://agupubs.onlinelibrary.wiley.com/doi/pdf/10.1002/2015RS005849.

[101] J. Jackson, *Classical Electrodynamics*, 3 ed. (Wiley, 2000).

[102] D. R. Nicholson and D. R. Nicholson, *Introduction to plasma theory* (Wiley New York, 1983).

[103] S. Prohira, https://github.com/prchyr/RadioScatter (2017).

[104] K. DeVries, Private communication (2017).

[105] Y. Itikawa and N. Mason, Journal of Physical and Chemical Reference Data **34**, 1 (2005), https://doi.org/10.1063/1.1799251.

[106] RICE, I. Kravchenko *et al.*, Astropart. Phys. **19**, 15 (2003), astro-ph/0112372.

[107] S. Barwick, D. Besson, P. Gorham, and D. Saltzberg, J. Glaciol. **51**, 231 (2005).

[108] A. G. Vieregg, K. Bechtol, and A. Romero-Wolf, JCAP **1602**, 005 (2016), 1504.08006.

[109] T. Meures, *Development of a Sub-glacial Radio Telescope for the Detection of GZK Neutrinos*Springer Theses (Springer International Publishing, 2015).

[110] ARA, P. Allison *et al.*, Phys. Rev. **D93**, 082003 (2016), 1507.08991.

[111] A. Bean, J. P. Ralston, and J. Snow, Nucl. Instrum. Meth. **A596**, 172 (2008), 1008.0029.

[112] K. de Vries *et al.*, Proceedings of 35th International Cosmic Ray Conference — PoS(ICRC2017) **301**, 391 (2017).

[113] P. W. Gorham *et al.*, Phys. Rev. E **62**, 8590 (2000).

[114] P. Motloch, J. Alvarez-Muñiz, P. Privitera, and E. Zas, Phys. Rev. D **93**, 043010 (2016).

[115] ANITA, P. W. Gorham *et al.*, Phys. Rev. **D98**, 022001 (2018), 1803.02719.

[116] ANITA, S. Hoover *et al.*, Phys. Rev. Lett. **105**, 151101 (2010), 1005.0035.

[117] H. Schoorlemmer *et al.*, Astropart. Phys. **77**, 32 (2016), 1506.05396.

[118] D. Z. Besson *et al.*, Radio Science **50**, 1 (2015), 2013RS005315.

[119] A. Novikov *et al.*, J. Phys. Conf. Ser. **798**, 012217 (2017).

[120] P. Fretwell *et al.*, The Cryosphere **7**, 375 (2013).

Appendix A

The HiCal-2 Instrument

This chapter is adapted from a paper accepted by Nuclear Instrumentation and Methods in Physics-A:

HiCal 2: An Instrument Designed for Calibration of the ANITA Experiment and for Antarctic Surface Reflectivity Measurements

S. Prohira[e], A. Novikov[e,n], D. Z. Besson[e,n], K. Ratzlaff[e], J. Stockham[e], M. Stockham[e], J. M. Clem[h], R. Young[e], P. W. Gorham[c], P. Allison[b,k], O. Banerjee[b], L. Batten[i], J. J. Beatty[b,k], K. Belov[j], W. R. Binns[f], V. Bugaev[f], P. Cao[h], C. Chen[d], P. Chen[d], A. Connolly[b,k], L. Cremonesi[i], B. Dailey[b], C. Deaconu[l], P. F. Dowkontt[a], B. D. Fox[c], J. Gordon[b], C. Hast[g], B. Hill[c], R. Hupe[b], M. H. Israel[f], J. Kowalski[c], J. Lam[a], J. G. Learned[c], K. M. Liewer[j], T.C. Liu[d], A. Ludwig[l], S. Matsuno[c], C. Miki[c], M. Mottram[i], K. Mulrey[h], J. Nam[d], R. J. Nichol[i], E. Oberla[l], B. F. Rauch[f], J. Roberts[c], A. Romero-Wolf[j], B. Rotter[c], J. Russell[c], D. Saltzberg[a], H. Schoorlemmer[c], D. Seckel[h], S. Stafford[b], B. Strutt[a], K. Tatem[c], G. S. Varner[c], A. G. Vieregg[l], S. A. Wissel[m], F. Wu[a]

[a]*Dept. of Physics and Astronomy, Univ. of California, Los Angeles, Los Angeles, CA 90095.*
[b]*Dept. of Physics, Ohio State Univ., Columbus, OH 43210.*
[c]*Dept. of Physics and Astronomy, Univ. of Hawaii, Manoa, HI 96822.*
[d]*Dept. of Physics, Grad. Inst. of Astrophys.,& Leung Center for Cosmology and Particle Astrophysics, National Taiwan University, Taipei, Taiwan.*
[e]*Dept. of Physics and Astronomy, Univ. of Kansas, Lawrence, KS 66045.*
[f]*Dept. of Physics, Washington Univ. in St. Louis, MO 63130.*
[g]*SLAC National Accelerator Laboratory, Menlo Park, CA, 94025.*
[h]*Dept. of Physics, Univ. of Delaware, Newark, DE 19716.*
[i]*Dept. of Physics and Astronomy, University College London, London, United Kingdom.*
[j]*Jet Propulsion Laboratory, Pasadena, CA 91109.*
[k]*Center for Cosmology and Particle Astrophysics, Ohio State Univ., Columbus, OH 43210.*
[l]*Dept. of Physics, Enrico Fermi Institute, Kavli Institute for Cosmological Physics, Univ. of Chicago , Chicago IL 60637.*
[m]*Dept. of Physics, California Polytechnic State Univ., San Luis Obispo, CA 93407.*
[n]*National Research Nuclear University, Moscow Engineering Physics Institute, 31 Kashirskoye Highway, Russia 115409*

A.1 Introduction: The HiCal project and ANITA

The Antarctic Impulsive Transient Antenna (ANITA) [51] is a balloon-borne antenna array instrument that searches for Askaryan radio emissions from interactions of ultra-high-energy cosmic ray neutrinos with the Antarctic ice [44]. The ANITA instrument is also sensitive to ultra-high-energy cosmic ray (UHECR) radio signals [116], which are typically detected after the radio signal from the down-going shower is reflected up off of the ice surface. One important experimental uncertainty is the extent to which the surface roughness affects the received signal amplitude and spectrum of cosmic rays. The HiCal instrument is a balloon-borne high-voltage (HV) pulser that either leads or follows the ANITA payload on a separate balloon and periodically emits impulsive broadband RF signals. These radio pulses can be received by ANITA twice, both direct and reflected from the Antarctic surface, simultaneously calibrating the ANITA instrument and providing measurements of the surface reflectivity at various incidence angles. The various signals of interest to which ANITA is sensitive are shown diagrammatically in Figure A.1.

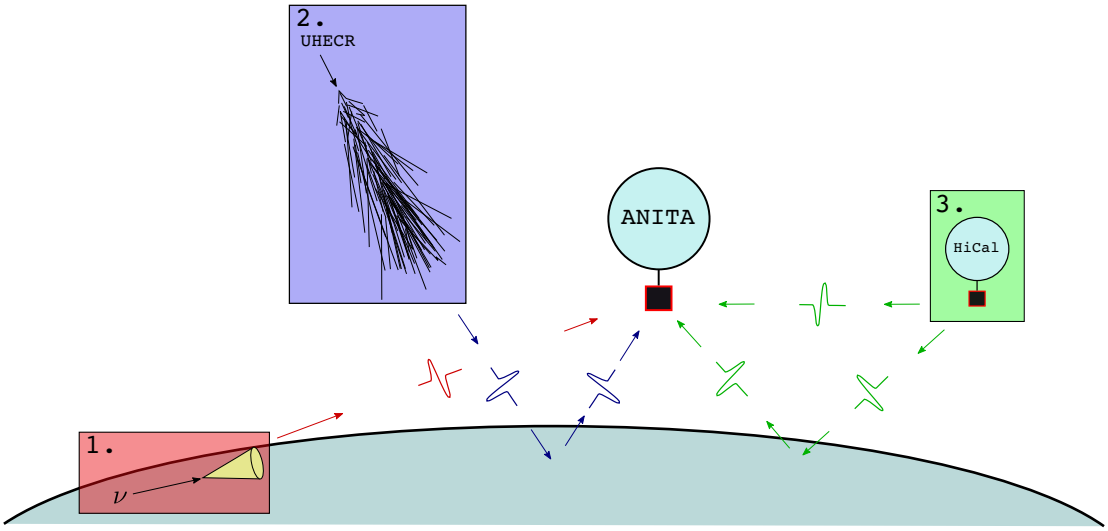

Figure A.1: The various signals searched for by ANITA. 1) Neutrino interactions with ice molecules create cones of Askaryan radiation, which upon exit from the ice, are detected by ANITA as short impulsive transients. 2) UHECR showers produce radio by a mix of the Askaryan effect and geomagnetic deflection, and are generally down-going. UHECR signals are detected by ANITA both directly, and, more commonly, after being reflected up off the ice. 3) HiCal produces an impulsive RF signal to mimic the UHECR signal. ANITA receives the HiCal signal both directly and also reflected from the ice.

HiCal-1 flew successfully in December 2014 as a companion balloon to ANITA3 [86]. In this paper, we discuss an improved system, HiCal-2, that accompanied ANITA-4 on its circumpolar journey in December 2016.

A theoretical description of the surface reflectivity problem is given in [117], which quantifies the extent to which surface roughness can affect the reconstructed primary UHECR energy. To test this model, one can analyze the ratio of reflected vs. direct signal amplitudes of various signals as seen by the ANITA instrument. An analysis of surface reflectivity using the sun during the ANITA-2 flight is given in [118], and an analysis of satellite, solar, and HiCal-1 data during the ANITA-3 flight is given in [86]. The HiCal-1 data represented the first transient signals to be analyzed in such a way, but unfortunately the flight path only allowed for measurements at very large separation distances, indicating some discrepancy between model calculation and data at such glancing surface incidence angles. Specifically, the reflected vs. direct power ratio of pulses seen by ANITA-3 exceeded predictions in the elevation angle (complement of the zenith angle) range

of 3-6 degrees. HiCal-2 was flown to provide considerably improved statistics over a wider range of incidence angles, and investigate further the apparent disagreement between model and HiCal-1 data.

A.1.1 HiCal-2 subsystems

HiCal-2 consisted of the 4 main sub-systems shown in Figure A.2:

1. The HV pulse generator and antenna, inside of a 1 atmosphere Pressure Vessel (PV).
2. Communication, telemetry, and GPS information subsystems provided by NASA's Columbia Scientific Balloon Facility (CSBF) to and from the instrument, as well as the battery power supply.
3. The Azimuth and Time-Stamp Apparatus (ATSA), for heading and environmental data.
4. The HiCal system board, which timestamped the outgoing pulses and combined PV pressure and ATSA data into packets to be telemetered.

Collectively, these systems were constrained by a 5 kg total weight limit, which proved to be an engineering challenge. Design choices had to be made to maximize performance of the instrument, while at the same time minimizing weight.

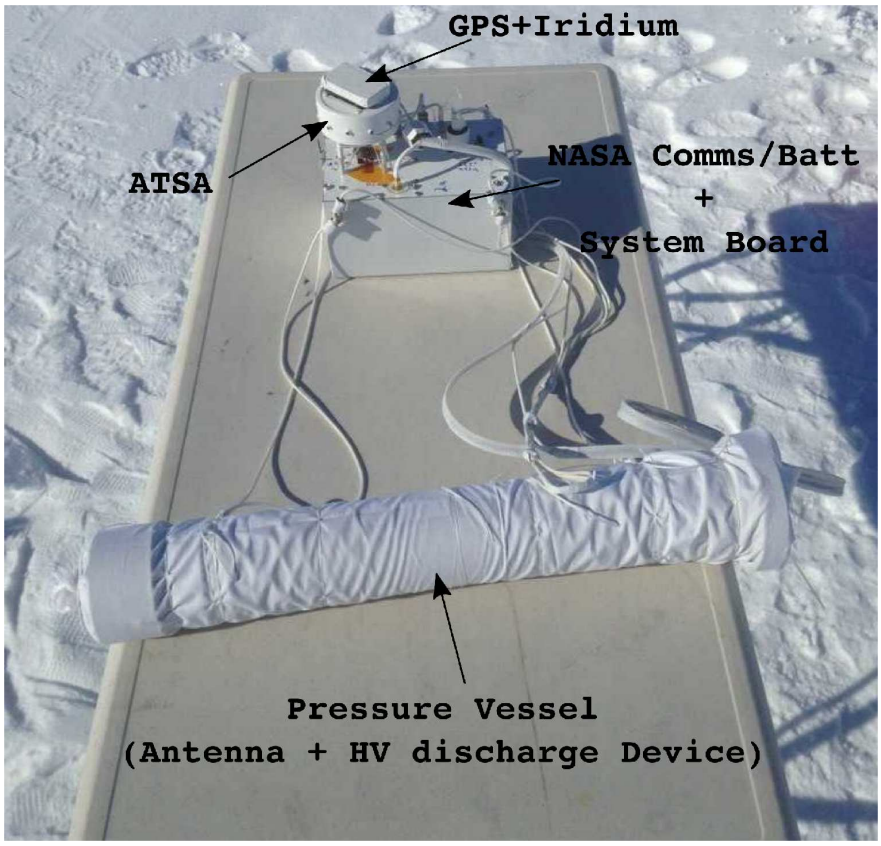

Figure A.2: The HiCal-2 instrument.

A.2 High-Voltage Pulse Generation

A.2.1 Piezoelectricity

"Piezoelectricity" is the term for the electric potential generated by a mechanical deformation of a particular type of crystal. Of interest in high-voltage applications is the fact that, for most crystals, there is a linear regime over which the output voltage is proportional to the applied stress. A device which rapidly deforms a robust crystal, in many cases by striking the crystal with a spring-loaded hammer, can produce a potential of many kV. One such device, the MSR camp-stove lighter of Figure A.3, is a particularly robust model, typically providing $>$100,000 "clicks" without failure of the crystal or striking mechanism. In this case, the impact of the hammer with the crystal results in an HV discharge across the $\sim$6 mm space between the core and the sheath of the protruding

metallic tube.

The benefits of using such a device as an HV source are two-fold. One, the power required to generate the HV discharge is solely that needed to depress the clicker mechanically, which can be done using a motor and camshaft, as described below, which for HiCal-2 was measured to be 140 mW RMS. Second, the HV source itself is electrically isolated from the electromechanical operation of the "clicker", which is advantageous in a radio frequency application.

Figure A.3: The MSR camp stove lighter.

A.2.2 A Model for high-voltage Discharge

The ideal HiCal pulse would resemble a delta function in time, thereby probing the Antarctic surface with equal power at every frequency. To approach this ideal, HiCal-1 implemented a standard spark-gap transmitter, as used in late 19th century radio experimentation and telegraphy. Spark-gap transmitters consist of an antenna attached either in series or in parallel to an air-gap and a high-voltage source. The high voltage source generates a potential across the air gap such that an arc occurs between its nodes[67]. During breakdown, RF is produced and transmitted via the antenna. Spark-gap transmitters are attractive for our purposes because the resultant RF is generally highly broadband, due to its transient nature. HiCal-2 improved upon the design of the

spark-gap transmitter by using a finely-tunable spark gap hub to tune the gap itself in such a way as to maximize output amplitude and minimize pulse width.

Empirically, we observed an inverse relationship between spark gap size and RF emission amplitude for spark gap lengths shorter than 2 mm, as shown in Figure A.5. The amplitude of the output pulse increased as the spark gap was shortened, down to $\sim$230 μm, below which the amplitude began to drop again.

A.3 Instrument

A.3.1 high-voltage System

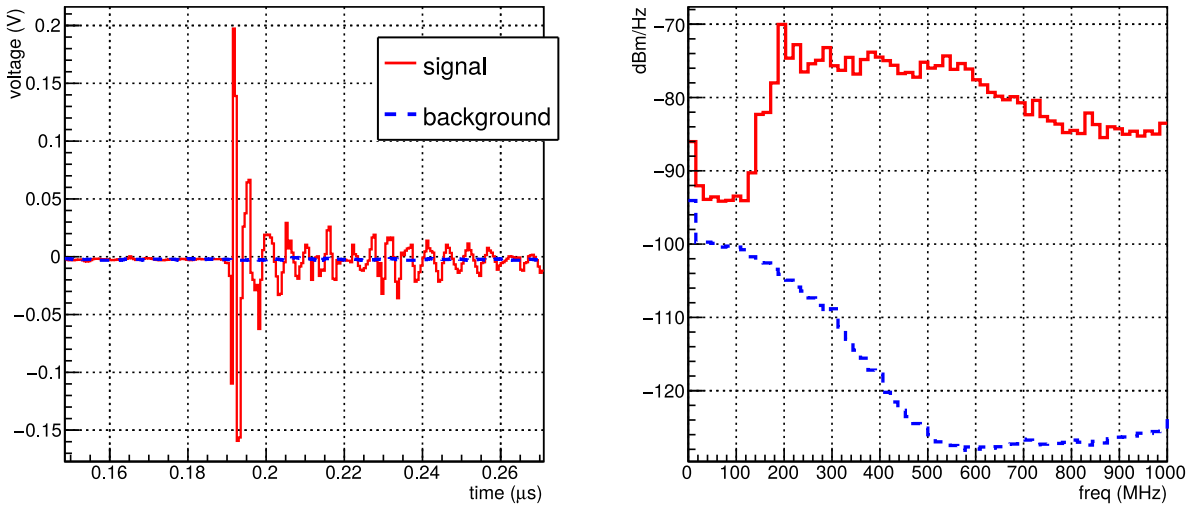

Figure A.4: An example pulse from the HiCal-2 system, as received by an Anita-4 horn antenna at a distance of 40 m and read out by an HP54542 oscilloscope, compared to ambient background. Left: Voltage vs. time. Right: Power spectrum.

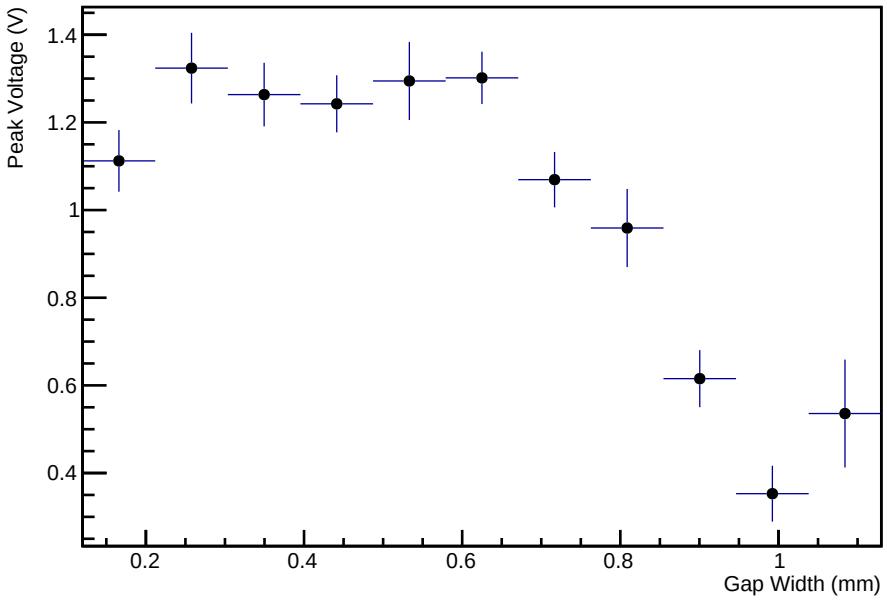

Figure A.5: Width of a spark gap vs. amplitude of the resultant pulse as measured into an RF antenna at 20m.

HiCal-2 implements the MSR sparker as the HV source of Figure A.6. A servo motor (ServoCity 20 RPM gear motor) turns a cam (a rotor with a well-defined pitch angle) at a rate of $\sim$0.1 Hz that depresses the spring of the MSR sparker, thus generating an HV potential once per revolution. This sparker is connected to the antenna such that half of the bicone is attached to the core of the sparker, the other half to the sparker's metallic sheath. As long as the spark gap between the antenna halves is the minimum impedance path in the circuit, the breakdown location migrates from the MSR sparker core/sheath to the antenna. This breakdown causes an arc across the gap between the two halves of the bicone antenna, as shown in Figure A.6.

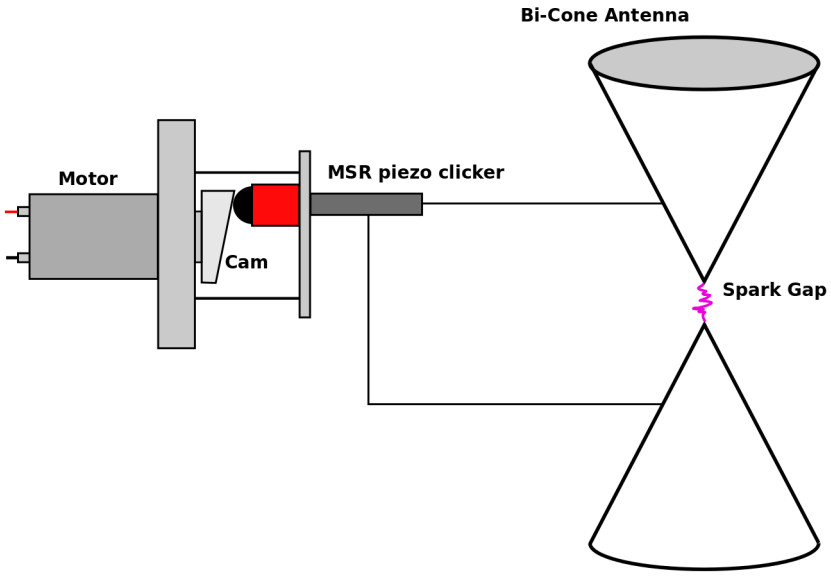

Figure A.6: Schematic of the motor mount, MSR piezo unit, and the bicone antenna (not to scale). The spark gap is exaggerated for illustration.

A key benefit of this system is that the primary failure mode is well-defined. Because the HV generation is decoupled from the electronics that turn the motor, any electronics failure will simply result in no pulses, as opposed to an unpredictable discharge.

The MSR clicker was chosen for its durability. Several duration tests were performed to ensure that the device would continue to perform after tens of thousands of clicks, and in various environments. For one such test, the motor was run continuously for 96 hours, and the output pulses were recorded. Figure A.7 shows the peak received amplitude as a function of time during the test. Figure A.8 shows a comparison of the first, the 24,000th, and 48,000th pulse from the 96 hour duration test. These pulses look nearly identical in both time and frequency space, demonstrating the durability of the piezo/breakdown system.

There was some concern about the breakdown changing the chemistry of the atmosphere inside of the sealed PV such that the breakdown and subsequent RF emission would change over the course of the mission. During the long test described above, there was no observation of any significant change in the pulses from start to finish, and therefore it was concluded that such an effect was not noticeable in the volume of air within the PV for the number of pulses expected

during the HiCal-2 mission.

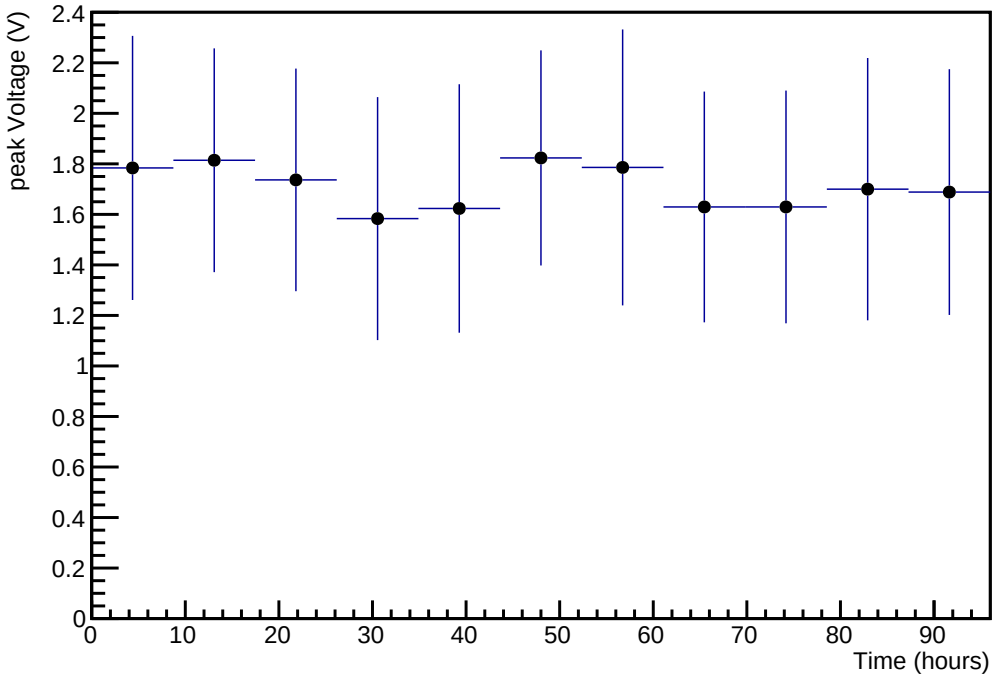

Figure A.7: A 96-hour spark test, showing the consistency of the RF emission. Error bars indicate the full spread of recorded values.

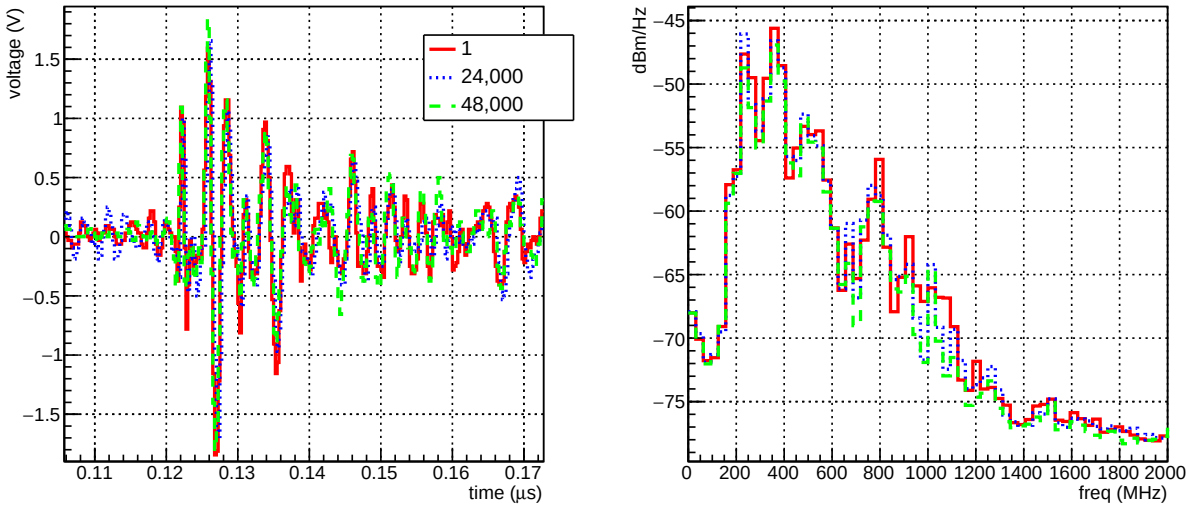

Figure A.8: Comparisson of several pulses from a 90+ hour duration test, showing consistency over time. Left:time. Right: Power spectrum.

A.3.2 Antenna

The HiCal-2 bicone antenna of Figure A.9 was used produce the RF emission from the controlled HV discharge. This antenna needed to be broadband in the range of ANITA-4 sensitivity (200–1200 MHz) but sufficiently small and light to satisfy the mass constraints for flight. The antenna consists of 24 gauge (.51 mm) aluminum sheet cut and rolled into the bicone configuration, with a half-length of 20 cm and a radius of 4.5 cm. A machined spacer, shown in Figure A.9, separates the two antenna halves, isolating them from one another. Threaded into this spacer is a tunable spark gap, set to roughly 230μm. The spacer is coupled to the antenna via brass set screws. The antenna's rigidity is provided by the pressure vessel itself, with an inner dimension matching the bicone outer dimension for a snug fit.

Figure A.9: The HiCal-2 bicone antenna, left, with a detail of the 3d-printed spacer and machined spark gap set bolt, right.

The antenna flies in the horizontal polarization configuration, e.g. aligned so that the axis of cylindrical symmetry of the antenna flies parallel to the ground plane. This ensures that the gain of the antenna in the direction of ANITA-4 is the same as the gain in the direction of the ice below (except for the extremes near the bicone ends). The gain pattern of the antenna is very similar to a dipole antenna, although more broadband due to the bicone design. The pattern for several different frequencies is given in Figure A.10.

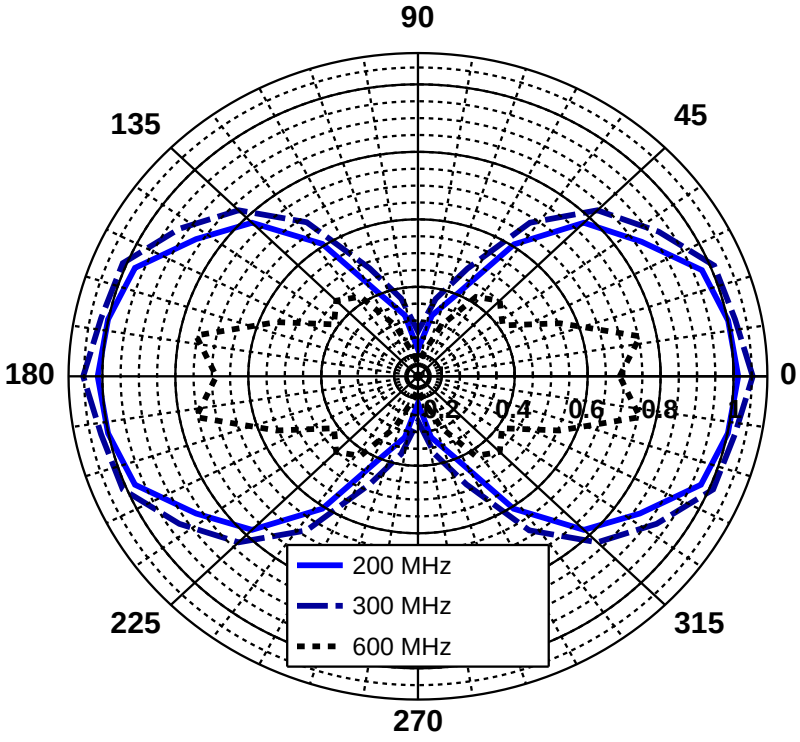

Figure A.10: The HiCal-2 antenna beam pattern for 3 frequencies. The antenna axis is aligned along the vertical axis of the plot, with cylindrical symmetry assumed.

A.3.3 Pressure Vessel and Timestamp System

To maintain the integrity and consistency of the breakdown, the antenna environment must be maintained near 1000 mbar within the ambient environment during flight of 5 mbar. Therefore, the HV system and antenna were housed in a 1 atm pressure vessel (PV). Weight and dielectric requirements motivated the use of a lightweight plastic. Acrylonitrile butadiene styrene (ABS), a typical plastic piping used for drainage, was used due to its affordability and light weight. The pressure vessel consisted of a main body with a 7.6 cm interior diameter terminated on one end by a fixed cap and the other end terminated by a machined ABS flange. An end cap with an o-ring was bolted to this flange to provide the seal. The end cap was fitted with an epoxy-filled threaded feedthrough, into which were fixed 4 wires, allowing for power and data transfer into and out of the vessel. The vessel is shown in Figure A.11, and the performance of the pressure vessels

during a rigorous thermal/vacuum test at NASA's Columbia Scientific Ballooning Facility (CSBF) in Palestine, TX is shown in Figure A.12.

Figure A.11: The HiCal-2 pressure vessel. 9 cm in diameter by 60 cm in length.

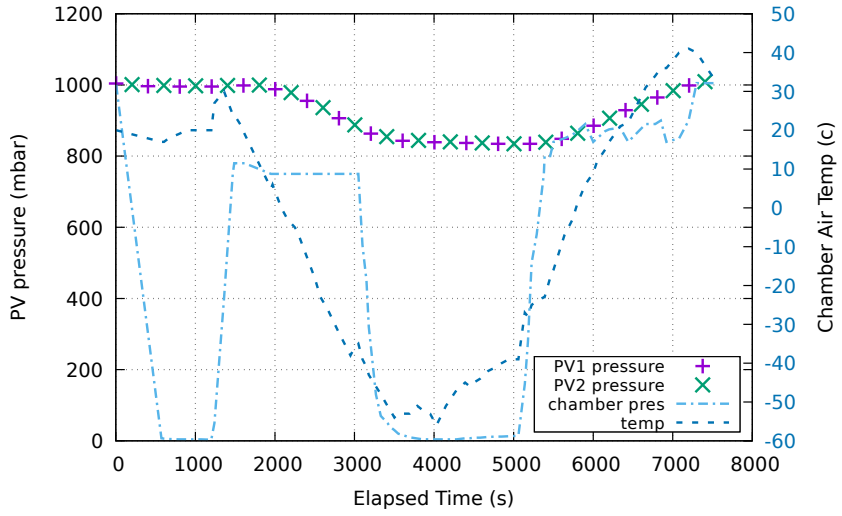

Figure A.12: Performance of the pressure vessel in a thermal/vacuum test inside of a thermal/vacuum chamber, for which temperature and pressure were cycled through flight conditions. Note the dip in pressure due to the cold temperatures typical of ascent through the troposphere.

The antenna and HV system resided within the PV. Because the HiCal motor runs autonomously

when powered and is not triggered or tied to a GPS clock, the pulse emission time is only predictable to within the ∼10 ms jitter in the camshaft rotation period, necessitating passive timestamping of the output pulses. To this end, a rigid 10 gauge (2.5 mm) pickup wire was threaded axially into the bicone, to detect the pulse and transmit it to the ATSA board (described below) for timestamping. The PV also housed a Honeywell SSCDANN015PAAB5 pressure monitor, to track the performance of the pressure vessel through the flight. The motor and the pressure monitor were both fed in parallel from a 5 V source. Correspondingly, the 4 feedthrough wires through the endcap flange of the PV were power (5V), ground, pressure monitoring, and pulse pickup antenna for timestamping. The time-series data of the monitors for HiCal-2a (second HiCal balloon to be launched) and 2b (first HiCal payload to launch) are shown in Figure A.13, showing that the PV held pressure through the flight, and that it served as a de-facto thermometer, sensitive to the day/night cycle.

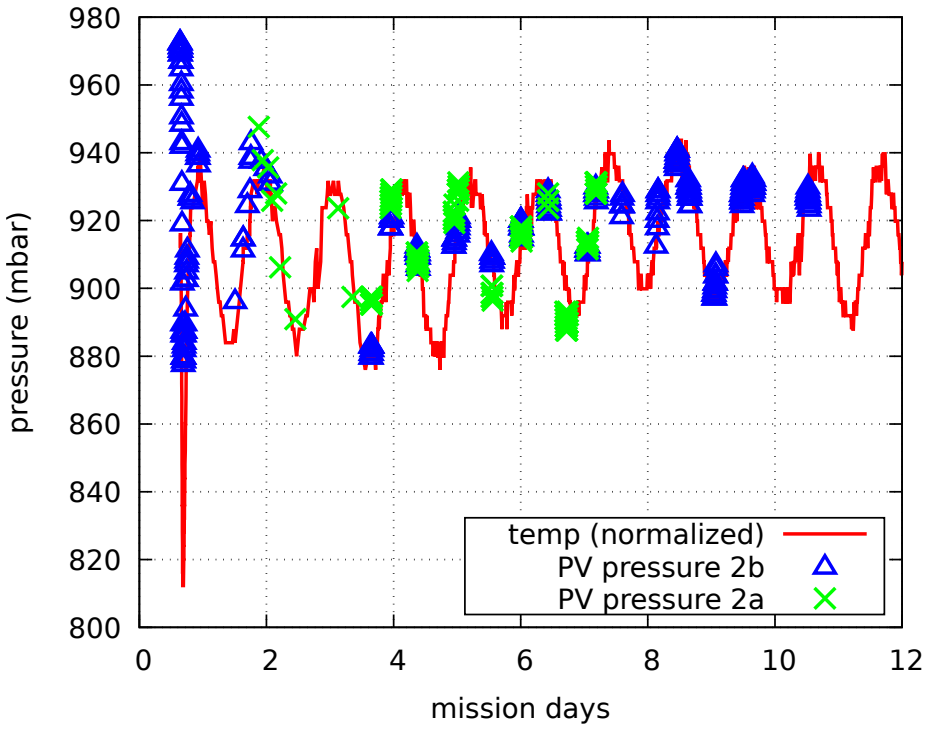

Figure A.13: Pressure of the HiCal-2 PVs. For reference, the ambient temperature is overlaid, showing that the pressure tracks the general trend of the ambient temperature. The intermittent nature of the pressure vessel data is due to the operation of HiCal in flight. The instruments were activated for roughly 30 minutes, 3 times per day; pressure monitors are only powered at that time.

A.3.4 ATSA

The azimuth and time-stamp apparatus (ATSA) flew on top of HiCal-2 to provide azimuthal orientation (accurate to ± 3 degrees) and RF pulse timestamp information (accurate to ± 55 μs) for the transmitted pulses. Details of this device are given in [119].

A.3.5 HiCal system board

The HiCal system board featured a PIC microcontroller, and was responsible for formatting all of the science data for telemetery, and providing conditioned power to ATSA and the HV discharge system, including the PV pressure monitor. It included an internal clock, synced to GPS, that would latch when ATSA registered a pulse from the PV. This timestamp, along with temperature and azimuth, were formatted and sent via RS-232 to the NASA telemetery unit for each pulse.

A.3.6 NASA electronics and power

The NASA electronics, called the MIP, consisted of GPS and Iridium units, for position and telemetery purposes respectively. The instrumentation package on board HiCal-2 had a throughput of 255 bytes/minute, including 'housekeeping' data, such as GPS, temperature, and PV pressure monitoring, and 'science' data, including our timestamped pulses and azimuth information. The MIP also had commanding capability, which allowed us to remotely turn the system on and off through an electromechanical relay governing the power to the HiCal system board.

NASA also provided custom batteries for the instrument, designed specifically for the extreme conditions of flight. These batteries powered the MIP and HiCal electronics, via the aforementioned relay. Each payload had 2 battery packs.

A.4 Implementation and Testing

The systems were designed and built at various locations, with the final integration performed over the summer of 2016 at CSBF. At the end of September 2016, a 'hang test' (Fig. A.14) was performed, during which HiCal GPS and communication were tested, followed by shipment to Antarctica in mid-October, 2016.

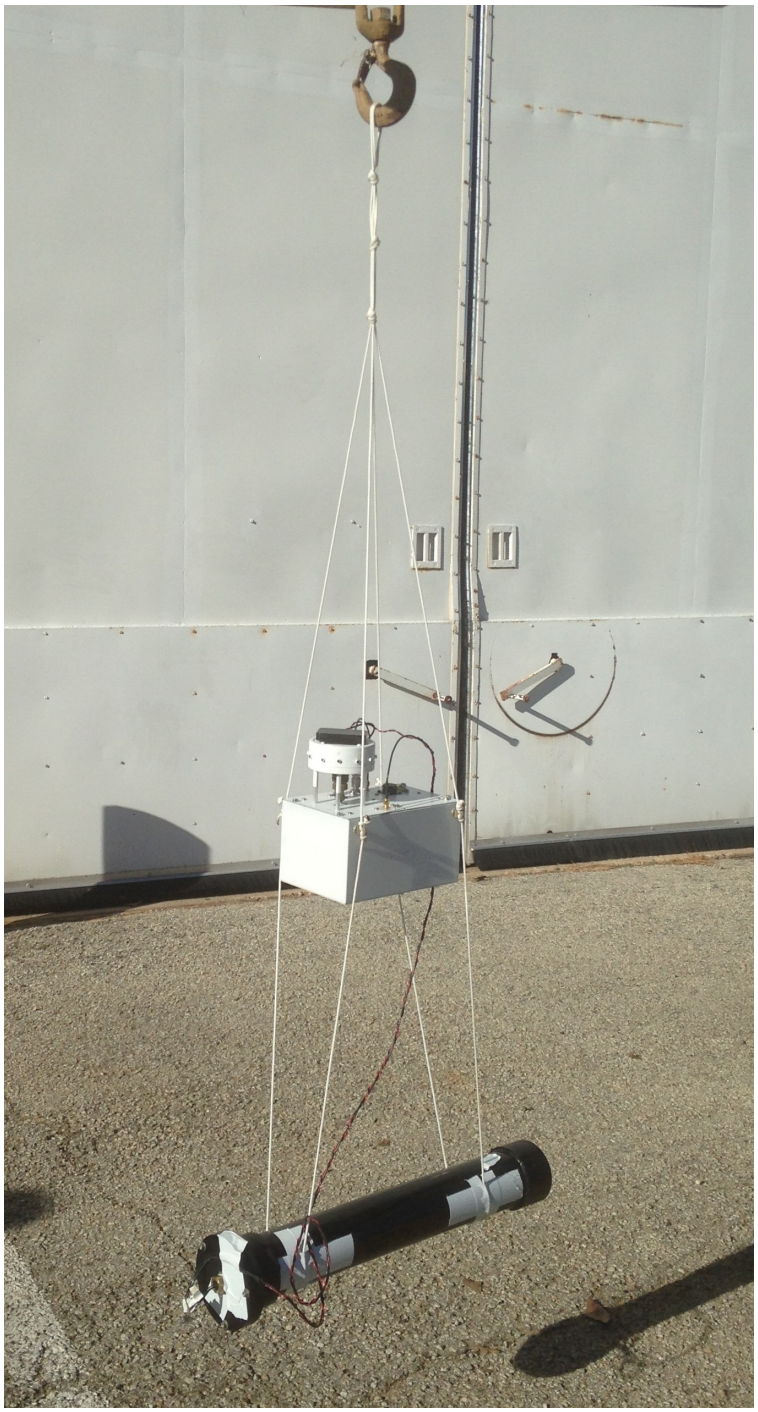

Figure A.14: The hang test at CSBF, where all systems performed nominally, verifying payload-readiness for the Antarctic flight.

A.5 Flight

HiCal-2b launched from NASA's Long Duration Ballooning Facility (LDB) on the Ross Ice Shelf of Antarctica on December 11 (initially leading ANITA-4 by approximately 700 km), with HiCal-2a launching on December 12 (initially trailing ANITA-4 by approximately 500 km), roughly 10 days after ANITA 4 launched. Photos of the payloads just after launch are shown in Figure A.15. Although the original plan was to launch HiCal immediately after ANITA 4, logistics and weather made that impossible, requiring a delay until ANITA swung back close enough to LDB after its first revolution to allow a launch in proximity. To extend the lifetime of the instruments, HiCal-2a and HiCal-2b were turned on to pulse in 30 minute intervals approximately once every six hours, and left in a low power state the rest of the flight. Although both instruments performed well, one instrument died at one-half its expected lifetime – this may have been due to a failure in one of the battery packs, although the exact failure remains undiagnosed as the payloads were not recovered. Together the two payloads completed 1.5 cumulative revolutions of the continent for a combined 18 days of flight. Their flight paths are shown in Figure A.16.

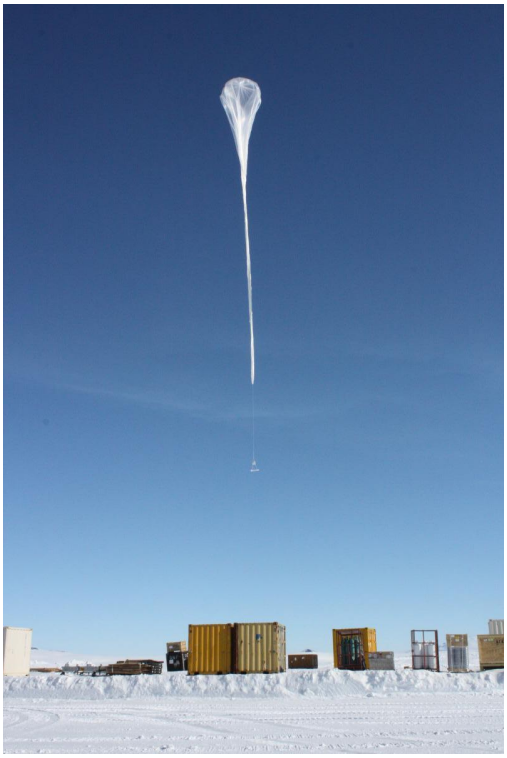

Figure A.15: The two HiCal payloads, 2a and 2b, right and left respectively. HiCal-2b is barely visible against the backdrop of cloud cover.

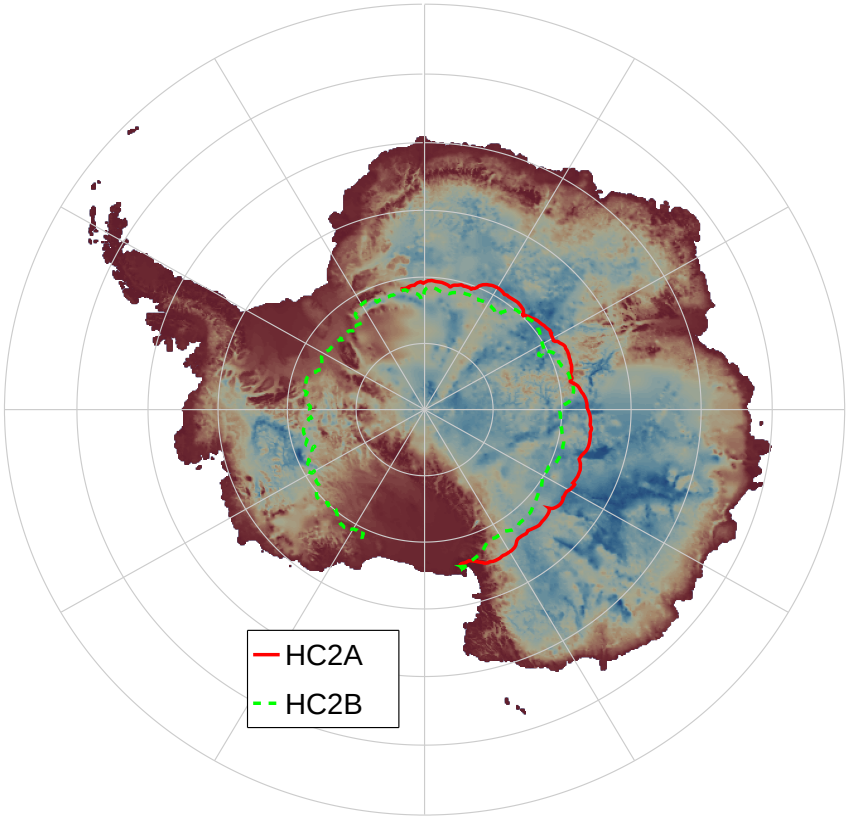

Figure A.16: The HiCal flight paths during the ANITA4 flight, over a map of the Antarctic continent. The color gradient indicates ice thickness[120].

A.6 Summary and Discussion

The analysis of the HiCal-2 data is underway, and will be presented more completely in a companion article. ANITA-4 captured $\mathcal{O}$(10,000) pulses total, direct and reflected from the ice surface, from HiCal-2, with over 2,500 'pairs' analyzed thus far, for which both the direct and reflected impulses from the same pulse were recorded. This dataset provides surface roughness information at observation angles (measured relative to the horizontal) of 4–30 degrees (separation distances of 100-700 km), and has allowed a high-statistics measurement of the surface roughness coefficient of the Antarctic ice. This distance/angle range covers the full range of interest for surface roughness studies. The range of distances (and therefore angles) scanned by HiCal-2 overlaps with all previous surface reflectivity measurements mentioned in this article.

HiCal-3, which is scheduled to fly with the proposed ANITA-5 instrument, will feature a larger payload, both horizontal and vertical polarizations, higher telemetry throughput, local RF pulse capture and improved time-stamping. This will allow us to have a record of the emitted pulse as well as the pulse as captured by ANITA, which will lower the systematic uncertainty in pulse-to-pulse variation during analysis.

Appendix B

Expansion of data in a basis

We can take a data set and expand it in a basis. This basis can be a decomposition, as in the text, of any matrix. We can build up a matrix of, for example, null data, then decompose this matrix into a basis, and expand real data into this basis. This expansion can then be used as a filter for the real data. In what follows we have two data sets, a real set, and a null set.

The general procedure is as follows: we take the null set and decompose it via singular value decomposition into a basis. We then take both sets and perform the same carrier subtraction described in Section 5.5.5. At this point the real set contains beam splash, whatever remains of the carrier after subtraction, and the putative signal. The null set will, by definition, contain only the beam splash and whatever remains of the carrier after subtraction. Then, we take each real data event and expand it into the null basis. This expansion will contain only the elements in the real data which resemble the patterns in the null set, i.e., this is our filter. This expansion (filter) is then subtracted from the original event, which leaves only the components of the real event which do not resemble the null basis.

Here we present the mathematical formulation of the basis production and data expansion. We start by building a matrix $M_{ik} = V_i^k$ where each column k of the matrix M is a vector from the null set V. We perform SVD on this matrix,

$$M = u\Lambda v*, \tag{B.1}$$

and then systematically zero all but one of the singular values (diagonal entries of Λ), which is set to 1.

$$\Lambda^{\alpha}_{ij} = \delta_{i\alpha}\delta_{j\alpha} \tag{B.2}$$

For example, Λ^3 is a matrix with a 1 in the (3, 3) position and zeros everywhere else. Then, for each index α, a basis vector e^{α} is produced by reversing the decomposition using the new matrix Λ^{α} and summing over the N columns of the reconstructed matrix M^{α}.

$$M^{\alpha} = u\Lambda^{\alpha}v* \tag{B.3}$$

$$e^{\alpha}_i = \sum_{k=1}^{N} M^{\alpha}_{ik} \tag{B.4}$$

We can then take a data vector V^d and expand it in this basis (summation over repeated indices implied),

$$c^{\alpha} = V^d_i e^{\alpha}_i, \tag{B.5}$$

e.g. the expansion coefficient c^{α} is the inner product of the signal vector with the normalized basis vector e^{α}. The expansion of the real event into the null basis is the filter $f_i = c^{\alpha}e^{\alpha}_i$. This filter can be subtracted from the data vector $V^d_{filtered} = V^d - f$, leaving any unfiltered excess in the data vector. For this specific case, what should remain after this filtration is the putative scattered signal, which was not present in the null set. The result of this procedure, for real and null sets, is presented in Figure B.1.

This figure is qualitatively similar to Figure 5.14 though the absolute amplitude is not, as here the procedure is performed on normalized vectors. The signal region excess is evident between

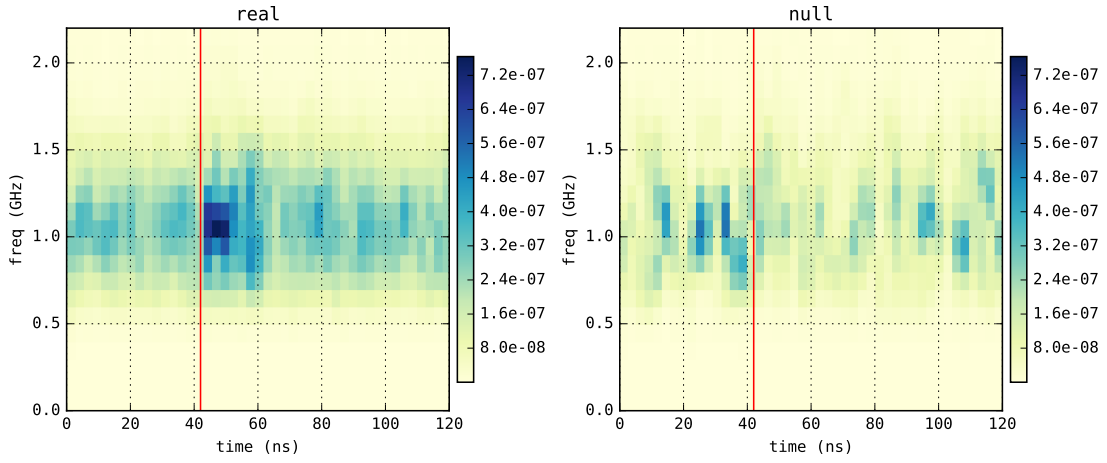

Figure B.1: A comparison of the real (left) and null (right) data after the expansion in the null basis has been subtracted from each. These spectrograms are the averages of all normalized events in the sets.

real and null sets, which have the same color scale. Using a sideband subtraction technique (as explained in the text) we obtain the significance of Figure B.2.

As seen in Figure B.2, the significance in this method is much higher than that presented in the main text.

To investigate the effect of the basis in which the filter is constructed, we can reverse the procedure, build a basis out of the real set, and repeat the above procedure using this basis. That is, we expand real and null in the real basis, and use this expansion as a filter. This should remove everything from the null set. However, since a real scatter is phase unstable on an event-by-event case, any remainder in the signal set would possibly be indication of signal. When building a basis, the features which are most similar event-to-event (e.g. the beam splash) will be most prominent, but phase unstable features will be diminished.[I] In this case, the production of the basis vectors averages the reconstructed vectors (see Eq B.4), which results in destructive interference for anything which is not phase stable.

[I]Contrast this with the method of section 5.5.7, in which the overall sum was made on the spectrogram of the reconstructed events after the beam-splash patterns had been removed event-by-event. In that case, the individual phases of the signal modes did not add destructively because they were being added in power.

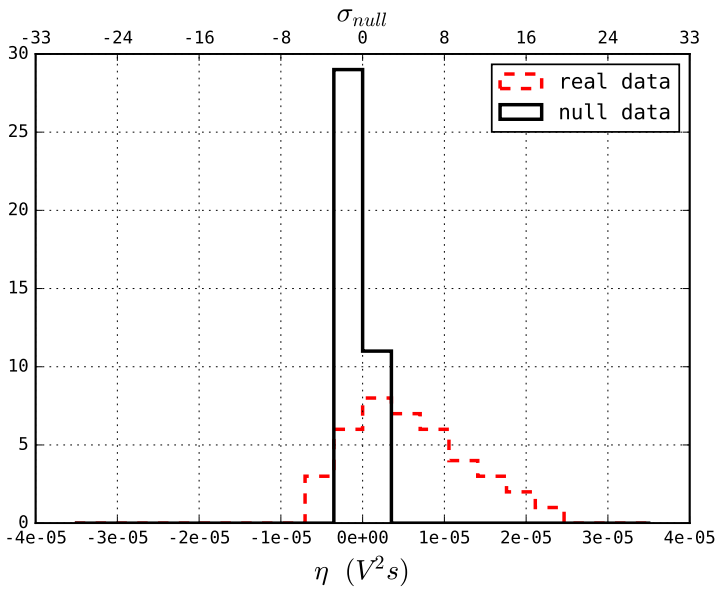

Figure B.2: The significance of the excess in the signal region of Figure B.1, corresponding to $5.26\sigma_{null}$.

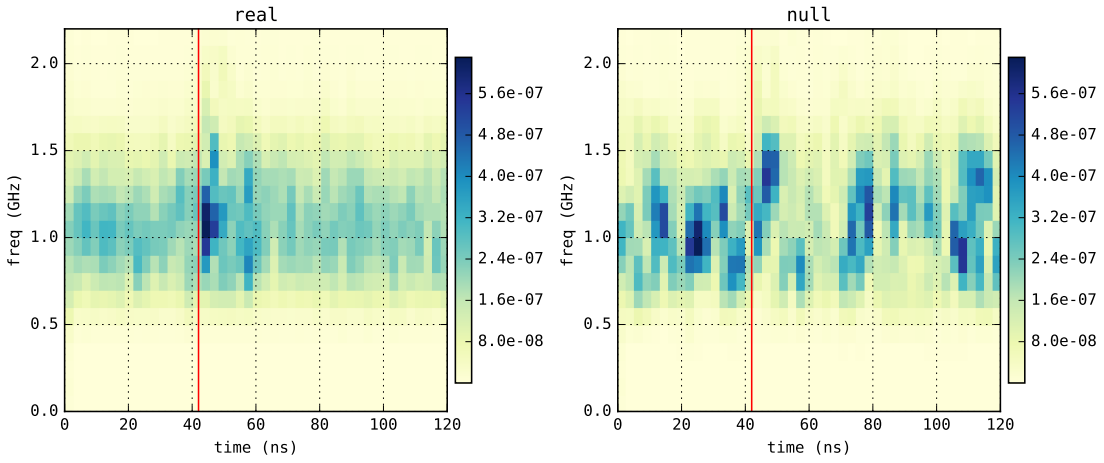

Figure B.3: A comparison of the real (left) and null (right) data after the expansion in the real basis has been subtracted from each. These spectrograms are the averages of all normalized events in the sets.

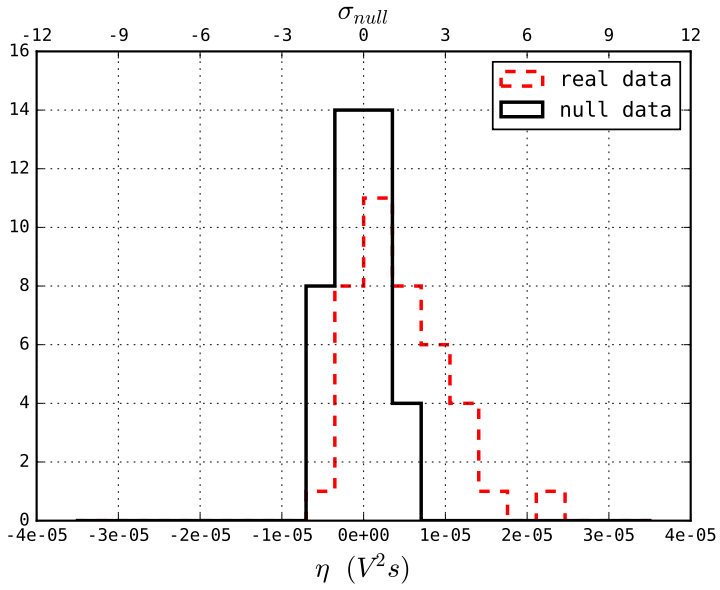

Figure B.4: The significance of the excess in the signal region of Figure B.3. The significance of the mean of the real distribution is estimated to be $1.46\sigma_{null}$.

The results of this procedure are shown in Figure B.3. We see that the null set indeed appears to be dominated by noise, and the real set is very quiet except for a small excess in the signal region. This is again explained by the lack of phase stability in the signal region. We note that this signal excess is smaller than the excess after filtration using the null basis (Figure B.1). The significance of this excess is shown in Figure B.4, and is significantly smaller than the same procedure using the null basis, as expected.